UNIVERSITÀ
DEGLI STUDI
DI PADOVA

Università degli studi di Padova

Dipartimento di Astronomia

SCUOLA DI DOTTORATO DI RICERCA IN ASTRONOMIA

CICLO XXIII

GAS METALLICITIES IN GALAXIES

Direttore della Scuola: Prof. Giampaolo Piotto
Supervisori: Prof. Alessandro Pizzella
Dott. Lorenzo Morelli

Dottorando: Andrea Cardullo

Riassunto

Gli argomenti trattati all'interno di questa tesi riguardano principalmente lo studio della metallicità del gas delle galassie attraverso la misura delle righe di emissione prodotte dal gas ionizzato, ed il calcolo di estimatori di metallicità ottenuti come rapporti tra queste.

La prima parte della tesi prende in esame un campione di galassie a redshift intermedio (z$\sim$ 0.4), tramite le quali si è cercata una correlazione tra gli indicatori di metallicità misurabili dallo spettro integrato ottenuto e proprietà fotometriche quali i colori e le magnitudini.
Nella seconda parte della tesi si analizza l'andamento radiale degli stessi indicatori di metallicità del gas per una classe di galassie non approfonditamente studiata quale è quella delle galassie di bassa brillanza superficiale.

Metallicità del gas in galassie distanti

La metallicità di una galassia è, insieme alla massa, una delle proprietà fondamentali per poter comprendere i processi fisici che caratterizzano la storia ed evoluzione delle galassie. Essa è infatti legata a tutti fenomeni che si susseguono durante l'evoluzione delle stelle, dalla nucleosintesi fino all'esplosione delle Supernovae.

Studi condotti fino ad oggi, mostrano come la metallicità sia strettamente correlata ad altri parametri fisici quali la massa o la luminosità, e cercano di interpretare le correlazioni osservate a diversi redshift nell'ambito delle diverse teorie di formazione ed evoluzione delle galassie.

A causa della generale difficoltà nell'ottenere spettri con un rapporto Segnale/Rumore sufficiente per poter studiare la componente stellare, la maggior parte

degli studi statistici o degli studi di oggetti ad alto redshift si concentra sullo studio della metallicità del gas delle galassie, attraverso lo studio delle righe di emissione prodotte.

Una precisa determinazione della metallicità del gas richiede la conoscenza della temperatura elettronica, e questa può essere accuratamente determinata solo quando siano note le intensità di righe aurorali (come [OIII]λ4363), tramite il rapporto tra queste ultime e le corrispondenti righe nebulari ([OIII]$\lambda\lambda$4959, 5007). La misura delle righe aurorali è tuttavia difficoltosa, specialmente quando la metallicità del gas è elevata e la temperatura bassa. In mancanza di una determinazione delle righe aurorali si può ricorrere a differenti metodi utilizzando altri rapporti di righe di emissione intense.

Uno dei metodi più utilizzati è probabilmente l'uso del parametro R_{23} calcolato come $\frac{[OII]\lambda3727+[OIII]\lambda\lambda4959,5007}{H\beta}$. Chiari vantaggi nell'uso del parametro R_{23} sono la sua dipendenza da righe di emissione molto intense e la sua applicabilità in un largo intervallo di distanze. D'altra parte le soluzioni in metallicità sono degeneri: a parità di R_{23} ci sono valori di alta e bassa metallicità. La degenerazione può essere superata ricorrendo all'uso di altri stimatori di metallicità quali i rapporti [NII]λ6584/Hα, [OIII]λ5007/[NII]λ6584, [NII]λ6584/[OII]λ3727, [NII]λ6584/[SII]λ6720 e [OIII]λ5007/[OII]λ3727. Ciascuno di questi è affetto in maniera più o meno significativa da una dipendenza dal grado di ionizzazione e da una dipendenza dall'arrossamento, ma si rivelano utili almeno nella determinazione nel ramo di alta o bassa metallicità delle soluzioni del parametro R_{23}. Il metodo più utilizzato è [NII]/Hα, basato su righe molto intense, ma limitato dalla sua scarsa applicabilità ad alti redshift, a causa della posizione delle righe stesse.

La possibilità di ottenere facilmente e per grandi campioni di galassie una

fotometria affidabile ed uniforme, ricorrendo all'uso di grandi cataloghi di galassie come la Sloan Digital Sky Server (SDSS), ci spingono alla ricerca di una calibrazione di R_{23} che sia indipendente da altri rapporti di righe. Una correlazione R_{23}-[NII]/Hα-colori ad esempio ci permetterebbe di sostituire il rapporto [NII]/Hα con un colore, rendendo ugualmente possibile la scelta del ramo corretto di metallicità noti i soli valori di R_{23}.

Con questo obiettivo in mente è stato analizzato un set di dati VLT/VIMOS. I dati sono stati ridotti e calibrati secondo le procedure standard della *pipeline* fornita da ESO. Tramite programmi appositamente scritti facendo uso del linguaggio IRAF, sono stati estratti dalle 1300 galassie acquisite in 7 campi diversi gli spettri di quelle che, ove presenti, mostravano simultaneamente le righe di emissione [OIII]$\lambda\lambda 4959, 5007$, [OII]$\lambda 3727$ e Hβ, necessarie per il calcolo di R_{23}, e ne è stato misurato il redshift. Gli spettri risultanti, 29 galassie in intervallo di redshift compreso tra 0.3 e 0.6, sono stati analizzati ed è stato calcolato il valore del parametro R_{23}. Dall'archivio SDSS (DR6) disponibile online si sono ottenuti i valori delle magnitudini nelle varie bande, e sono stati confrontati con i valori di R_{23}. Questo confronto non è stato sufficiente per poter trovare una calibrazione del parametro, essendo ancora necessarie informazioni sulle righe Hα e [NII]. Si è deciso quindi, parallelamente, di procedere con l'analisi di dati di letteratura per cui fossero già disponibili misure del parametro R_{23} e del rapporto [NII]/Hα, e per i quali fosse possibile ottenere la fotometria SDSS. Si è quindi analizzato un campione di galassie locali (redshift compreso tra 0 e 0.1), per le quali sono state testate possibili correlazioni tra gli indicatori di metallicità R_{23} e [NII]/Hα e i colori e le magnitudini assolute. Purtroppo anche in questo caso non è stata trovata alcuna correlazione.

L'uso del solo parametro R_{23} permette una determinazione piuttosto incerta

della metallciità specialmente nella regione dell'inversione delle soluzioni, tuttavia è stato ugualmente utilizzato per stimare l'abbondanza di ossigeno per le galassie in esame. I valori ottenuti sono poi stati posti su un piano $L - Z$ e confrontati con un campione di galassie nello stesso intervallo di redshift e con un campione di galassie locali. I punti ottenuti cadono nella stessa regione dei campioni di confronto e seguono la relazione tra luminosità e metallicità trovata per le galassie locali, confermando la mancanza di una evidente evoluzione nella relazione $L - Z$ per oggetti relativamente vicini.

Galassie di bassa brillanza superficiale

Sebbene le galassie a disco siano la classe di galassie più comune nell'universo, la formazione dei bulge, dei dischi e la loro coevoluzione è ancora poco capita, sebbene molto dibattuta. Comprendere come questi si siano formati ed evoluti è fondamentale per poter avere un quadro completo della formazione delle galassie.

La maggior parte degli studi condotti fino ad ora si è concentrata su galassie di alta brillanza superficiale (ad esempio, le galassie generalmente scelte per illustrare la sequenza di Hubble), trascurando al contrario galassie di bassa brillanza superficiale (LSB) che, sebbene più difficili da osservare, non costituiscono una classe di oggetti peculiari.

Le galassie LSB, definite come quelle galassie che esibiscono una brillanza superficiale centrale deproiettata per il disco superiore di almeno una magnitudine rispetto al limite di $\mu_B(0) = 22.7$ mag arcsec^{-2}, rappresentano una classe di galassie dalle caratteristiche insolite. Il quadro che si ottiene dagli studi fin ora condotti mostra che queste galassie sono generalmente caratterizzate da una bassa densità superficiale nella distribuzione di HI, e che si tratta di oggetti compatti e meno evoluti rispetto al resto delle galassie. Tuttavia non si tratta di

oggetti piccoli, mostrando raggi di scala di diversi kpc comparabili con le galassie di alta brillanza superficiale. Sono generalmente oggetti di bassa metallicità, con basso tasso di formazione stellare, e cinematica e potenziale gravitazionale dominato dalla materia oscura. D'altra parte, alcuni studi mostrano come non vi siano sostanziali differenze tra gli sferoidi di galassie LSB giganti e quelli di galassie HSB, e che i due tipi di galassie si sovrappongono sul piano della relazione Tully-Fisher. È stato trovato anche che, contrariamente a studi precedenti che affermano il decrescere della metallicità con il decrescere della brillanza superficiale, le galassie LSB possono esibire metallicità di tipo solari.

A causa della lora bassa brillanza, è generalmente difficile ottenere spettri spazialmente risolti abbastanza profondi da poter studiare in dettaglio sia la componente gassosa che la componente stellare separatamente, preferendo quindi spettri integrati in cui poter studiare la componente più brillante della galassia, vale a dire le regioni HII, e rinunciando allo studio dei profili radiali di abbondanza.

In questa tesi abbiamo analizzato un campione di galassie locali di bassa brillanza superficiale per cui erano disponibili osservazioni VLT/FORS2. Sfruttando le brillanti righe di emissione di [OIII] e Hβ è stato calcolato l'indicatore R_3 tramite cui è stata determinata infine la metallicità. I lunghi tempi di esposizione e la qualità dei dati hanno permesso di ottenere i profili radiali di metallicità per le galassie del campione, mostrando un valore generalmente alto per la metallicità e la presenza di un, sebbene lieve, gradiente con il raggio.

Questo tipo di dati è estremamente raro per galassie LSB, per le quali ad eccezione di pochissimi casi, sono generalmente disponibili solo valori integrati di metallicità.

Il confronto di questi risultati con la letteratura, pone le galassie studiate in

una posizione intermedia tra quanto generalmente ottenuto per le LSB e le galassie HSB, sottolineando di fatto la necessità di ulteriori indagini per comprendere a fondo questo tipo di oggetti.

Abstract

Topics covered in this thesis mainly concern the study of gas metallicity in galaxies by measuring the emission lines produced by ionized gas, and the calculation of metallicity estimators as the ratio between them.

The first part of the thesis examines a sample of galaxies at intermediate redshift ($z \sim 0.4$), through which we searched for a correlation between the metallicity indicators measurable on the integrated spectrum and photometric properties such as colors and magnitudes.
In the second part of the thesis we analyzed the radial profiles of the same gas metallicity indices for a class of galaxies not yet studied in great detail such as the low surface brightness galaxies.

Gas metallicity in distant galaxies

The metallicity is, together with the mass, one of the fundamental properties necessary to understand the physical processes that characterize the history and evolution of galaxies. It is indeed related to all the phenomena that take place during the evolution of the stars, from nucleosynthesis to supernovae explosions.

Studies performed so far, show how the metallicity is connected to other physical parameters like the mass or the luminosity, and they try to interpret the observed correlations at different redshift in the context of different theories

of formation and evolution of galaxies.

Due to the general difficulties in obtaining spectra with S/N high enough to study the stellar component, most of the statistical studies or the studies of high redshift objects focus on the gas metallicity, through the study of the emission lines.

For a precise determination of the gas metallicity, knowledge of the electron temperature is required, however this can be accurately determined only when there are known the intensity of the auroral lines (such as [OIII]λ4363), through the ratio between them and the corresponding nebular lines ([OIII]$\lambda\lambda$4959, 5007). The measure of the auroral line is however difficult, especially when the gas metallicity is high and the temperature low. In absence of a determination of the auroral lines other methods based on bright emission lines can be used.

One of the most used method is probably the parameter R_{23} calculated as $\frac{[OII]\lambda3727+[OIII]\lambda\lambda4959,5007}{H\beta}$. Clear advantages in the use of the parameter R_{23} are its dependence on very bright emission lines and its applicability over a wide range of distances. On the other hand, the metallicity solutions are degenerate: the same value of R_{23} can represent both high and low metallicity. This degeneracy can be broken through the use of other estimators obtained from bright emission lines such as the ratios [NII]λ6584/Hα, [OIII]λ5007/[NII]λ6584, [NII]λ6584/[OII]λ3727, [NII]λ6584/[SII]λ6720 and [OIII]λ5007/[OII]λ3727. Each of these is affected more or less significantly from the degree of ionization and reddening, but they are useful in determining at least the correct branch of metallicity solutions for the parameter R_{23}. One of the most used method is [NII]/Hα, based on very strong lines, but limited by its lack of applicability at high redshift, due to the location of the lines themselves.

The possibility to easily obtain large samples of galaxies with reliable and

uniform photometry, by means of large catalogs of galaxies like the Sloan Digital Sky Server (SDSS), drives us to search for a calibration for R_{23} independent of other line ratios. An R_{23}-[NII]/Hα-color correlation for example, would allow us to replace the lacking [NII]/Hα ratio with a color, making equally possible to choose the correct branch of metallicity, being known R_{23}.

With this in mind a set of VLT/VIMOS data has been analyzed. The data were reduced and calibrated according to standard procedures of the ESO pipeline. Through special programs written using the IRAF language, there were extracted from the 1300 galaxies obtained in 7 different fields the spectra of those, if any, showed simultaneously the [OIII]$\lambda\lambda 4959, 5007$, [OII]$\lambda 3727$ and Hβemission lines, necessary to compute R_{23}, and their redshift was measured. The resulting spectra, 29 galaxies in the redshift range between 0.3 and 0.6, were analyzed and R_{23} has been calculated. From the SDSS archive (DR6), available online, there were extracted the magnitudes in the various bandpasses, and were compared with R_{23}. This comparison was not sufficient to find a calibration for the parameter, still missing information about the Hαline. It has been therefore decided, in parallel, to proceed with the analysis of literature data for which were already available measurements of R_{23} and the [NII]/Hαratio, and for which it was possible to obtain SDSS photometry. We then analyzed a sample of local galaxies (redshift between 0 and 0.1), for which possible correlations between the metallicity indicators R_{23}, [NII]/Hα and the colors or absolute magnitudes were tested. Unfortunately also in this case no correlation has been found.

The only R_{23} parameter allows a poor determination of the metallicity, especially in the region of the inversion, however it has been used to obtain estimate of the oxygen abundance for the galaxies examined. The values obtained there were plotted on a $L - Z$ plane and compared with a sample of galaxies in the

same redshift range and with a sample of local galaxies. The data obtained fall in the same region of the comparison samples and follow the luminosity-metallicity relation found for local galaxies, thus confirming the lack of an evident evolution in the $L - Z$ relation for relatively close objects.

Low Surface Brightness galaxies

Even though disk galaxies represent the most common class of large galaxies in the universe, the formation of bulges and disks and their coevolution is still poorly understood and hotly debated. Understanding how they formed and evolved is therefor fundamental to obtain a complete picture of galaxy formation.

The majority of studies performed so far, focused on high surface brightness galaxies (for example the galaxies generally adopted to illustrate the Hubble sequence), neglecting on the contrary low surface brightness galaxies (LSB) which, even if more difficult to be identified than their HSB counterparts, are far from representing an oddity.

Low Surface Brightness galaxies, defined as those galaxies exhibiting a central deprojected surface brightness of the disk exceeding by at least one magnitude the limit $\mu_B(0) = 22.7$ mag arcsec^{-2}, represent a class of galaxies with peculiar characteristics. The picture obtained so far shows that these galaxies are generally characterized by a low surface density in the distribution of HI, also that they are compact objects and less evolved then the other galaxies. However they are not small objects, exhibiting scale radii of several kpc, comparable with those of High Surface Brightness galaxies (HSB). Their are generally metal poor, with low star formation rates, and with kinematics, and therefore gravitational potential, dominated by dark matter. On the other hand, several studies show how there are no substantial differences between the bulges of giant LSB and HSB

galaxies, and also that these galaxies overlap on the Tully-Fisher relation. It has been also found that, contrarily to previous studies that claimed the connection between the decreasing of the metallicity and the decreasing of the central surface brightness, LSB galaxies can exhibit near solar metallcity.

Due to their low brightness, it is generally difficult obtain spatially resolved spectra deep enough to study their gaseous and stellar component separately, thus preferring the analysis of the brightest component of the galaxy, i.e. the HII regions, on integrated spectra, and renouncing the study of abundance radial profiles.

In this thesis we analyzed a sample of local low surface brightness galaxies for which were available VLT/FORS2 observations. Through the bright emission lines [OIII] and Hβ, the index R_3 has been computed and the metallicity derived. Long exposure time and high data quality allowed us to obtain metallicity radial profiles for the galaxies of the sample, showing generally high values and the presence of a, even if shallow, gradient with radius.

This kind of data is extremely rare for LSB galaxies, for which are generally available only integrated values for the metallicity, excepted for very few cases.

The comparison between these results and the literature, places the galaxies studied in an intermediate position between the general picture obtained for LSB galaxies and HSB, underlying the necessity of further investigation to better understand these objects.

Contents

List of Tables

List of Figures

Introduction

Chapter 1

Gas metallicity in galaxies

Galaxy mass and metallicity are two of the most important physical properties of galaxies. They are metrics of the evolution processes, being related to the amount of gas locked up into stars and to all the important phenomena that take place during the whole stellar evolution phases, from nucleosynthesis to supernovae explosions. The comprehension of the connection between these properties, and their evolution with time are fundamental to understand the physical processes that determine the history and evolution of galaxies.

Since the 1907s, it is known that low-luminosity dwarf galaxies have systematically lower metallicities compared to more luminous galaxies (Lequeux et al., 1979; Skillman et al., 1989; Richer & McCall, 1995). This dependence, initially obtained for irregular galaxies, was later confirmed for galaxies of different morphological types (e.g. Vila-Costas & Edmunds, 1992; Kobulnicky & Zaritsky, 1999; Melbourne & Salzer, 2002; Lee et al., 2004; Pilyugin et al., 2004; Lee et al., 2006).

The differences between giant and dwarf galaxies are usually attributed to different chemical evolution of galaxies with different masses (e.g. Lequeux et

al., 1979; Tremonti et al., 2004; Lee et al., 2006; Ellison et al., 2008). Thus, more efficient mechanisms seem to be at work in massive galaxies converting gas into stars and/or less efficient ones ejecting enriched matter into the galactic halo or even into the intergalactic medium. While the mass of a galaxy is one of the key physical parameters governing galaxy evolution, its determination is not easy and somewhat uncertain. Therefore, very often the luminosity, which is directly derived from observations, is used as a proxy for the mass.

Metallicity reflects the level of the gas astration in the galaxy. Hence, the metallicity of a galaxy depends strongly on its evolutionary state, specifically, on the fraction of the gas converted into stars. The metallicity in emission-line galaxies is defined in terms of the relative abundance of oxygen to hydrogen (usually 12 + log O/H) in the interstellar medium (ISM).

Various physical processes may be responsible for the mass-metallicity $M-Z$ (and luminosity-metallicity $L-Z$) relation. One possibility is that outflows, generated by starburst winds, eject metal-enriched gas into the IGM preferentially out of low-mass galaxies (due to the shallow gravitational potential well), making their enrichment less effective than in massive systems (e.g. Tremonti et al., 2004; De Lucia et al., 2004; Finlator & Davé, 2008). An alternative scenario is that low mass systems are still at an early evolutionary stage and have still to convert most of their gas into stars, hence they are poorly metal-enriched relative to massive galaxies (which are instead already evolved). This is the so-called "galaxy downsizing" scenario, supported by various observational evidences (e.g. Juneau et al., 2005; Feulner et al., 2005; Franceschini et al., 2006; Asari et al., 2007), where massive galaxies formed most of their stars rapidly and at high redshift, while low mass systems are characterized by a slower evolution, which extends to low redshift. Finally Köppen et al. (2007) ascribes the mass-metallicity relation

to variations of the IMF high-mass cutoff in different star forming environments.

The relative role of these processes is debated. It is likely that each of them contributes at least to some extent, since observational evidences have been found for all of them. Each of these factors (outflows/feedback, downsizing, IMF) has profound implications on the evolution of galaxies. Therefore, it is clear that the $M - Z$ (and $L - Z$) relation contains a wealth of information useful to constrain models of galaxy formation and evolution.

Observational constraints of the mass-metallicity relation have been obtained up to z$\sim$3.5 thanks to various deep surveys (Savaglio et al., 2005; Liang et al., 2006; Erb et al., 2006; Maiolino et al., 2008). While it is evident an evolution of the $M - Z$ relation (as well as the $L - Z$ relation) at high redshift, in the sense that on average higher redshift galaxies are characterized by lower metallicities (at given mass), it is still not clear what happens at intermediate redshift. Among the studies at z<1, mainly based on small samples, some authors (e.g. Savaglio et al., 2005; Maier et al., 2005) found that a consistent fraction of the galaxies observed have metallicities lower than those of local galaxies with similar luminosities and star formation rates. In contrast, Lilly et al. (2003) and Lamareille et al. (2006) found that metallicities appear to be remarkably similar to those of local galaxies.

Note that, due to difficulties in obtaining high S/N spectra on the stellar continuum, all of these studies refer to the gas metallicity obtained from the analysis of the HII regions.

The HII regions are ionized clouds of gas associated with zones of recent star formation: powered by one, a few or a cluster of massive stars they are the place where heating and cooling processes such as photoionization, recombination, collisions and so on, are responsible for the production of bright emission lines.

Emission line ratios can be used to asses the chemical composition of these regions, being related to their temperature. The methods used to determine the abundances can be divided essentially in two groups, the empirical and the model fitting methods. The first includes both the direct and statistical methods.

A direct measure of the abundance ratio of two ions is obtained from the observed intensity ratio of lines emitted by these ions. For example, the ratio O^{++}/H^{+} can be derived as follows:

$$O^{++}/H^{+} = \frac{[OIII]\lambda 5007/H\beta}{j_{[OIII](T_e,n)}/j_{H\beta(T_e,n)}} \tag{1.1}$$

where $j_{[OIII](T_e,n)}$ is the emission coefficient of the [OIII]λ5007 line, which is dependent on the electronic temperature T_e and the density n (assumed uniform in the nebula). The density is usually derived from intensity ratios of two lines of the same ion which have the same excitation energy but different collisional deexcitation rates, like the most commonly used [SII]λ6731/6717 ratio, or by means of far infrared lines or, finally, through ratio of high order hydrogen recombination lines.

The electronic temperature T_e can be derived using temperature-sensitive line ratios, such as the ratio between the two lines [OIII]λ4363 and [OIII]λ5007, which have very different excitation potentials (Osterbrock, 1989). Other line ratios can also be used as temperature indicators, such as [NII]λ5755/6584 and [SII]λ6312/9532.

However, the *auroral* lines (transition from the second lowest excited level to the lowest excited level: [OIII]λ4363, [NII]λ5755, ...) are generally too weak to be measured respect the *nebular* counterparts (first excited level to the ground level: [OIII]$\lambda\lambda 4959, 5007$,[NII]$\lambda\lambda 6548, 6584$, ...), especially in metal-rich regions where the temperature is low: as metallicity increases, also the efficiency of the cooling

processes due to the emission lines of metals in the near infrared increases, cutting down the temperature and thus inhibiting the collisional processes responsible for the auroral emission lines.

When the electron temperature cannot be determined (because the temperature sensitive lines cannot be observed, or simply because the observations do not cover the appropriate spectral range), one has to go for statistical methods or "strong line methods". However, unlike the direct methods for abundance determinations, statistical methods have to be calibrated. This can be done empirically using abundances derived from direct methods, or objects other from HII regions thought to have the same chemical composition (Pilyugin & Thuan, 2005; Pilyugin, 2003; Tremonti et al., 2004; Liang et al., 2006; Nagao et al., 2006), or theoretically using grid of ab-initio photoionization models (McGaugh, 1991; Kewley & Dopita, 2002). Clearly the reliability of statistical methods will depend not only on the choice of an adequate indicator but also on the quality of the calibration.

These techniques have first been introduced by Pagel et al. (1979) who used the 4 strongest lines of O and H: Hα, Hβ, [OII]λ3727 and [OIII], to derive metallicities in giant extragalactic HII regions. The relative intensities of the emission lines in a nebula depend on the mean effective temperature of the ionization source, the gas density distribution and the metallicity, represented by O/H. Oxygen is at the same time the main coolant in nebulae and the element whose abundance is most straightforwardly related to the chemical evolution of galaxies therefore, assuming that the effective temperature is closely linked to the metallicity, and that it is the metallicity that drives the observed line ratios, a ratio involving the two most important ionization states of oxygen would be useful as indicator of the O/H ratio. Pagel et al. (1979) proposed the R_{23} parameter

defined as follow:

$$R_{23} = \frac{[OII]\lambda 3727 + [OIII]\lambda\lambda 4959, 5007}{H\beta} \tag{1.2}$$

The Hα line was used to correct the spectra for reddening, by means of the comparison between the observed Hα/ Hβ ratio with the case B recombination value at a typical T_e.

There are many other metallicity indicators that have been proposed: [OIII]λ5007/[NII]λ6584 (O_3N_2) by Alloin et al. (1979); [NII]λ6584/Hα (N_2), by Storchi-Bergmann et al. (1994); ([SIII]$\lambda\lambda$9069, 9532+[SII]λ6720)/Hα (S_{23}), by Vilchez & Esteban (1996); [NII]λ6584/[OII]λ3727 (N_2O_2) by Dopita et al. (2000); [ArIII]λ7135/[OIII]λ5007 (Ar_3O_3) and [SIIIλ9069/[OIII]λ5007 (S_3O_3) by Stasińska (2006); [NeIII]λ3869/[OII]λ3727 (Ne_3O_2) by Nagao et al. (2006).

The most widely used index is probably the R_{23} parameter. However this index, as other indexes based on ratios of optical collisionally excited line and a recombination line (e.g. S_{23}), has the disadvantage of being double-valued. In fact at low metallicities, when cooling is dominated by recombination and collisional excitation of hydrogen, T_e is independent of the relative abundance of oxygen and hydrogen, and R_{23} is proportional to O/H. At high metallicities, on the contrary, the T_e is low and the cooling is efficient with the energy mainly evacuated by the infrared line [OIII]λ8800. Since T_e decreases with increasing O/H, R_{23} increases.

To find whether the objects under study are on the "high abundance" or "low abundance" branch, there are necessary external arguments. The most common is based on the [NII]λ6584 line. The N/O ratio is observed to increase as O/H increases, at least at high metallicities. Moreover, high metallicity HII regions tend to have lower ionization parameters favouring low-excitation lines

such as [NII]λ6584. There are several ratios that make uses of [NII]λ6584 line, used to discriminate between the two branch solutions of the R_{23} index, such as [NII]λ6584/Hα, [OIII]λ5007/[NII]λ6584, [NII]λ6584/[OII]λ3727, [NII]λ6584/[SII]λ6720 (Pettini & Pagel, 2004; Nagao et al., 2006).

Each of these ratios depends, more or less severely, on the ionization level (which is usually estimated by means of the O_{32}=[OIII]λ5007/[OII]λ3727 ratio) and reddening, so that they present different level of accuracy, but they are useful in determining the branch of high or low metallicity solution for R_{23}.

As we already pointed out, statistical methods requires to be calibrated. The easiest way is through the analysis of the abundances given by the photoionization model fitting. In general there are different reasons to build photoionization models. For example one might want to check the sensitivity of input parameters on observable properties, or derive the chemical composition of a given nebula or estimate characteristics of the ionizing source and so on. Each case requires a specific approach, for example, if one wants to derive the chemical composition of a nebula by means emission line fitting, it is not sufficient to find one solution, while it would be necessary to explore the entire range of possible solutions, given the observational constraints. Focusing on the determination of abundances one can follow two different approaches: tailored model fitting or grids of models. In the first case the procedure would imply some steps such as:

1. the definition of the input parameters (characteristics of the ionizing radiation field, gas density, chemical abundances, distances)
2. the use of an appropriate code
3. the comparison between the observed data with the outputs
4. the iteration of the previous steps until the observations are satisfactorily reproduced (which means that all the observational data are reproduced

within acceptable limits).

This approach, in order to obtain a good quality of the fit, requires that as many observational constraints as possible are available (i.e. not only the line intensity ratios), reminding also that some constraints are not independent (for example, being the [OIII]λ5007/4959 ratio fixed by atomic physics, the ratios [OIII]λ5007/Hβ and [OIII]λ4959/Hβ should both be fitted) and can be used to test the goodness of the observations. A priori, if all the observations are fitted within the errors, the model abundances represent the real abundances. This however is often not the case, which means either that the observations were not as good as thought or that some assumptions in the modelling may be incorrect, not representing the real situation.

If one is interested in determining the metallicities for a large sample of objects, a tailored model fitting procedure would be extremely time consuming, so that it becomes useful the analysis through a vast grid of photoionization models where derive the metallicities of the observed emission lines by interpolation. However also in this case the metallicities derived should be used with caution. Yin et al. (2007), showed that this method can return abundances higher to those directly obtained from [OIII]λ4363. They argued that since the procedure uses simultaneously all the strong lines to derive O/H, any offset between real and adopted N/O induces an offset in the derived metallicity.

So far it has been pointed out that abundances in galaxies can be estimated through the bright emission lines emitted by the HII regions. Even if there are necessary more then one emission line ratios, coupled with photoionization models or direct measures, it is evident that this kind of analysis shows its usefulness when we move our observations toward distant objects. As seen before, in fact, there are a multitude of possible line ratios that can be used when we

plan to use observations from the ground, not only for the local universe. In particular, the lines necessary to compute the R_{23} parameter, plus the [NII] lines, can be observed simultaneously from ground (using appropriate bandpasses) up to z $\sim$ 2.6, as showed in figure 1.1.

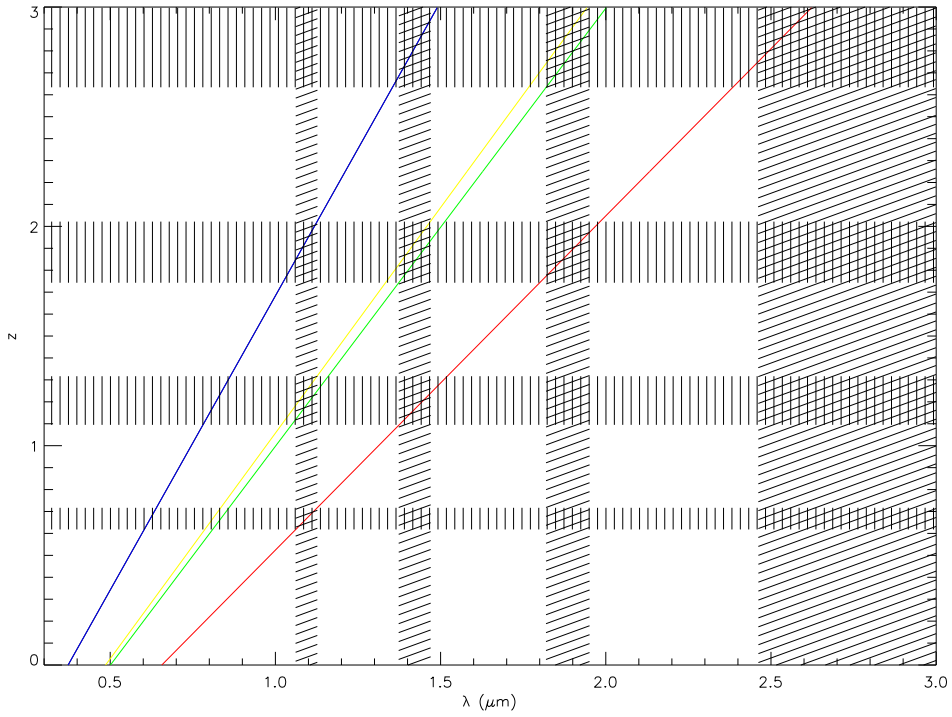

Figure 1.1: The figure illustrates the wavelength of the redshifted [OII] (blue), [OIII] (green), Hβ (yellow), and [NII] (red) lines. The shaded vertical areas indicate low atmospheric transmission, the horizontal shaded areas indicate redshift intervals where these lines cannot be observed simultaneously from ground.

Focusing on the R_{23} ratio, it appears evident that it could be used up to redshift z $\sim$ 0.5, by mean of the only optical band. However, in this way we lose all the other lines generally used to break the degeneracy in the metallicity solutions of this parameter ([NII] for example moves into the infrared band, making necessary the use of a second observation to obtain it).

For this reason, it would be useful to find a calibration for the R_{23} parameter to be independent of other emission line ratios.

Nowadays, electronic archives give us free access to an incredible amount of data that can be used for a lot of different purposes. For this reason we decided to investigate if a connection between photometry and R_{23} is possible. Any correlation between R_{23}, [NII]λ6584/Hα and color, for example, would allow us to replace the necessity of using additional emission lines, with a simpler-to-obtain photometric measure, thus avoiding the limitations (e.g. both in terms of time necessary for multiple observations or maximum distance of the objects) intrinsic in the usual spectral analysis.

Chapter 2

Low Surface Brightness galaxies

Understanding the formation and evolution of galaxies is one of the most important issues in extragalactic research.

One of the key questions is whether all galaxies formed early through a dissipational collapse of large protogalaxies in a "monolithic" process, or whether they are the result of successive mergers between small structures in a hierarchical merging process (see the volume edited by Bender & Renzini, 2003, for reviews).

Simulations of galaxy formation in a cosmological setup need to make some simple assumptions to deal with the complex physics of the baryons. In these models, according to the prescription of the Lambda-Cold Dark Matter model (Baugh et al., 1996; Kauffmann, 1996), the galaxy structures present in the local Universe are the result of a series of merging events. In this framework the ellipticals formed from the merging of spirals occurred in recent times ($z < 1$). However, analyzing in detail the nearby galaxies to understand the properties of

their stellar and gas components turns out that this hypothesis seems unlikely in the light of the chemical and photometric differences between ellipticals and spirals. Furthermore, the (dry and wet) merger scenarios have problems in reproducing the chemical and spectrophotometric properties of local ellipticals. This suggests a very early and fast formation for these galaxies with the most massive ones forming before and with more intense star formation than the less massive ones (Pipino & Matteucci, 2004). In particular, to reproduce at the same time the increasing [α/Fe] ratio with galactic mass and the mass-metallicity relations found in ellipticals, one needs to assume a down-sizing in star formation, as described above (Pipino & Matteucci, 2006, 2008).

All these constraints seem better took into account by the "monolithic collapse" scenario. In this formation mechanism, proposed for the first time by Larson (1975) and followed then by many others (e.g. Arimoto & Yoshii, 1987; Matteucci & Tornambe, 1987; Pipino & Matteucci, 2004), the spheroids lead a quiet life, having assembled their baryonic mass at early time in a gaseous form: after a single dominant episode of star formation, it stopped after the occurrence of a galactic wind, and then they passively evolve until today.

Ellipticals galaxies are only "half of the sky" and it is not possible to improve our understanding of formation and evolution of galaxies if we do not consider disk galaxies. They are the most common class of large galaxies in the universe. In general, disk galaxies consist of two main components, a central dense bulge and an extended disk. But high resolution images show that their structure could be much more complicated by the presence of bars and different nuclear components. It has been estimated that bulges account for more than one quarter of the stars in the local universe (Driver et al., 2007), and are fundamental to galaxy evolution. Bulge size is one of the main features by which galaxies are

classified in Hubble types, with late types having low mass and low concentration bulges while early types have massive, concentrated bulges. The fraction of galactic stellar mass in the bulge constrains how galaxies evolve between Hubble types. Bulges influence the size and strength of bars (central elongated structures composed of stars found at the centers of 75% of disk galaxies), which in turn have a profound effect on the rest of the stellar and gaseous mass distribution. The formation of bulges is still poorly understood although hotly debated since understanding their formation and evolution is a necessary step for a complete picture of galaxy formation.

The relative importance of the dissipative collapse (Eggen et al., 1962; Gilmore & Wyse, 1998), major and minor merging events (Cole et al., 2000; Aguerri et al., 2001) and redistribution of disk material due to the presence of a bar or environmental effects (Kormendy & Kennicutt, 2004) drives the variety of properties observed in bulges. Comparing these observational properties with the theoretical model prescriptions will clarify the dominant formation mechanism for bulges. However, due to their complex structure, disk galaxies have been subject to much less attention and their studies are limited to the very central regions of bulges. Only for few S0 (Mehlert et al., 2003; Ganda et al., 2007) and a bunch of spiral galaxies in cluster (Peletier et al., 2007; Morelli et al., 2008) was derived chemical-composition radial-profiles. This information, as for elliptical galaxies, is expected to be a crucial constraint for the model prescriptions.

Models, however, can not neglect the contribute of the gas component of the disk when describing the bulge formation. In fact, the interplay of radial gas flows coupled with the duration of the star formation can create different situation with a variety of [α/Fe] ratio gradients as observed (Pipino et al., 2008, and references therein). Understanding gas flows and chemical evolution is even

more crucial considering spiral galaxies. Deep HI observations in spiral galaxies have shown the presence of thick gaseous layers extending to several kiloparsec from the disk plane. The amount of extra-planar gas is proportional to the star formation rate (SFR), thus suggesting an internal origin, likely being disk interstellar medium (ISM) ejected in the halo by Type II supernovae (SNe II). All the above points to a substantial gas circulation between disk and halo. The ejection of the gas out of the disk due to SNe II is usually called galactic fountain. The ejected ISM rises above the galactic plane, remaining bound to the galaxy. The extra-planar gas can form clouds via thermal instabilities and then return to the plane mixing with the disk ISM. A fraction of the metals produced by the SNe II remains trapped in these clouds and thus get recycled at some distance from the birth place. This metal circulation can have important consequences on the chemical evolution of the galaxy and in particular on the formation of the abundance gradient of the disk stellar population.

All the above topics have been pushed forward, so far, only in high surface brightness (HSB) galaxies (i.e., the galaxies which are usually adopted to illustrate the Hubble sequence). On the contrary, low surface brightness (LSB) galaxies have been less investigated. Although they are more difficult to identify than their HSB counterparts, LSB galaxies are far from occupy a niche in galactic astrophysics.

LSB galaxies are operatively defined starting from the Freeman law. The analytic expression of the Freeman law (Freeman, 1970) which describes the surface brightness of a disc is:

$$I(r) = I_0 e^{-r/h} \tag{2.1}$$

where h is the scale radius of the discs, i.e. the distance to which the central

surface brightness drops down of a factor e^{-1}, and I_0 is the central surface brightness ($r = 0$). If we express the surface brightness in unit $mag\ arcsec^{-2}$, the previous relation can be written as follows:

$$\mu(r) = \mu_0 + 1.086(r/h) \tag{2.2}$$

with $\mu_0 = -2.5 \log I_0$. The galaxies sample selected by Freeman was made by local and brilliant disc galaxies, whose discs exhibited the same deprojected surface brightness in B band $\mu_B^0(0) = \mu_B(0) - 2.5 \log(\cos i)$, with mean value $\mu_B(0) = 21.65 \pm 0.3$ mag arcsec^{-2} (Freeman law). Once established $\mu_B(0) = 22.7$ mag arcsec^{-2} as the limit for the central deprojected surface brightness for the discs, all the discs exceeding by one magnitude this limit are classified as Low Surface Brightness (LSB) galaxies, otherwise they are classified as High Surface Brightness (HSB). However the Freeman law is affected by selection bias: having been selected in the original sample all galaxies brilliant and extended, Freeman had erroneously fixed the h parameter, considering as a consequence galaxies with scale radius comparable among them. A unique value for the surface brightness in the discs cannot exists, it can be only an upper limit. Also this limit is correlated with the morphologic type, decreasing through the S0s and ellipticals. This suggests that the LSB doesn't constitute a separate class of galaxies, instead they are part of the Hubble sequence.They are likely to be the manifestation of the lower density peaks in the initial density fluctuation spectrum and span the entire range of galactic masses. They appear in a wide range of morphologies from the more populous dwarf spiral/ irregular galaxies to the most massive spiral galaxies known to date (e.g., Malin I).

There are not so many studies on the LSB galaxies and they can be divided into two classes. One is the study of surveys planned to find LSB galaxies and to

quantify a series of parameter such as their number density respect to the total galaxy number density or their luminosity density and mass density. The second class on the other hand comprises studies of the internal structure of this kind of galaxies, possibly investigating their gas content, star formation history and evolutionary processes.

The first large-area surveys examined to compile LSB catalogs were photographic surveys such as the Uppsala General Catalogue (Nilson, 1973), the POSS-2 survey (Schombert & Bothun, 1988; Schombert et al., 1992) and the APM survey (Impey et al., 1996). More recently, CCD surveys like the drift-scan survey of Dalcanton et al. (1997), or the multicolor surveys of O'Neil, Bothun, & Cornell (1997) and O'Neil et al. (1997) increased the number of LSB identified, proving that this class of galaxies is not an oddity respect the general picture. Dalcanton et al. (1997) for example concluded that the number density of LSBs were $N = 0.01^{+0.006}_{-0.005}$ galaxies $h^3_{50}\mathrm{Mpc}^{-3}$, equal to the number density of HSB galaxies. More recently de Jong & Lacey (2000) found that while the luminosity density is dominated by the HSB galaxies, the number density of galaxies is essentially flat distributed at all surface brightnesses fainter than $\mu_B(0) \simeq 21$ mag arcsec^{-2}, and therefore the LSBs constitute a significant fraction of the total number of galaxies.

A thorough study of LSB disk galaxies have been conducted by de Blok trough the years starting with his thesis (de Blok, 1997), including multicolor optical surface photometry (de Blok et al., 1995), VLA mapping of the HI distribution (de Blok et al., 1996; de Blok & McGaugh, 1997), and spectroscopy of the HII regions (de Blok & van der Hulst, 1998). The general picture obtained from these works is that LSB galaxies are metal-poor and gas-rich, with scale lengths comparable to HSBs but with much lower surface densities. However

the de Blok's selection criteria included existing HI detection. Kinematics, and therefore gravitational potentials, are dominated by dark matter at all radii and the low global star formation rates are the result of both low surface density and low metallicity.

The effects of SNe II explosion are expected to impact also the evolution of LSB galaxies, even if their star formation rate is relatively low. SF in LSB galaxies appears to be concentrated in few compact sites, while most of the disk is quiescent (McGaugh & Bothun, 1994). The low HI surface density, indeed, implies that the neutral gas cannot easily gather round to form giant molecular clouds and consequently in these galaxies it is not possible to form stars from these clouds, as it occurs in HSB galaxies. This so-called sporadic star formation generates fluctuations of alpha elements abundance, unless the heavy elements are efficiently mixed on scales larger than 1-2 kpc (e.g. Vorobyov et al., 2009). Even if these galaxies show brilliant HII regions, indicative of ongoing stellar formation, they still exhibit a star formation rate at least an order of magnitude lower respect to the HSB galaxies. The star formation could take place in an environment of more diffused HI gas instead of giant molecular clouds, making the surface brightness low. Typically a significative ultraviolet flux is not observed, but blue colors are rather high suggesting the probable presence of a young stellar population, which translates in a younger age respect to the HSB galaxies. This suggest that the formation of these galaxies could have occurred in late respect to the other galaxies.

A large scatter in the Tully-Fisher relation among LSB galaxies was found by Burkholder et al. (2001), who had available photometry, HI spectroscopy and low-resolution optical spectroscopy for a sample of 250 LSBs from the catalog of Impey et al. (1996). They also used emission line ratios to measure the

metallicity for a subsample of the observed objects, divided in HSB and LSB galaxies (defined $\mu_B = 22$ mag arcsec^{-2} as limit between the two groups), and found there to be a roughly 50% overlap in the metallicity range of the two groups.

Although most of the LSB galaxies are bulgeless, there are also galaxies with a LSB disks and a significant bulge component (Beijersbergen et al., 1999; Pizzella et al., 2008). Sprayberry et al. (1995), by studying photometry, low-resolution spectroscopy and HI spectroscopy for a small sample of giant LSB, found that there are no differences between the bulges of these large LSB and HSB galaxies. An important question, is whether many of these bulges hosted by disks with low stellar density are high surface brightness bulges embedded in LSB disks. In such a case, the bulge could evolve independently with respect to the disk, and one should expect that bulges in LSB disks are characterized by the same metallicity of the bulges of HSB galaxies. On the other hand, the secular evolution of galaxies, allowing the direct formation of bulges from disks in isolated galaxies, implies that the stellar population of disks is similar to that in bulges. For example, one can expect that abundances gradients are mild or even inverted from the center to the outskirts of the galaxy.

Because of the low surface brightness, deep spectra for the stellar disks of the LSB galaxies are difficult to obtain and it requires large amounts of telescope time. The brightest objects in a LSB are generally the HII regions, where the bright emission lines make them more easily observable than the underlying continuum. For this reason, while the analysis of the emission lines in the spectra of LSB galaxies allowed the measure of the current gas phase metallicity, the properties of the underlying stellar population, as obtained from the absorption lines, have been rarely determined. Bergmann et al. (2003) for example, obtained

low-resolution spectra for 19 red and blue LSB galaxies, and used combination of emission line and absorption line based diagnostics to investigate the star formation and chemical enrichment histories of these galaxies. They found that they were diverse, with some galaxies having low metallicity and young mean stellar ages and other galaxies showing old, supersolar-metallicity stellar populations. Also, in contrast with previous studies which found strong trend of decreasing metallicity with decreasing central surface brightness, they found galaxies with low surface brightness but near-solar metallicity.

As discussed so far, authors do not agree about the nature of LSB galaxies. Even if they appear to be different, several studies pointed out that LSB may not constitute a different class of objects respect to HSB galaxies, showing instead the same characteristics. The peculiar characteristics of the LSB with respect the normal HSB galaxies make them a perfect laboratory and a unique opportunity to learn different aspects of the formation and evolution of galaxies.

Aim and scheme of the thesis

The aim of this thesis is to study the gas metallicity in galaxies by mean of the Hβ, [OIII] and [OII] emission lines.
The thesis is divided into two parts as described in **chapter 1** and **2**:

- in the first part we will focus on the study of a sample of galaxies in the low-intermediate redshift range between 0.3 <z< 0.6 and spanning an interval of 5 mags in luminosity, from M_B=-16 to M_B=-21. We will extract the equivalent width for the emission lines visible on their spectra and we compute the integrated R_{23} parameter. We will investigate for correlation between spectroscopic metallicity diagnostic and photometric properties, also studying a large comparison sample of nearby galaxies for which are available in literature both the R_{23} and [NII]/Hα measurements.

- in the second part we will focus on Low Surface Brightness galaxies. We will analyze the spectra of a small sample of nearby LSBs for which we have available long-slit spectroscopy. The quality of the data and the closeness of the objects observed allow us to obtain measurements of the ionized gas metallicity as a function of the distance from the nucleus, ever obtained for LSB galaxies so far.

In addiction to this, in the **Appendix B** it is reported a paper published on A&A in 2009, during the PhD studies, concerning the discovery of an UV flare at the center of the elliptical galaxy NGC 4278.

In **chapter 3** we present the data observations and the procedure adopted to extract from the full sample the objects at redshift 0.3 <z< 0.6, whose spectra showed the lines necessary to perform the subsequent analysis. Also there are presented the literature data used to investigate the presence of a correlation

between the metallicity diagnostic and photometry.

In **chapter 4** we describe the method used to measure the metallicity estimators and the associated errors.

In **chapter 5** we discuss correlation tests performed in search of a connection between these estimators and the photometry and we compute the metallicity of the objects.

In **chapter 6** there are presented the data available for the Low Surface Brightness galaxies and all the preliminary reduction steps performed to obtain scientific analyzable data.

In **chapter 7** there are described the procedures used to extract the radial information about both the gas and the stellar component.

In **chapter 8** it is described how the metallicity estimates have been obtained at each radius and there are discussed the results.

In **Appendix A** there are reported the values of the metallicity estimators and metallicity obtained at each radius for the low surface brightness galaxies studied in the second part of the thesis.

Part I

Gas metallicity in distant galaxies

Chapter 3

Data acquisition and reduction

3.1 Sample selection

3.1.1 Vimos observations

In 2006 Yegorova I., Salucci P. and Pizzella A. obtained observation time at the Very Large Telescope for a proposal whose aim was to find satellites in a region of about 500 kpc surrounding isolated spiral galaxies (Yegorova et al., 2011, ESO program IDs 075.B-0794 and 077.B-0767). Satellites can be used, by mean of their radial velocity, to probe the distribution of dark matter at very large radii for the sample galaxies. It was planned a spectroscopic survey of the region of approximately 500 kpc around 7 isolated spiral galaxies. The instrument chosen for the survey was the Visual Imager and Multi Object Spectrograph, VIMOS, mounted at the Nasmyth B focus of the ESO UT3 telescope at Paranal, setted in its Multi Object Spectroscopy mode, MOS. VIMOS-MOS observations, indeed, allow to distinguish the satellites of the primary galaxies among the extra galactic targets present in each field, and to measure their radial velocity. All the targets have been selected from the Sloan Digital Sky Survey. They are isolated and are

known to have a number of satellites.

VIMOS-MOS has available several grisms that allow observation both with Low resolution and High resolution, with different wavelength coverage from 3700 Å to 8750 Å. In our case the HR-Orange grism has been used. It allows a wavelength range from 4550 to 8400 Å, depending on the position of the slits relative to the center of the field of view, along the dispersion direction. The spectral resolution is 2150, while the dispersion is 0.6 Å/pix. The target galaxies where selected to be non interacting with other objects in a region of about 500 kpc from their center. For each of the four quadrant of the camera a mask was created with a number of slits of approximately 50. The exposure time for 6 of the 7 targets was 10900 sec. In the remaining case the exposure time is limited to 4300 sec due to bad atmospheric conditions during the observation. There were observed 1347 objects in all the 7 fields.

The set up of the instrument described, makes accessible observations of objects that lie in the redshift range $0.3 < z < 0.6$, which allows the simultaneous acquisition of the line necessary to compute the R_{23} parameter. However the slits are placed on the masks almost casually, in the sense that the objects selected, even if present in the SDSS archive, reside at unknown distances.

A preliminary analysis of just one quadrant (in fig. 3.1 an example of the acquisition images obtained) revealed the presence of 4 objects in the redshift range useful for our purpose, so we decided to analyze the full dataset, in order to collect the largest data sample possible. We also searched the ESO archive for similar observations, but we did not find useful data. We were indeed interested in long exposure times, in order to have signal level high enough to reveal objects at $z \simeq 0.5$, and to measure their emission lines fluxes.

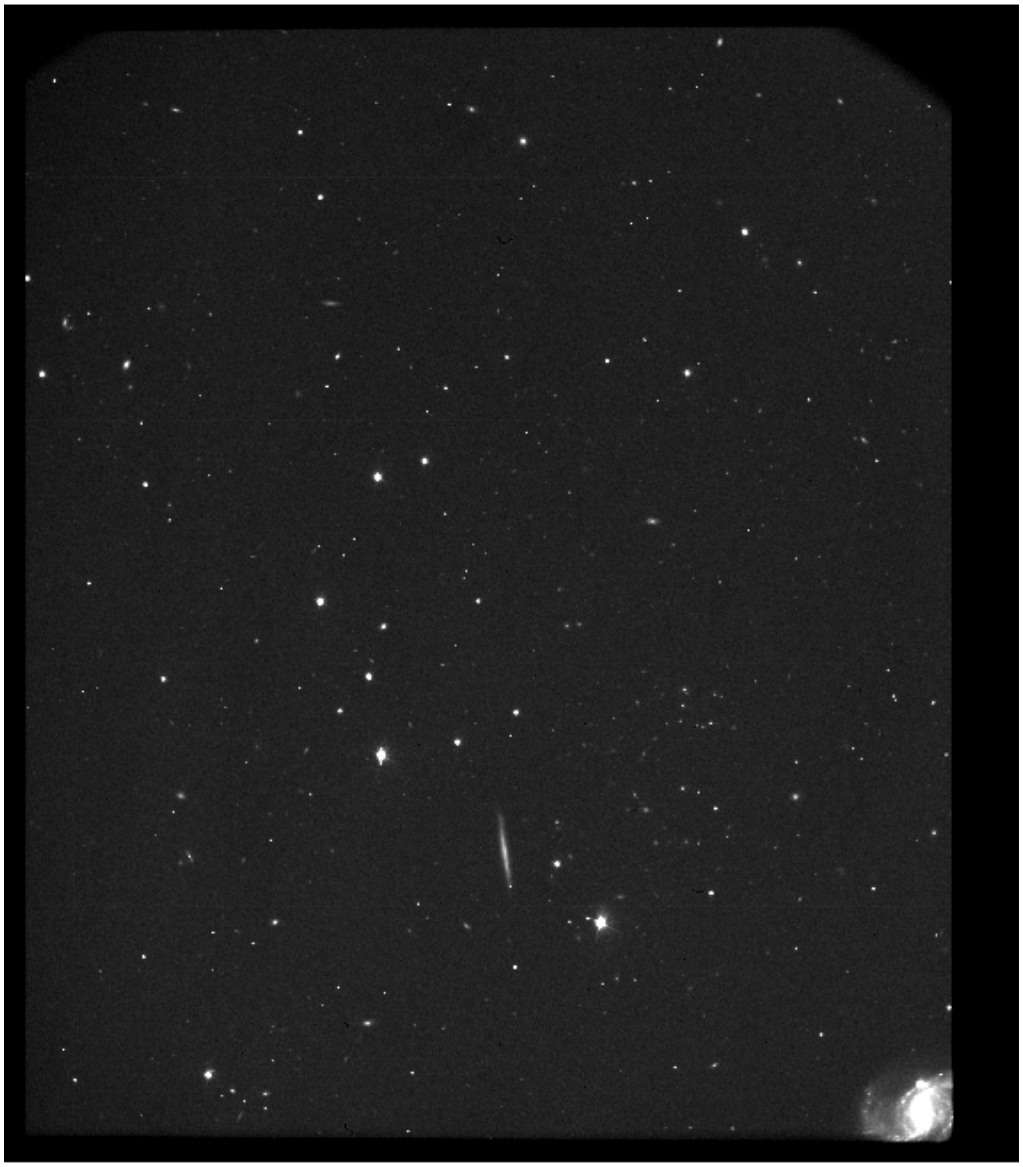

Figure 3.1: Example of acquisition image obtained with VIMOS. The image is relative to only one of the four quadrants that constitute the instrument. The center of the full detector is bottom right.

3.1.2 Literature data

Our data exhibit a spectral range capable of showing simultaneously the lines necessary to measure the R_{23} parameter or in some cases the Hα region, but never both for the same galaxy. For this reason we decided to compare our measurements with a catalog of galaxies for which both these regions were available. Furthermore the objects in this catalog should be part of the SDSS Archive, in order to compare the same kind of photometric information, i.e. magnitudes and colors.

We searched the literature in order to find such a catalog and, at the time of this study, we found the collection of data presented by Nagao and collaborators in a study of gas-metallicity in star forming galaxies (Nagao et al., 2006). The complete sample is a collection of heterogeneous data taken from previous studies and consists in two subsamples of data both at high and low metallicity.

As for the sample of low metallicity, it is composed by two groups of data. The first is a selection of the spectra analyzed by Izotov et al. (2006) in a systematic study of the oxygen abundance for low-metallicity galaxies in the SDSS Data Release 3 (DR3, Abazajian et al., 2005), by means of the [OIII]λ4363 emission-line flux. In particular there were selected those spectra with a relatively small error in the oxygen abundance [$\Delta(log\frac{O}{H}) \leq 0.05$]. The second is a collection of data of galaxies with a [OIII]λ4363 measurements from the literature. For these objects, in order to minimize possible systematic errors due to the different methods used in the calculation of the oxygen abundace, the latter has been re-calculated by adopting the same method used in Izotov et al. (2006).

As for the sample of high-metallicity, they referred to the oxygen abundances derived by Tremonti et al. (2004), selecting about 48000 objects from their oxygen-abundance catalog of the SDSS Data Release 4 (Adelman-McCarthy et

al., 2006).

For our study we used a subsample of this large collection of data, with a number of object somewhat smaller than the catalog showed in Nagao et al. (2006). This is because all the object now have both R_{23} parameter and [NII]/Hα ratio measurements, while the objects in the paper may have only one of various emission-line flux ratios (Nagao, private communications). The final sample consists of approximately 25000 objects, of which about 150 at low-metallicity and the rest at high-metallicity. For these objects there are available measurements of R_{23}, [NII]/Hα and metallicity, as shown in figure 3.2, and we also know all their identification number in the SDSS Archive (necessary to retrieve the photometry from the archive).

3.2 Data reduction

Being the data obtained from the archive, they were already processed through the VLT-VIMOS pipeline[1]. The pipeline process includes all the steps necessary to produce scientific data starting from the raw observations.

First of all bias subtraction is applied, overscan regions are removed and flat-fielding applied. Bias, as known, is added to the image at the acquisition stage in order to avoid the statistical fluctuation of counts be negative. Dishomogeneities over the surface of the detector can cause different quantum efficiency in different region. For this reason the images or spectra acquired are altered by artifacts that make the observed energy distribution on the sensor different form the reality. This effect is corrected by analyzing the spectrum of a well known homogenous light source, the flat field. After these corrections, the response of the whole

[1] All the discussion below is made assuming that, being the observations performed in 2006, the scheme of data obtained is the output of the pipeline used until 2010. That is slightly different form the actual one.

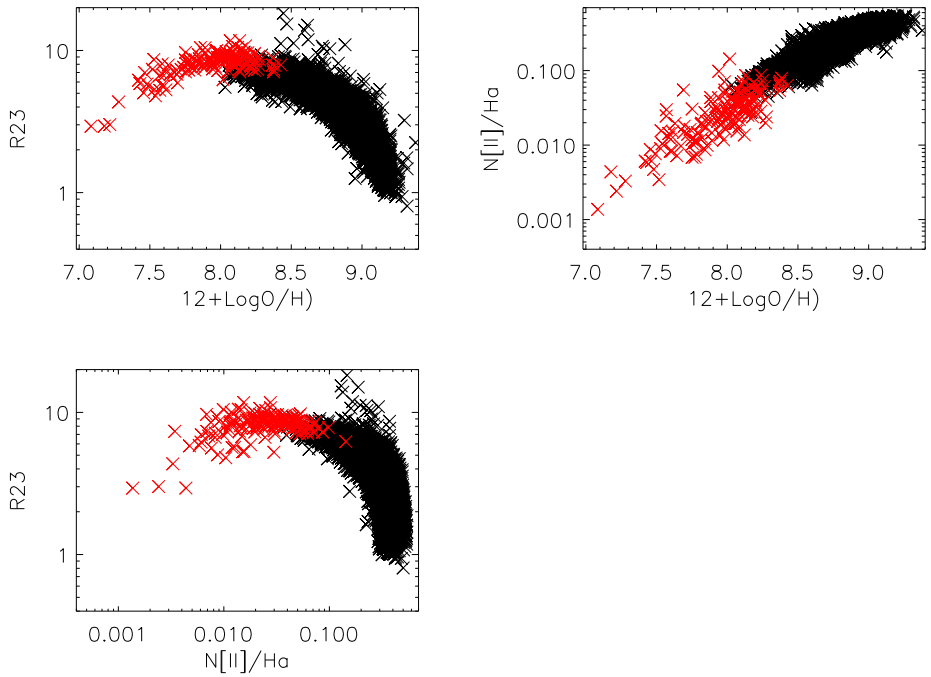

Figure 3.2: Gas metallicity diagnostics for the literature comparison sample. The measure are taken from Nagao et al. (2006). Red points refer to the 150 objects ot low-metallicity.

sensor is the same in every part of it and we can measure in consistent way the counts received by each pixel. Optical distorsion are also corrected by remapping the slit spectra, which are afterwards wavelength-calibrated using the wavelength calibration lamp and sky lines spectra observed during the same observation run. Consecutively the sky background is subtracted from the spectra. Being available in our case more than one exposure for target, each frame has been aligned to the first one and stacked to obtain the final spectra, with the cumulative exposure time. At this point objects are extracted from the spectra using an optimal extraction algorithm (Horne, 1986).

3.2.1 Redshift computation

The wavelength calibration of the VIMOS-MOS data rearranges the spectra observed in each of the four quadrants/masks, in a single two dimensional mosaic of spectra (see figure 3.3). Each mosaic is composed by the two dimensional spec-

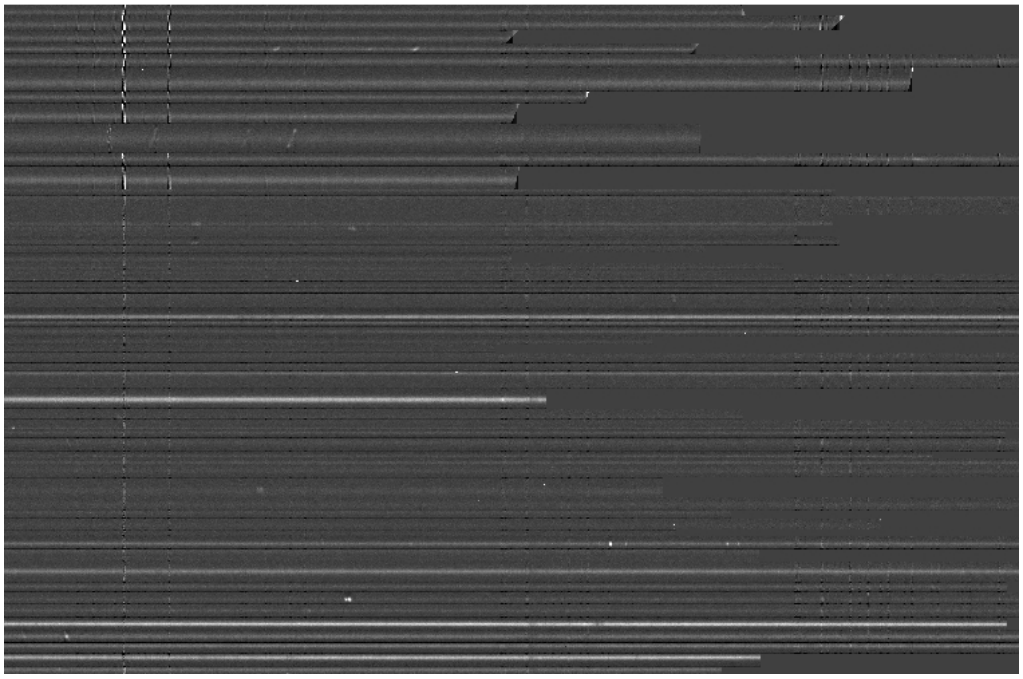

Figure 3.3: Example of the mosaic of spectra obtained as result of the Vimos pipeline. The figure shows only a section of the full image but it is clearly visible the different spectral range covered by each slit.

tra obtained from the various slits, positioned one above the other and aligned along the dispersion axis on the basis of the wavelength calibration earlier performed. Of course, depending on the position of the slit on the mask, this kind of mosaic provides spectra ranging in different wavelength intervals, which are consequently placed in different position along the dispersion axis on the mosaic itself. In addiction, all the objects observed reside at different unknown redshift, therefore the features we are searching will be placed in completely casual posi-

tion on the mosaic. This becomes a limit for our possibility of detecting useful data: an object potentially in the correct redshift range can indeed have been observed in a spectrum too red or too blue to show all the features requested, making the spectrum itself unusable for our purpose.

Our analysis starts with the identification of the redshift for all the objects observed. The features we are looking for, i.e. [OII]$\lambda\lambda$3726, 3728, [OIII]$\lambda\lambda$4959, 5007 and Hβ, if present, are brighter than the rest of the spectrum and well visible over the background level. Also they show a very easy and recognizable pattern so that we can use all these characteristics to identify the redshift of the majority of the objects. Unfortunately the visual inspection of the spectra is the most easy an probably accurate way to identify all these features, or at least some of them, onto the spectra. A completely automated algorithm should in fact take into account too many variables in order to be able to recognize the features in a sample, such the one we have, in which redshift and extension of the spectra themselves are so different and casual. Furthermore we are interested only in those objects that can show all the emission lines we have discussed before, making useless the identification of the redshift in all the other cases. For this reason, it would be an unreasonable waste of time try to create such a kind of algorithm.

We therefore developed an *IRAF*[2] procedure that allow us to compute the redshift only for the spectra where we detect, by visual inspection, well known emission lines.

Besides the spectra in which we detected the emission lines necessary for our analysis, there were a number of spectra showing the other easily recognizable

[2]Image Reduction and Analysis Facilities is distributed by the National Optical Astronomy Observatories, which are operated by the Association of Universities for Research in Astronomy, Inc., under cooperative agreement with the National Science Foundation.

pattern formed by the [NII]$\lambda\lambda$6548, 6584 and Hα lines. Also for these spectra we measured the redshift. In all the other cases, that means in all the spectra where no clear emission line was detected, no distance measurement was performed and the spectra were immediately rejected.

There have been observed 1347 spectra. Approximately half of the objects showed recognizable features (i.e. oxygen, hydrogen or nitrogen lines) that allowed us to measure the redshift. Each line has been fitted independently with a gaussian profile whose center, in wavelength units, has been converted to *cz*. If the lines identified were the correct ones, the redshift measured had to be the same for all the lines visible in the same spectrum. In this case we averaged the redshift obtained from all the lines to obtain its best estimate. If this was not the case, it meant that some lines were not correctly identified and we proceeded again with their identification.

We were able to measure the redshift for 637 object, and they all lie in the range between $z = 0.03$ and $z = 0.91$. Only 37 objects simultaneously showed the oxygen and hydrogen lines necessary to compute the R_{23} parameter. In figure 3.4 we show the frequency distribution of all the redshift determined (in black), divided in interval of $z = 0.03$. The red-hatched histogram highlights the distribution of the 37 objects showing all the lines necessary to our analysis.

3.2.2 Coordinates' extraction

When the VIMOS instrument is used in its Multi Object Spectrograph configuration, users customize the mask by placing the requested number of slits in the position and orientation required.

As product of the pipeline we obtain two different tables, the *SOTM* and *SWTM* files, respectively the OBJECT_TABLE and the WINDOW_TABLE,

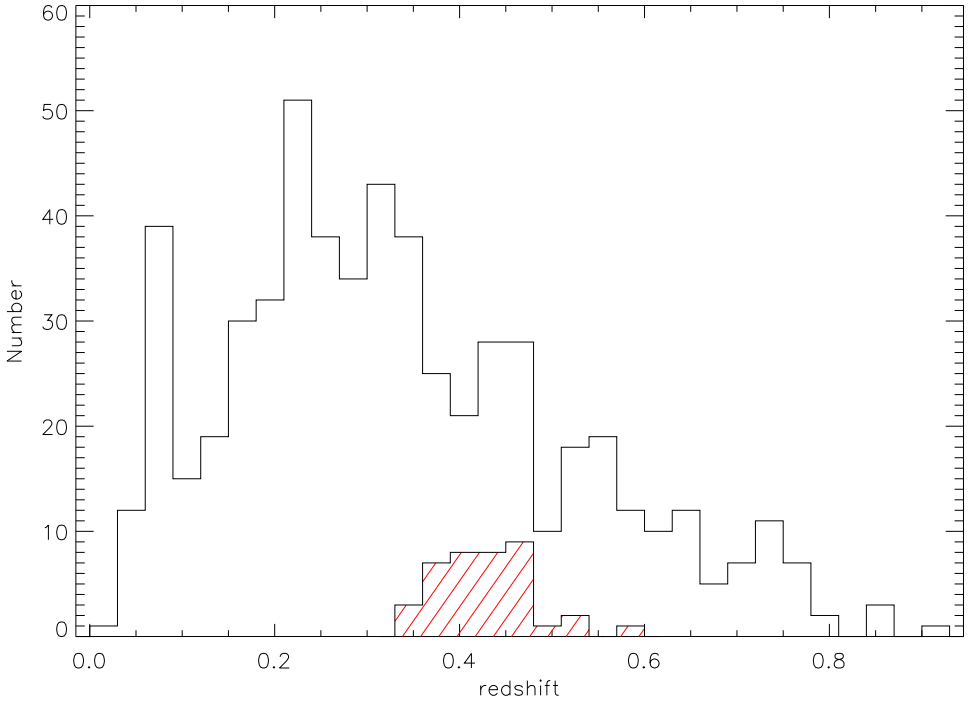

Figure 3.4: Frequency distribution of the redshift for the 637 galaxies identified. The red-hatched histogram is relative to the subsample of 37 objects showing both [OII]λ3727, Hβ and [OIII]$\lambda\lambda$4959, 5007 lines.

for each of the four sensor of the instrument. The former refers to the one-dimensional extracted spectra (that we didn't use for our work, so here ignored) while the latter refers to the two-dimensional extracted spectra. It contains several information about the position of the objects in the slits, as reassumed in table 3.2.2, but no direct information about the celestial coordinates of the objects observed.

Besides to this file, information about each slit of the mask are also added to the header of the scientific extracted spectra. For each slit there are saved the X and Y coordinates, sizes in mm units relative to the center of the mask,

column name	description
SLIT	slit number
SPEC_START	pixel position (Y) of the first row of the slit extracted
SPEC_END	pixel position (Y) of the last row of the slit extracted
OBJ_NO	sequential number of the object in slit (they can be more than one)
OBJ_START	pixel position (Y) of the first row of object relative to SPEC_START
OBJ_END	pixel position (Y) of the last row of object relative to SPEC_START
OBJ_POS	pixel position (Y) of object relative to SPEC_START
OBJ_X	mask X coordinate of object in mm units, relative to the center of the mask
OBJ_Y	mask Y coordinate of object in mm units, relative to the center of the mask

Table 3.1: Content of the WINDOW_TABLE files, available for each quadrant.

the shape of the slit and an identification number. Also there are the RA and DEC of the object (see table 3.2.2). However, for what concern the equatorial coordinates, these are correct only if the system (i.e. the pipeline) identifies an object inside the correspondent slit. Unfortunately, the automatic procedure is not always able to detect the object, especially when the signal of the source is very low respect to the sky background.

```
...
HIERARCH ESO INS SLIT1 TYPE     = RECTANGLE   / Type of SLIT i
HIERARCH ESO INS SLIT1 ID       =   432       / ID of SLIT i
HIERARCH ESO INS SLIT1 OBJ RA   =   0.000000  / RA (J2000) of object
HIERARCH ESO INS SLIT1 OBJ DEC  =   0.000000  / DEC (J2000) of object
HIERARCH ESO INS SLIT1 X        =   50.516000 / x co-ordinate of SLIT i
HIERARCH ESO INS SLIT1 Y        =   5.954000  / y co-ordinate of SLIT i
HIERARCH ESO INS SLIT1 DIMX     =   3.575000  / Size in x direction of SLIT i
HIERARCH ESO INS SLIT1 DIMY     =   0.523000  / Size in y direction of SLIT i
...
```

Table 3.2: Example of the information on the slit position stored in the header of the spectra.

Since we are interested in obtaining the photometric observation collected in the Sloan Digital Sky Survey Archive, we need to know the position in the sky

of the objects here observed. In particular we need the coordinates of the only objects lying in the correct redshift range to measure the R_{23} parameter. In many cases the pipeline, as mentioned before, was not able to identify anything as object inside the slits even though clear features were recognizable, making the information stored in the headers incomplete and useless to automatically extract the coordinates. Furthermore we did not have available the original list of targets observed within each mask, with their position in the sky and the correspondent position of the slit in the mask.

For these reasons we needed a way to convert the X and Y coordinates given in mm units and stored in the SWTM files into the equatorial system, and we developed a semiautomatic procedure to this aim. As result of the redshift measure we have available for each telescope pointing four tables containing the redshift of the object identified and the ID number of the slit in which it was found. These tables were matched with the WINDOW_TABLE files and with the list of the only object selected to the following analysis, in order to obtain the X and Y coordinates of these objects. We have a number of tables equal to the number of pre-images obtained during the observations. We coupled each coordinates list to the respective pre-image. We converted them to the image-system coordinates (that is in pixel) and we associated to these position circular marks that would help in the identification of the objects. We displayed all the pre-images with the superimposed marks and, since the display program is able to automatically switch between different system of coordinates included the equatorial one, we have finally been able to obtain the sky coordinates of all our selected objects.

Chapter 4

Data Analysis

4.1 Measure of the equivalent widths

The 37 two dimensional spectra selected from the complete data set, have been now examined in order to find and, if needed, fix possible problems in the measurement of the fluxes.

When a large number of objects is observed, as it is in our case with multi object spectroscopy, it is statistically easier to introduce errors in the observations themselves in respect to the case in which few objects are studied. In our case for example, both the position, rotation angle and length of the apertures are decided by the observer, and there are afterwards placed on the real mask. Human error is not negligible as well as the possibility that an error can occur when the software or the hardware create the mask: this for example translates in possible mis-aligment between the center of the object observed and the aperture centered on it. For this reason it was essential check if these kind of problem had affected our selected spectra.

The majority of the spectra were correctly acquired but in some other cases

we found clear faults.

In one case the spectrum was damaged, probably due to some problems in the reading stage of the CCD. It showed several lines, 2 to 5 pixels large, of bad pixels along the dispersion axis, placed just above the signal of the galaxy, in two different positions, making impossible to recover the real counts number in those regions.

In a couple of cases the spectra were incomplete along the direction perpendicular to the dispersion axis. In this case probably the problem is due to a mis-alignment between the center of the aperture in respect to the center of the object, as we mentioned before. In the first case described the spectrum was damaged artificially during or after the acquisition itself, in this second case we have an error in the "pointing" of the source, making again impossible to recover the missing information.

In other cases the spectra appeared correctly acquired, but the position of the emission lines made them unusable: because the [OIII]$\lambda\lambda 4959, 5007$ lines fell on a region of the spectrum contaminated by strong night-sky lines, or because even if the redshift of the object was correct, unfortunately their spectral range ended just before these lines.

In all these cases we decided to reject the spectra, obtaining therefore a final sample of 29 objects.

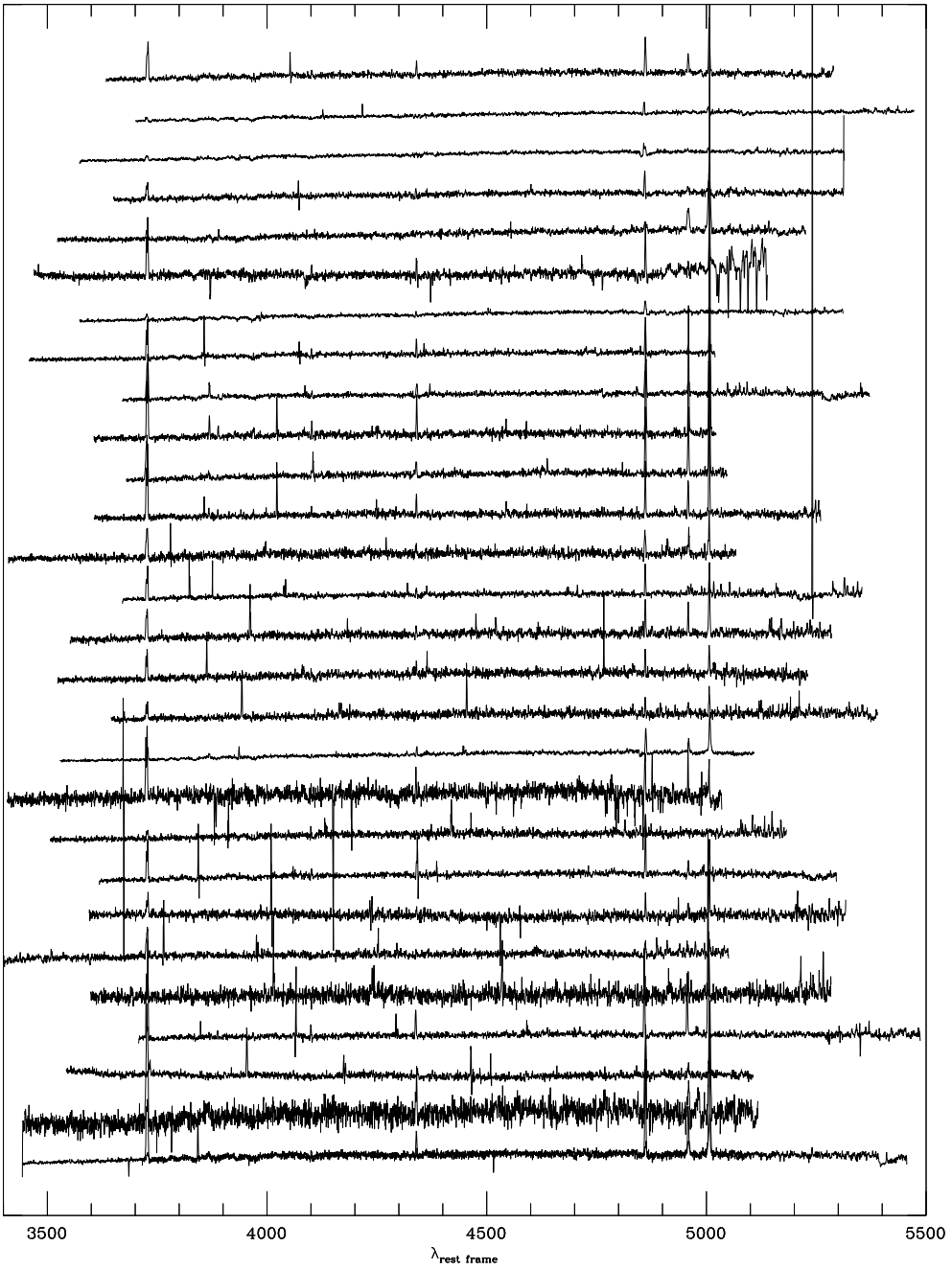

Figure 4.1: All the spectra selected from the full datasample, moved to rest-frame. The spectra are arbitrarily placed along the y-axis.

Due to the distance of the objects and to the instrumental setup, the entire signal of the galaxies selected is confined in a region of few pixels perpendicularly to the dispersion axis. For this reason it was not possible to make a study of the radial distribution of the gas metallicity from the center to the external regions. However, being interested in studying the global properties of these objects, we measured the total flux emitted by them in the emission lines of interest. To this aim we extracted a one dimensional spectrum for each object, by summing all the flux enclosed in appropriate apertures, and we used them in the following analysis (these spectra are showed in figure 4.1).

Generally, the abundance of chemical elements in a galaxy can be estimated if information about the emission lines emitted by nebulae are available. The strongest emission lines observable in visible and ultraviolet spectra are the hydrogen recombination lines, helium, and forbidden lines of carbon, nitrogen, oxygen, neon and sulfur. The relative strengths of these emission lines, in combination with information about the temperature and the density of the regions considered, can provide information about the relative and absolute abundance of each ion. It is sometimes possible to obtain precise measure of the relative fluxes of the emission lines, but nowadays it is increasingly common to obtain data that are not flux calibrated, especially for wide field spectroscopic surveys or multiobject spectrographs. Furthermore, for redshift greater than $z \simeq 0.3$, the Hα line is no more available (from ground based observations, in the visible) and the Hα/Hβ ratio commonly used to determine the reddening cannot be used, and cannot even be replaced with higher order Balmer lines, due to the low signal-to-noise ratio that these galaxies generally manifests.

Rather then fluxes, equivalent widths can be measured and used to extract information about the chemical composition. As described by Kobulnicky &

Phillips (2003), even if in general it would be preferable obtain metallicities from flux calibrated emission lines, equivalent width also works reasonably well for relatively faint, intermediate-redshift galaxies, as in our case (as showed in figure 4.2).

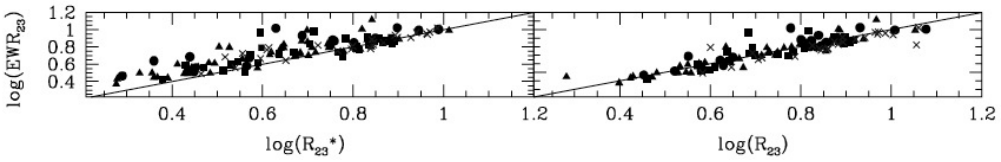

Figure 4.2: Comparison between R_{23} obtained from calibrated fluxes and equivalent widths, as showed in Kobulnicky & Phillips (2003). Even if the correlation is stronger between R_{23} corrected for reddening and EWR_{23} (right panel) , the strong correlation between R^*_{23} (uncorrected for reddening, left panel) and the EWR_{23} suggests that oxygen abundances can be estimated from equivalent width ratios as well as from dereddened line fluxes.

In this method the underlying stellar continuum is used as a raw flux calibrator. A great advantage in using equivalent widths is that any influence of reddening effects on star and gas, is equally removed.

If we consider a particular emission line delimited by λ_1 and λ_2, with center at wavelength λ, being $F_c(\lambda)$ the continuum level at that lambda and $F_l(\lambda)$ the emission line flux, the equivalent width is defined as follows:

$$EW = \int_{\lambda_1}^{\lambda_2} \left(\frac{F_l(\lambda)}{F_c(\lambda)} - 1 \right) d\lambda \tag{4.1}$$

For each line of interest, i.e. Hβ, [OIII]$\lambda\lambda 4959, 5007$ and [OII]$\lambda 3727$, we selected two regions surrounding the central wavelength, one on the blue side and the other on the red. These bandpasses need to be located near the emission line bandapass, and possibly in regions of less absorption or contamination from other structures, in order to select a flat continuum level flanking the emission line.

For these two continuum regions we computed the representative value of flux as follows:

$$F_{b,r} = \int_{\lambda_1^c}^{\lambda_2^c} \frac{F(\lambda)}{(\lambda_2^c - \lambda_1^c)} d\lambda \tag{4.2}$$

where $F_{b,r}$ represents alternatively the pseudo-continuum level of the blue and red bandpasses, and λ_1^c and λ_2^c are the wavelengths chosen as limits for these continuum bandpasses. We consider also a representative value for the wavelength of these pseudo-continua, and it has been fixed as the midpoint of the $[\lambda_1^c, \lambda_2^c]_{b,r}$ intervals. We then interpolated a straight line between the two pseudo-continua in order to obtain the continuum level (F_c) underlying the emission line.

In table 4.1 are listed the intervals selected to be the continuum regions surrounding each emission line of interest, and the central bandpass of the lines themselves. In figure 4.3 the same regions are showed both with the λ_1^c and λ_2^c limits, the pseudo-continua calculated and the underlying continuum level as resulted from our interpolation.

Feature measured	Blu continuum	Central bandpass	Red continuum
[OII]λ3727	3702.00 − 3717.00	3718.00 − 3736.00	3738.00 − 3753.00
Hβ	4827.88 − 4847.88	4847.88 − 4876.63	4876.63 − 4891.63
[OIII]λ4959	4885.00 − 4935.00	4948.92 − 4968.92	5030.00 − 5046.00
[OIII]λ5007	4885.00 − 4935.00	4996.85 − 5016.85	5030.00 − 5046.00

Table 4.1: Rest frame wavelength intervals defined in the measurement of the emission line equivalent widths, and relative continuum level. All numbers are given in Å units.

The error associated to the measure of the equivalent widths has been calculated by mean of Monte Carlo technique.

Consider that a physical phenomenon to be studied is describable using a math-

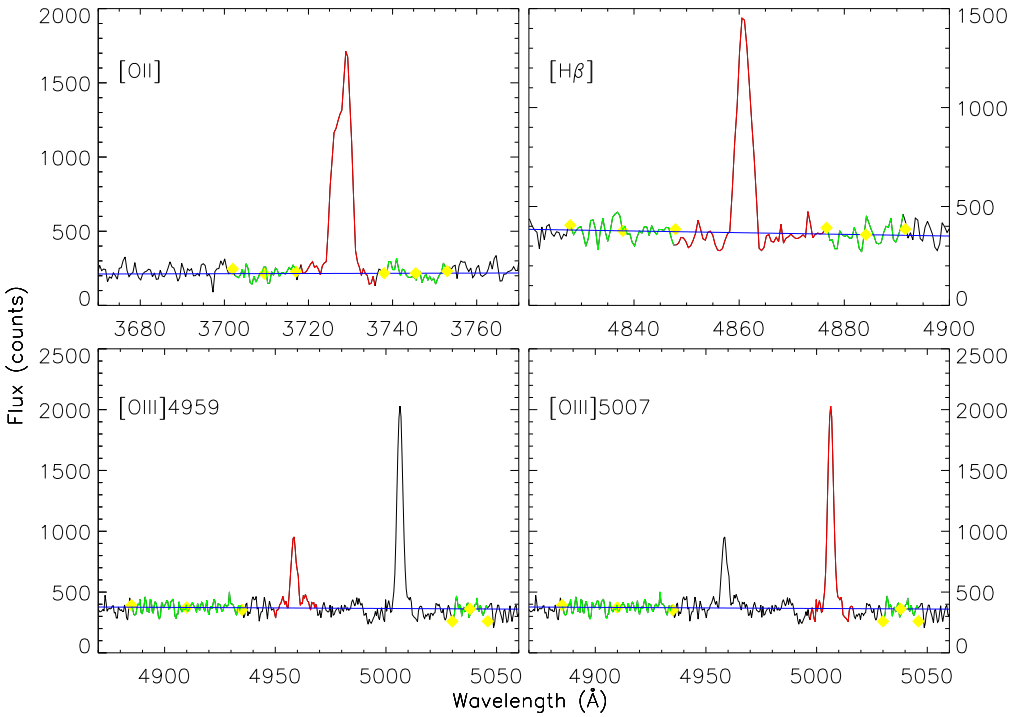

Figure 4.3: Regions selected to measure the flux of the four emission lines available for the computation of R_{23}. Superimposed to the spectrum there are the blue and red continuum regions flanking the emission line (in green), the emission line region (in red) and the continuum underlying the emission line as obtained by the interpolation (blue straight line). Yellow points are the λ_1^c, λ_2^c and representative wavelength of the pseudo-continua. The definition of the intervals are reported in 4.1.

ematical model determined by a number of parameters $\mathbf{a}$. Let $\mathbf{a}_{true}$ the true values of model parameters, unknown to the observer. Suppose, for an experiment, the data set obtained by measuring D_0 returns a corresponding set of parameters $\mathbf{a}_0$. These will differ from $\mathbf{a}_{true}$ due to the accidental and systematic errors, furthermore the series of data obtained is non the only possible: repeating the experiment (and the measures) N times, we get N different sets of data D_i, each with a corresponding set of parameters $\mathbf{a}_i \neq \mathbf{a}_0$.

The knowledge of the $\mathbf{a}_{true}$ values, could allow us in establishing the errors

to be associated to the parameters **a** measured by studying the distribution $\mathbf{a}_i - \mathbf{a}_{true}$. Let now imagine that $\mathbf{a}_0$ are the real parameters, and assume that the distribution $\mathbf{a}_i - \mathbf{a}_0$ follow the same trend of the unknown one $\mathbf{a}_i - \mathbf{a}_{true}$. It is often not possible to repeat the experiment under the same initial conditions, so that you have to use synthetic data sets D_i^s. These synthetic series must have the same size as the series measured initially (D_0) and must be obtained by generating random numbers from D_0.

Let now consider a series of N data (x_i, y_i) distributed according to a gaussian law $g(x)$ around a mean value m with standard deviation σ. We can calculate the $g(x_i; m, \sigma)$ values of the distribution function corresponding to the measurements obtained. To these values it is added a statistical noise r_i different point by point, with the condition that the new distribution obtained remains characterized by the same signal-to-noise ratio of the starting distribution. The new distribution $(x_i, g(x_i; m, \sigma) + r_i)$ is the synthetic series, characterized by the parameters m_s and σ_s.

Starting from the parameters used to measure the equivalent width of the Hβ, [OII]λ3727 and [OIII]$\lambda\lambda$4959, 5007 lines, a synthetic spectrum $I_S(\lambda)$ of emission lines is created, which of course would be characterized by a new set of parameters. This is compared with the original spectrum to obtain the residuals.

Standard deviation of the distribution of the residuals, *rms*, is then computed: it represents the noise caused by the signal of the galaxy, the sky background, the read out noise (RON) and all the operation performed to obtain the final reduced scientific data.

For each emission line it is added some noise, related to the generation of a casual number R_λ following a Poisson distribution, with mean value $I_S(\lambda)$. This noise il related to the photon flux hitting the detector and to the number of

counts determined by the latter. To this the contribution coming from the sky and that one coming from the calibration procedures is to be added. In practice, to the spectrum, at every λ it is added a "casual" noise distributed as a Poisson distribution with mean *rms*.

We generated 1000 different synthetic spectra $I_S(\lambda)$.

For all these spectra it is performed the measurement of the equivalent width as done for the original spectrum, obtaining 1000 different measure of the parameter. A statistic study is performed over the distribution of the measurements obtained, and the standard deviation is chosen to be the error associated to the measure of the equivalent width of each line.

Equivalent widths and the associated errors are reported in table 4.2.

SDSS name	[OII]	Δ[OII]	Hβ	ΔHβ	$[OIII]_{\lambda4959}$	$\Delta[O\ III]_{\lambda4959}$	$[OIII]_{\lambda5007}$	$\Delta[OIII]_{\lambda5007}$
SDSS J003845.31+000006.8	4.110	0.326	0.424	0.564	9.068	0.394	26.517	0.424
SDSS J003838.68+000225.1	57.907	0.442	25.698	0.588	15.289	0.476	44.592	0.679
SDSS J003806.59+000421.9	56.367	9.756	16.199	1.921	8.071	1.121	44.614	1.281
SDSS J134235.94+014424.1	3.826	0.384	3.435	0.645	2.431	0.616	9.084	0.664
SDSS J134229.37+015244.5	56.136	0.679	22.911	0.282	15.708	0.488	45.117	0.699
SDSS J134155.68+015530.8	-0.349	0.848	-0.677	2.653	2.029	0.706	8.586	1.558
SDSS J134154.75+014759.0	12.323	0.358	-1.423	0.442	1.010	0.579	2.335	0.710
SDSS J134156.84+014241.0	6.551	0.484	4.336	1.422	4.535	0.924	12.136	0.841
SDSS J145221.51+043448.8	24.805	0.348	9.426	0.547	0.077	0.430	4.728	0.354
SDSS J145150.75+044111.6	6.583	0.396	5.143	0.523	2.188	0.639	2.846	0.425
SDSS J145147.24+043654.2	30.379	0.935	8.017	3.104	6.047	1.614	5.991	1.172
SDSS J145156.20+043321.7	8.225	0.547	0.841	0.089	4.443	0.342	14.827	0.316
SDSS J145147.77+043244.5	12.367	0.652	2.070	1.257	3.015	0.666	5.340	0.859
SDSS J145149.20+043501.6	15.373	0.868	3.101	0.350	2.667	0.602	9.436	0.637
SDSS J152638.18+034353.8	15.519	0.392	11.057	0.889	4.204	0.312	15.399	0.526
SDSS J152630.18+035110.8	19.898	0.572	4.453	0.302	3.076	0.714	3.985	0.496
SDSS J152559.83+035249.3	20.449	0.532	4.829	0.797	5.675	0.752	9.570	0.621

SDSS J152606.03+034530.7	35.265	0.543	7.967	0.756	6.467	0.423	30.293	0.382
SDSS J154933.50-004255.0	41.048	0.520	14.786	0.298	15.507	0.623	51.020	0.464
SDSS J154931.48-003406.1	47.081	0.603	21.924	0.586	28.443	0.380	107.142	0.363
SDSS J154925.24-003717.8	31.185	0.554	9.272	0.354	5.563	0.515	13.066	0.364
SDSS J154914.49-004010.2	18.739	0.289	6.962	0.265	2.092	0.161	7.899	0.371
SDSS J154925.12-003645.4	5.713	0.490	1.992	0.215	1.027	0.204	1.175	0.261
SDSS J222013.98-074355.8	23.491	0.882	8.421	0.842	1.429	0.741	11.733	0.721
SDSS J222005.35-073932.3	8.704	0.701	3.448	0.177	8.773	0.296	28.329	0.338
SDSS J222014.86-073333.7	14.012	0.533	1.404	0.490	3.276	0.329	4.501	0.310
SDSS J221934.90-073825.9	4.006	0.351	-1.761	0.230	1.512	0.161	1.180	0.195
SDSS J221941.85-074703.8	1.784	0.502	0.885	0.268	0.458	0.338	1.091	0.317
SDSS J221936.38-074730.4	30.622	0.558	7.560	0.631	6.075	0.531	14.039	0.189

Table 4.2: Measurements obtained for the equivalent widths of Hβ, [OII]λ3727 and [OIII]$\lambda\lambda 4959, 5007$ lines and error associated as obtained by the Monte Carlo simulations.

4.2 Metallicity estimators

The equivalent widths obtained can be finally used to compute the R_{23} parameter, or in our case, the EWR_{23} parameter as follows:

$$\text{EW } R_{23} = \frac{\text{EW } [\text{OII}]\lambda 3727 + \text{EW } [\text{OIII}]\lambda 4959 + \text{EW } [\text{OIII}]\lambda 5007}{\text{EW H}\beta} \tag{4.3}$$

Furthermore, with the lines available it is possible to compute the O_{32} ratio. This is sensitive to the ionization parameter, and thus it is not a good metallicity calibrator, but it is the best we can use in this case, to choice the correct branch of the R_{23} vs. metallicity calibration. This is obtained as follows:

$$\text{EW } O_{32} = \frac{\text{EW } [\text{OIII}]\lambda 4959 + \text{EW } [\text{OIII}]\lambda 5007}{\text{EW } [\text{OII}]\lambda 3727} \tag{4.4}$$

The values obtained for the R_{23} and O_{32} are summarized in table 4.3.

SDSS name	$\text{Log}(R_{23})$	$\Delta\text{Log}(R_{23})$	$\text{Log}(O_{32})$	$\Delta\text{Log}(O_{32})$
SDSS J003845.31+000006.8	1.972	0.318	0.937	0.019
SDSS J003838.68+000225.1	0.661	0.007	0.015	0.006
SDSS J003806.59+000421.9	1.333	0.047	-0.750	0.014
SDSS J134235.94+014424.1	0.650	0.057	0.479	0.040
SDSS J134229.37+015244.5	0.708	0.005	0.035	0.006
SDSS J134156.84+014241.0	0.729	-4.764	0.406	-2.818
SDSS J145221.51+043448.8	0.497	-0.120	-0.713	0.119

SDSS J145150.75+044111.6	0.354	0.087	-0.116	0.035
SDSS J145147.24+043654.2	0.724	0.023	-0.402	0.050
SDSS J145156.20+043321.7	1.515	0.049	0.370	0.068
SDSS J145147.77+043244.5	1.000	0.148	-0.170	0.072
SDSS J145149.20+043501.6	0.947	0.027	-0.104	0.015
SDSS J152638.18+034353.8	0.502	0.206	0.101	0.057
SDSS J152630.18+035110.8	0.782	0.039	-0.450	0.032
SDSS J152559.83+035249.3	0.869	0.023	-0.128	0.014
SDSS J152606.03+034530.7	0.956	0.031	0.018	0.054
SDSS J154933.50-004255.0	0.862	0.056	0.210	0.028
SDSS J154931.48-003406.1	0.921	0.025	0.459	0.007
SDSS J154925.24-003717.8	0.730	0.006	-0.224	0.005
SDSS J154914.49-004010.2	0.616	0.005	-0.273	0.002
SDSS J154925.12-003645.4	0.599	0.014	-0.414	0.015
SDSS J222013.98-074355.8	0.639	0.014	-0.252	0.018
SDSS J222005.35-073932.3	1.123	0.053	0.630	0.070
SDSS J222014.86-073333.7	1.191	0.034	-0.256	0.034
SDSS J221941.85-074703.8	0.576	0.013	-0.061	0.013
SDSS J221936.38-074730.4	0.827	0.125	-0.183	0.026

Table 4.3: Values obtained for the R_{23} and O_{32} parameters.

These data can be used on a [OIII]/[OII]-R_{23} plane, which is particularly effective to separate the ioniziation parameter and the metallicity as suggested by

McGaugh (1991). In figure 4.4 we can see the R_{23}-O_{32} relation for our sample data.

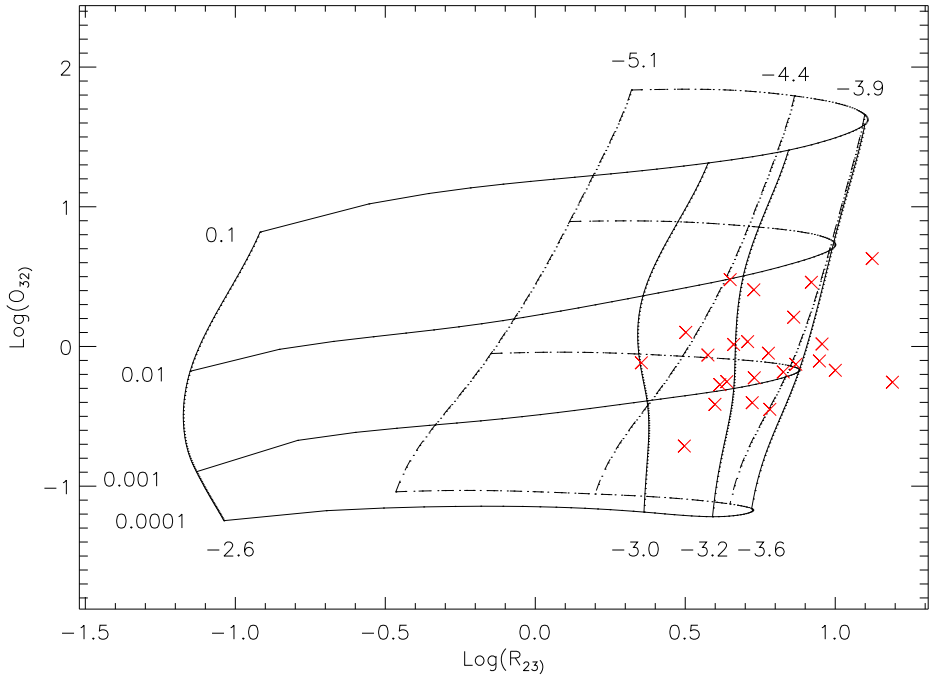

Figure 4.4: R_{23}-O_{32} plot for the sample galaxies. Over plotted there is the model grid obtained by McGaugh (1991). Numeric labels refer to lines of constant ionization parameter (U, horizontal), and constant metallicity ($Log(O/H)$, vertical), being $Log(O/H) = -3.1$ the solar value assumed by McGaugh (1991).

Chapter 5

Results and conclusion

5.1 Correlation analysis

Our purpose is to explore possible correlations between gas metallicity estimator obtained from emission lines and photometric properties in order to obtain a new instrument to study evolution of galaxies from the nearby universe toward higher universe. To this aim we decided to make use of the Sloan Digital Sky Survey, which provides huge amount of data, uniformly computed for a very large number of object.

Having available the coordinates of the objects selected, we identified them in the SDSS archive Data Release 6 (Adelman-McCarthy et al., 2008), and we retrieved magnitudes in the five bandpasses available and colors. Our objects lie in a not so narrow redshift range, spanning from $z > 0.3$ to $z < 0.6$, so it is dangerous to blindly use the observed magnitudes: considering two objects at different redshift, using the same filter to observe them means that we are observing different part of the spectrum simply due to the doppler effect. For this reason we extracted from the archive the absolute magnitudes as well the rest-

frame colors. We combined all these data with the measurements obtained so far for the metallicity estimator R_{23} and O_{32}, plotting all the possible combination of colors, absolute magnitudes and line ratios. We tested all the distributions obtained in order to understand if a correlation exists.

A standard parametric test attempts to reject the hypotesis that the correlation coefficient is equal to zero ($\rho = 0$) by computing r. The significance of a non-zero value for r is tested by computing the t parameter:

$$t = \frac{r\sqrt{N-2}}{\sqrt{1-r^2}} \tag{5.1}$$

which follows the probability distribution of the 'Student's' t statistic, with $N-2$ degrees of freedom.

Critical values of 'Student's' t distribution are used to reject the null hypotesis: if the t computed exceeds that corresponding to a critical value of the probability, then the hypotesis that the variables are unrelated (for example the couples R_{23}-color) can be rejected at the specified level of significance. In other words we can say that the level of significance found is the maximum probability that we accept to risk rejecting the null hypotesis when it is in fact true.

This kind of approach however has some drawback because of the assumption requested. For example it requires that the relation between the data, that must be on continuous scales, must be linear; they must be drawn from normally distributed populations; they must be free from restrictions in variability or groupings.

A viable alternative is to perform a non-parametric test. The most widely used non-parametric test is the Spearman rank correlation coefficient:

$$r_s = 1 - 6\frac{\sum^{N}(X_i - Y_i)^2}{N(N^2 - N)} \tag{5.2}$$

where there are N couples of data ranked so that (X_i, Y_i) represents the ranks of the variables for the ith pair, $1 < X_i < N$, $1 < Y_i < N$. The range of the rank coefficient is $0 < r_s < 1$, with high value indicating a significant correlation. Again, comparing the value obtained for the correlation coefficient to the table of critical values, if r_s exceeds the corresponding critical value, the hypotesis that the variables are unrelated is rejected at that level of significance.

We performed both a classical parametric and a non-parametric test to our distributions. As regards the Log(R_{23})-colors/Magnitudes relations, we obtained values between 0.11 and 0.32 for the Pearson coefficient, and between 0.01 and 0.04 for the Spearman coefficient, while for the Log(O_{32})-colors/Magnitudes relations we obtained values between 0.02 and 0.06 for the Pearson coefficient and between 0 and 0.1 for the Spearman coefficient.
In all these cases, being small the number of measurements (we have 29 objects), these values indicate that no correlation is present between the data, with a significance level greater than 20%.

The absence of correlation is also evident by looking at the plot in figures 5.1, 5.2, 5.3 and 5.4. In these plots we show the possible combination of the metallicity estimator R_{23} and O_{32}, with alternatively the absolute magnitudes and the rest frame colors.

Even if we didn't find any correlation between the photometric data and the two metallicity estimator R_{23} and O_{32} for our sample of galaxies, we decided to further investigate possible connections between gas metallicity diagnostics and

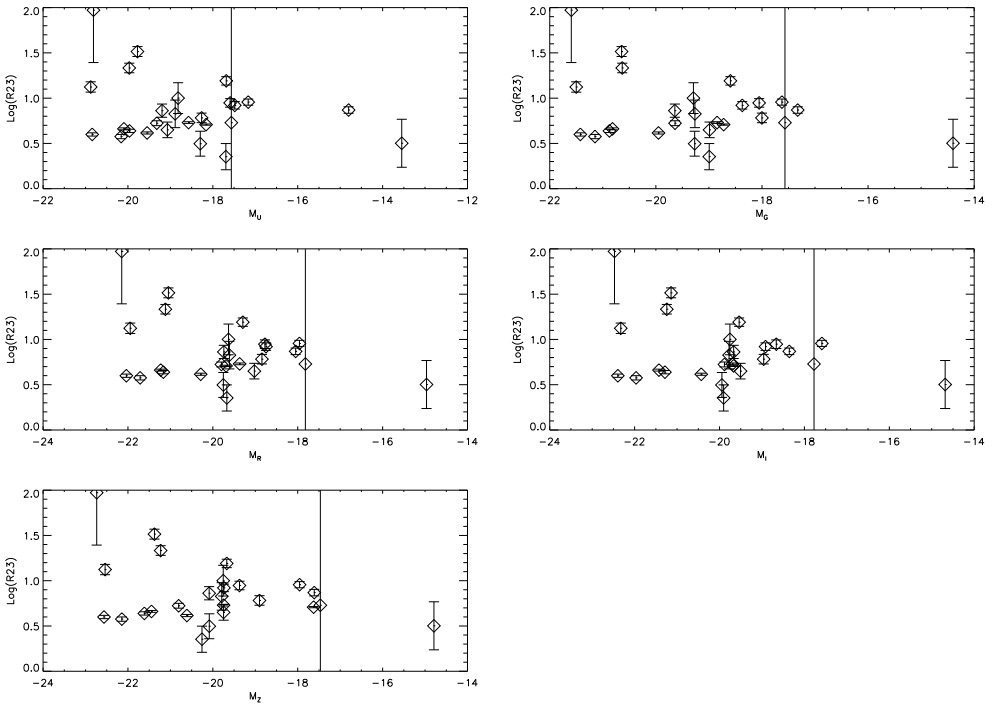

Figure 5.1: Relations between absolute magnitudes in the five different band taken from the Sloan Digital Sky Survey archive and the metallicity estimator R_{23}.

photometry. The aim of our research is in fact to find a proxy for the [NII]/Hα ratio which is, as already said, one of the most used and reliable ratio capable of disentangle the double sided solution in metallicity for the R_{23} parameter.

Failing to provide a measure of the [NII] and Hα for our galaxies, we decided to analyze a sample of galaxies already studied in literature, for which these lines are measured. We used a subsample of the data collected by Nagao et al. (2006), as described in section 3.1.2. The galaxies of this catalog are all present in the SDSS archive, thus we retrieved absolute magnitudes and rest frame colors as done for our galaxies. We tried to correlate the measure of the [NII]/Hα ratio with magnitudes and colors, but as for our galaxies it is clear that no correlation

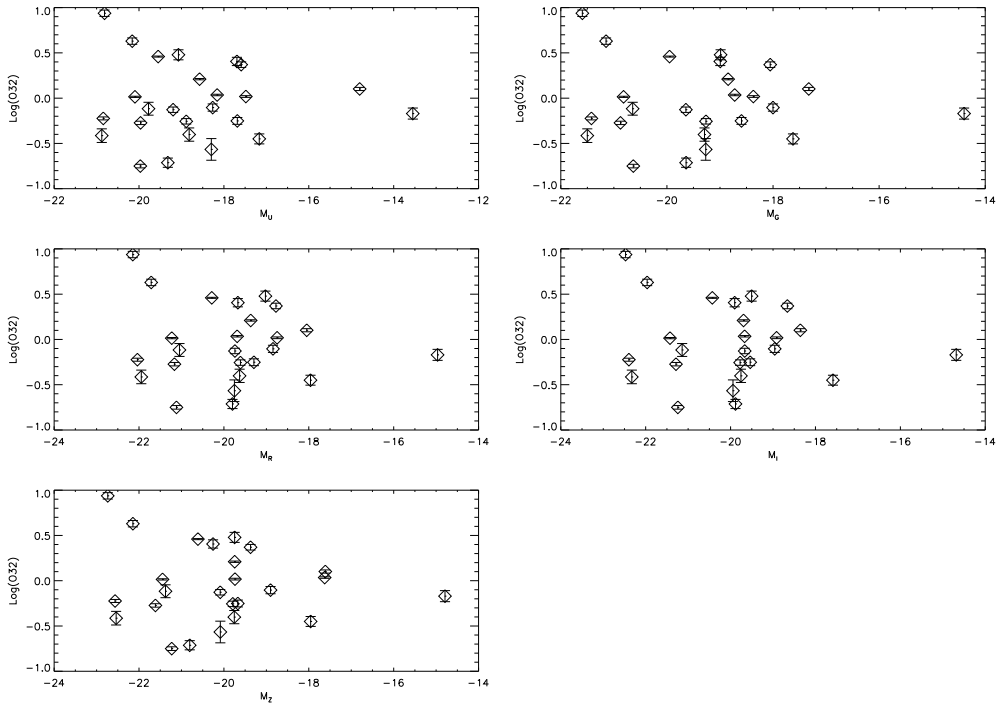

Figure 5.2: Same as figure 5.1 but for the metallicity estimator O_{32}.

exists, as confirmed both by the measure of the correlation coefficients and from the plots (see figure 5.5).

It is clear from the analysis so far performed, that no useful information can be retrieved coupling magnitudes or colors with emission line ratios such as [NII]/Hα or R_{23} and O_{32}, taken alone. A correlation between these parameter seems to be nonexistent, leaving the necessity of very extended spectra covering the spectral regions from the [OII] to (at least) the Hα lines, in order to estimate in the correct way the metallicity. This is very difficult when we want to observe distant and faint objects, for wich we would need very time-consuming observations in order to obtain enough signal and also the complete spectral range.

Having available [OII], [OIII] and Hβ, the only diagnostics that can be used

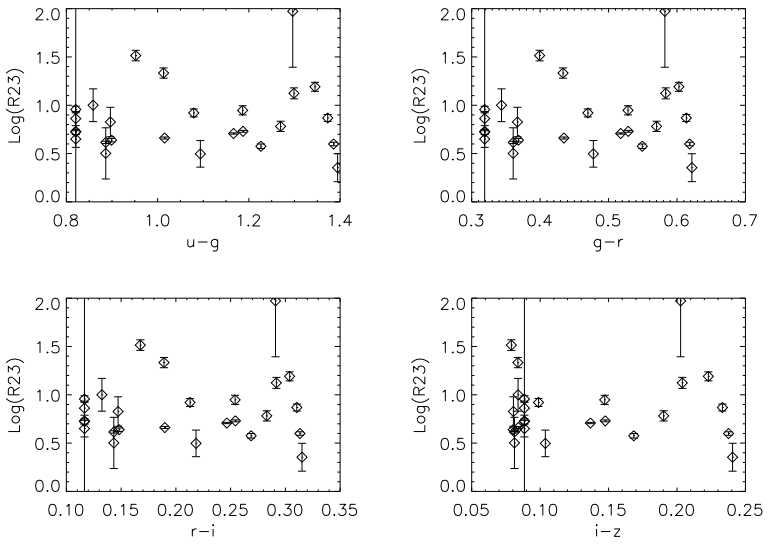

Figure 5.3: Relations between rest-frame colors, as taken from the Sloan Digital Sky Survey archive and R_{23}.

to estimate the oxygen abundance is the R_{23} parameter, which however has the drawback of being double sided, and ineffective especially in the turning region, thus implying a large error for metallicity.

This is the case of our data, which we remember have not been observed with the specific goal of studying the metallicity (and thus not selected a priori), but represent a good example of the vastness of information available in the archives that could be used for different purposes.

Following the prescriptions described by Kewley & Dopita (2002) we used combination of the equations proposed by Zaritsky et al. (1994, Z94), McGaugh (1991, M91) and Kewley & Dopita (2002, K02) themselves to obtain estimates of the metallicity. The Z94 R_{23} method, even if it gives a crude estimate of the metallicity, requires no initial guess so that it could be used as an initial guess for the more accurate M91 an K02 methods to determine the appropriate solution

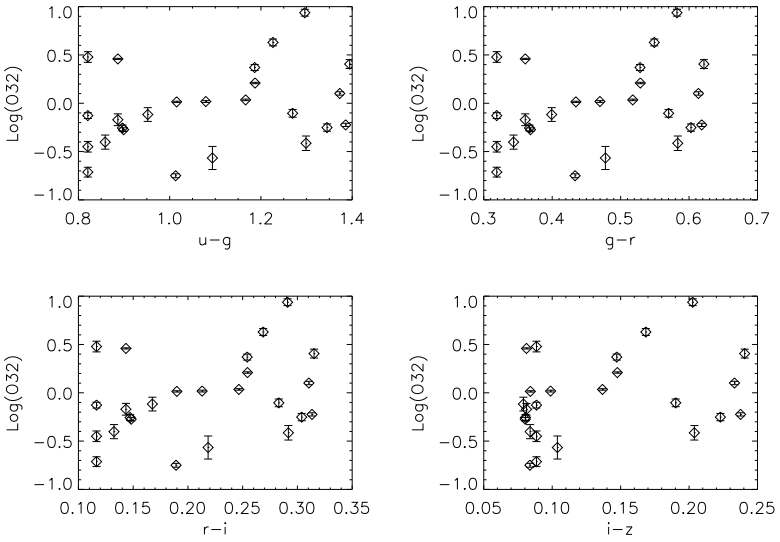

Figure 5.4: Same as figure 5.3 but for the O_{32} parameter.

branch of the R_{23} curve, depending of the value obtained (see Kewley & Dopita, 2002, for further information).

The values obtained for the metallicity (tabulated in table 5.1; the errors, due to the calibration used are ∼0.1 dex) have been used to compare the luminosity-metallicity relation of our sample with previous works.

Although redder bandpasses are less sensitive to the effects of dust obscuration and recent starbursts, historical precedent mandates that the luminosity-metallicity relationship be presented in terms of absolute B magnitude. Fortunately, the SDSS *g* band is fairly similar to the Johnson B band so we adopted the transformation given in Smith et al. (2002) to obtain B magnitudes for our galaxies.

In figure 5.6 we show our results in comparison with the data presented by Lilly et al. (2003). Open circles are the local comparison sample of Jansen et al. (2000) who observed the Nearby Field Galaxy Sample (NFGS, this sample

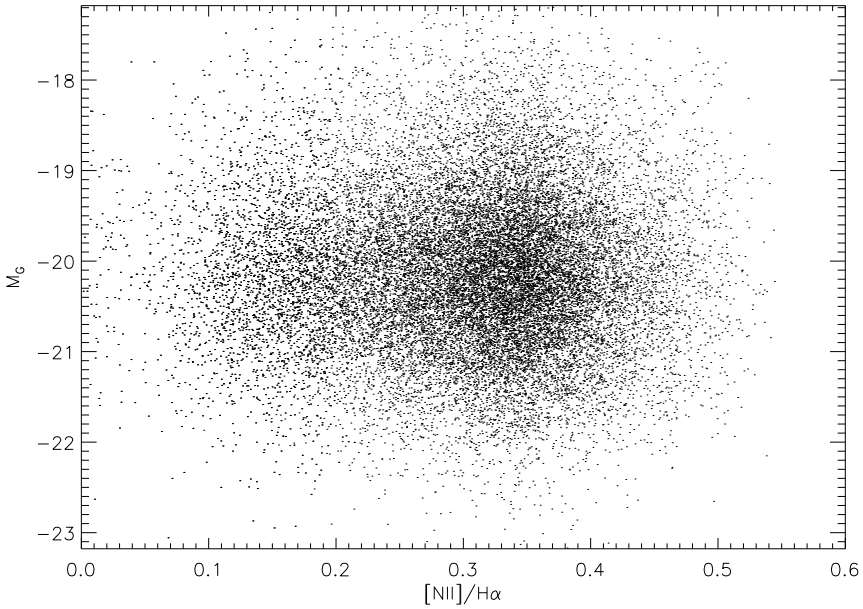

(a)

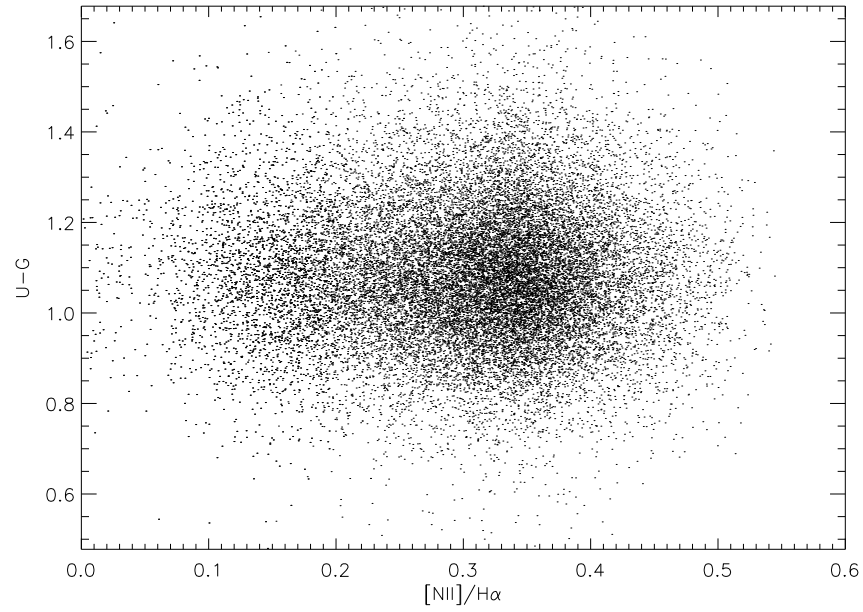

(b)

Figure 5.5: Example of [NII]/Hα ratio vs. Absolute magnitude (a) and rest frame color (b) for the literature comparison sample. No correlation connects these two quantities.

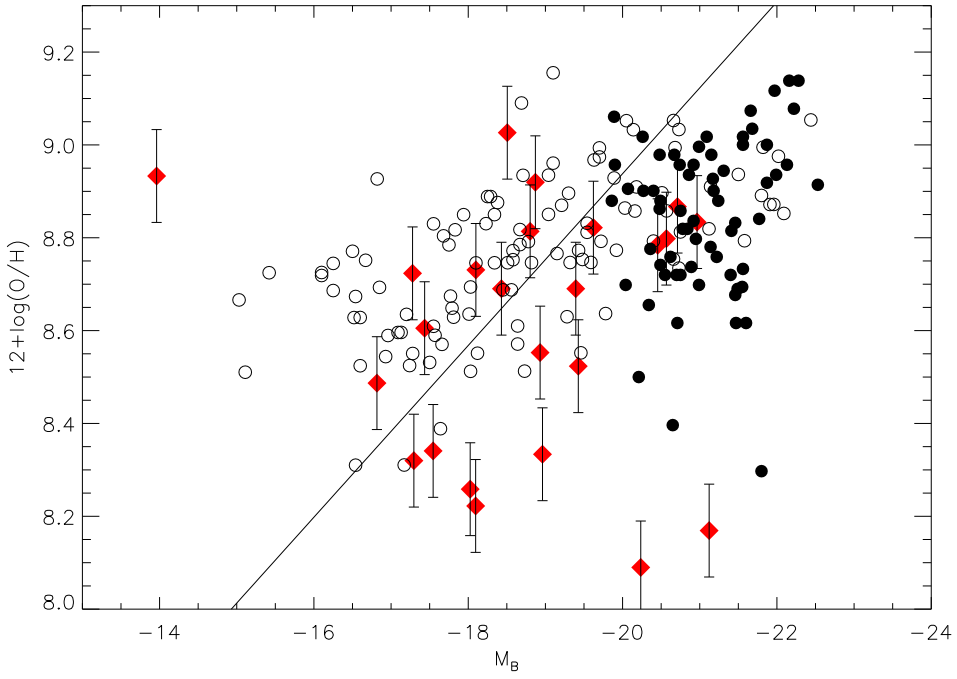

Figure 5.6: Luminosity-metallicity relation for observed sample and other galaxy samples drawn from literature. Red solid diamonds represent our data. Solid circles are the $0.47 < z < 0.92$ CFRS studied by Lilly et al. (2003), while open circles are the NFGS local galaxies used by the authors as comparison sample. The solid line is the luminosity-metallicity relation as obtained by Tremonti et al. (2004) for local SDSS galaxies.

is claimed to include galaxies of all morphological types and span 8 mag in luminosity and a broad range of environments). The solid circles are the $0.47 < z < 0.92$ Canada-France Redshift Survey (CFRS) galaxies studied by Lilly et al. (2003). The solid line represent the luminosity-metallicity relation as fitted by Tremonti et al. (2004) on a large sample of 53000 SDSS local galaxies.

Our data (solid red diamonds), which are in a redshift range similar to that of Lilly et al. (2003) and cover a range of luminosities spanning from -16< M_B <-21, fall in the same region of the comparison galaxies and follow the correlation

proposed by Tremonti et al. (2004) for local galaxies. This result points in the same direction of the conclusions of other authors (e.g. Lilly et al., 2003; Lamareille et al., 2006) that there seems to be no evident evolution in the $L - Z$ relation for low intermediate redshift galaxies.

Galaxy name	12+log(O/H)
SDSS J003845.31+000006.8	8.21900
SDSS J003838.68+000225.1	8.78386
SDSS J003806.59+000421.9	8.08983
SDSS J134235.94+014424.1	8.81380
SDSS J134229.37+015244.5	8.73073
SDSS J134156.84+014241.0	8.72337
SDSS J145221.51+043448.8	8.91959
SDSS J145150.75+044111.6	9.02639
SDSS J145147.24+043654.2	8.69030
SDSS J145156.20+043321.7	8.70841
SDSS J145147.77+043244.5	8.33364
SDSS J145149.20+043501.6	8.34083
SDSS J152638.18+034353.8	8.93302
SDSS J152630.18+035110.8	8.60522
SDSS J152559.83+035249.3	8.48693
SDSS J152606.03+034530.7	8.31987
SDSS J154933.50-004255.0	8.52336
SDSS J154931.48-003406.1	8.25842
SDSS J154925.24-003717.8	8.69030
SDSS J154914.49-004010.2	8.82179
SDSS J154925.12-003645.4	8.83384
SDSS J222013.98-074355.8	8.79814
SDSS J222005.35-073932.3	8.16924
SDSS J222014.86-073333.7	8.22225
SDSS J221941.85-074703.8	8.86708
SDSS J221936.38-074730.4	8.55264

Table 5.1: Measured metallicity for the sample galaxies. The errors, due to the calibration adopted, are 0.1 dex.

Part II

Gas metallicity in nearby Low Surface Brightness galaxies

Chapter 6

Data acquisition and reduction

6.1 Sample selection

The galaxies here studied have been acquired with the primary purpose of studying their kinematics, however the spectral range observed allow us to make an analysis of the metal content through the metallicity estimator [OIII]/Hβ (R_3). The spectroscopic observations have been done in Period 76 (3 night , from 23th to 25th, March 2006) and in Period 80 (two nights, on 17th and 18th, February 2008), at the UT1 unit of the European Southern Observatory Very Large Telescope (ESO program IDs 076.B-0375 and 080.B-0754). The instrument used is the spectrograph FORS2, *FOcal Reducer Spectrograph 2*. FORS2 is an optical instrument capable of operating in imaging, polarimetry, long slit and multi-object spectroscopy modes. We used it in the long-slit mode, equipped with a slit of 0.7" and the grism GRIS_1400V+18 which covers the spectral range between 4560 and 5840 Å with a dispersion of 20.8 Åmm^{-1}. The detector consists in two CCD MIT of 2048 X 4096 pixels each, separated one from the other by 480 μm, with resolution of 0.25"pixel^{-1} (in standard bin-

ning mode 2X2). The measured instrumental dispersion is 0.56Å. This configuration has been chosen in order to obtain measurements of the gas and star kinematics in the region including the Balmer hydrogen line Hβ and the Magnesium MgI$\lambda\lambda$5167.32, 5172.70, 5183.60 lines. Each galaxy has been also observed in imaging mode, with the R-Special+76 filter (centered at λ = 6550Å, with FWHM= 1650Å), in order to verify the correctness of the pointing of the telescope as well as the position angle of the slit. During the first run of observation, each galaxy has been observed by placing the slit along the major axis direction. Three spectra have been obtained slightly drifting the position along the radial direction so that the gap between the two ccd could be in different position. This is done in order to avoid, once the spectra are summed, regions of no signal. The exposure time for each spectrum is 2400 sec., for a total exposure time of 2 hours for each galaxy.

6.2 Data reduction

The reduction of the spectra has been performed using *IRAF* procedures, developed to optimize an speed up all the steps necessary to obtain scientific data starting from the raw observations.

The first step consists in the correction for bias, flat field and the removal of cosmic rays. Then we calibrate the spectra in wavelength units and correct for geometric distorsions. After these steps we can sum together the three spectra observed for each galaxy and we can calibrate the flux. At the end we can move to the analysis of the reduced spectra.

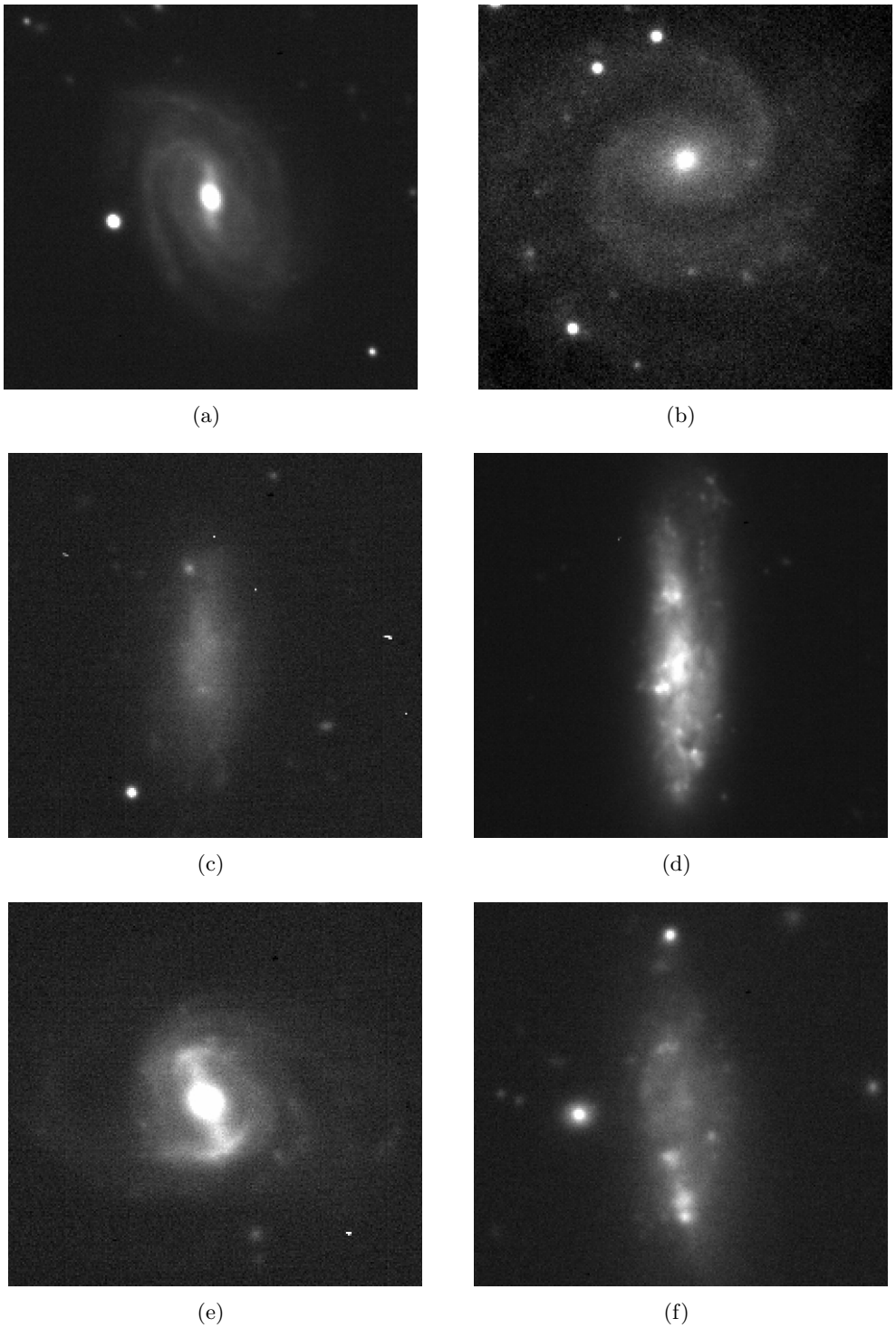

(a) (b) (c) (d) (e) (f)

Figure 6.1: Acquisition images obtained for the LSB galaxies of the sample, as observed in the R-Special+76 filter. The field of view is around 56". (a) 1007+0121, (b) ESO-LV 2060140, (c) LSBC L1-134, (d) NGC 5733, (e) PGC 26148, (f) PGC 33959.

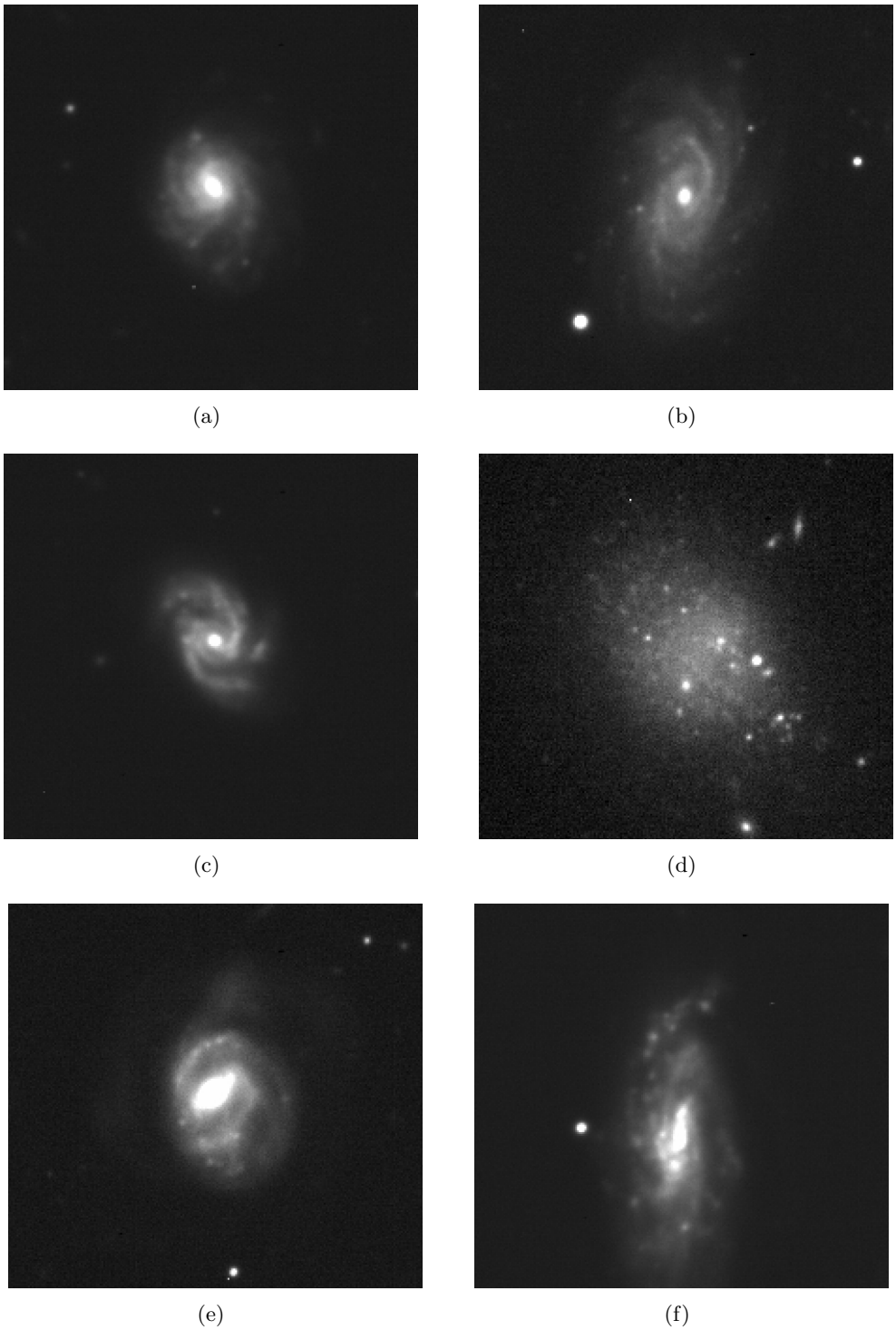

(a) (b) (c) (d) (e) (f)

Figure 6.2: As in figure 6.1. (a) PGC 34605 (b) PGC 37759, (c) PGC 39275, (d) PGC 41395, (e) PGC 46798, (f) UGC 6469.

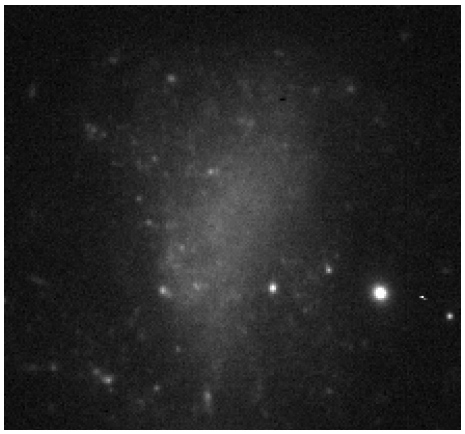

Figure 6.3: As in figure 6.1. UGC 7642

6.2.1 Preliminary reduction

Bias removal

The *bias* correspond to a certain number of counts, not related to any real signal, automatically added from the electronic of the instrument, to avoid that the statistical fluctuation of the counts themselves can reach negative values. Ideally the bias is constant over the sensor, however there is a little dependence from the temperature and the sensor itself: to measure it an image with shutter closed and zero exposure time is used. The hypotesis si that in this way the counts measured are due only to the electronic.

Several bias images have been acquired during every night of observations to better determine the mean value of the correction. All the bias images are averaged together and subjected to a $\sigma-$clipping procedure: the gain and read-out-noise values are combined to determine the σ of the various pixels. Once averaged the images, counts values greater than 3σ will be automatically rejected and replaced with the mean value. In this way we can exclude the contribution from pixels damaged or hit by cosmic rays. The mean bias calculated is around

170 counts, with a standard deviation of 1.5.

Flat field correction

Dishomogeneities over the surface of the detector, generated during the construction of the sensor, cause different quantum efficiency of the pixels: some pixels will be more sensitive, other will be less sensitive respect to a mean value. The analysis of the spectrum (in our case, since we are using spectra) of an homogenous light source can be used to correct for this effect.

During each night, several flat field spectra have been acquired, and they have been processed in the same way of the bias images, i.e. averaged and $\sigma-$clip processed, obtaining the mean flat field FF_m (fig. 6.4), which will be bias-corrected as all the other spectra.

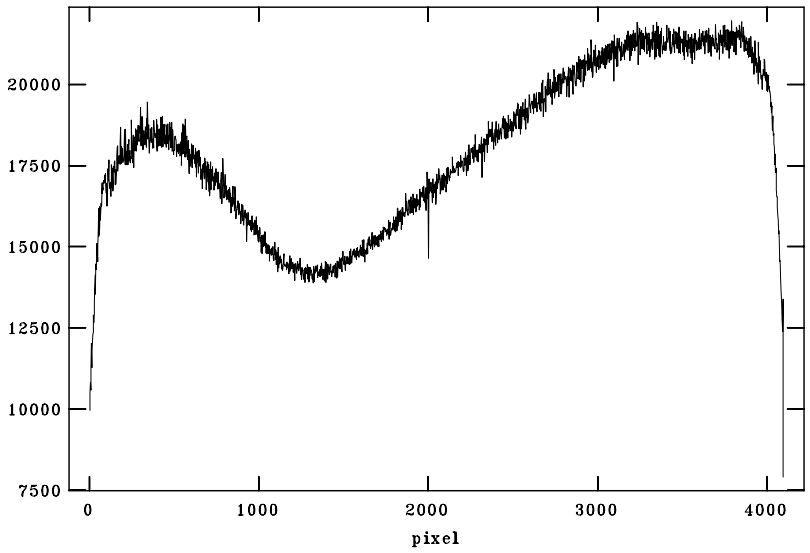

Figure 6.4: Mean flat field extracted along the dispersion axis.

The dependence from the spatial coordinate is corrected creating a normalization flat field. The mean value of the pixels along the dispersion direction is calculated

to form a one-dimensional spectrum. A polynomial filter is applied to remove the small scale fluctuations. Dividing line by line the FF_m by the one-dimensional spectrum obtained, we obtain the masterflat (fig. 6.5) which will be used to correct all the spectra. Counts coming from pixels more sensitive to the mean will be lowered, viceversa for that coming from less sensitive pixels.

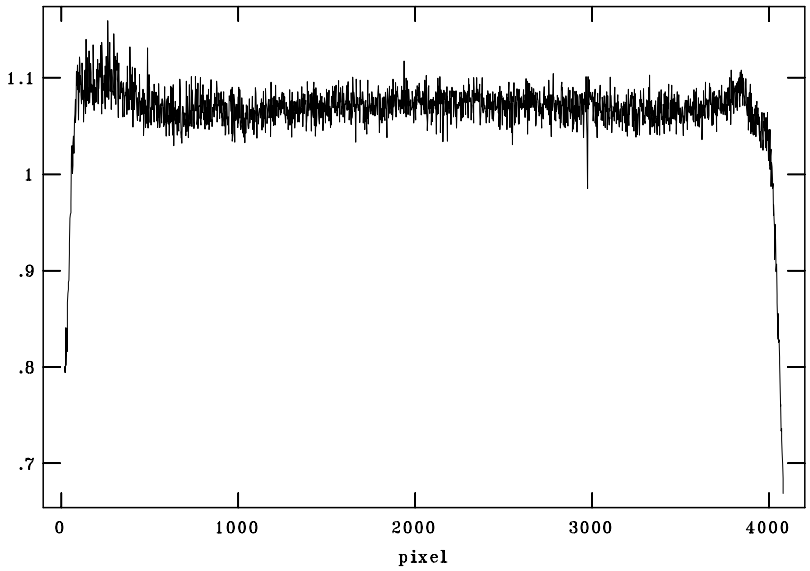

Figure 6.5: Masterflat profile extracted along the dispersion axis.

Cosmic rays removal

When a CCD observation is done, the signal collected by the sensor correspond to all the luminous sources within the field of view of the instrument. Besides the target selected, the near objects and the sky background (with its remarkable luminosity), there are the high energy particles known as cosmic rays. Their spurious signal is removed using the procedure `Lacos Spec` described by van Dokkum (2001). The operation of the program is based on the convolution of the spectrum with the Laplacian of a two-dimensional gaussian function. To

identify the cosmic rays in the convolved spectrum the value of each pixel is compared with the expected noise in the same point. This noise is different from the original one, in fact the laplacian operator increases the latter and "reset" all the negative poissonian fluctuations. The laplacian spectrum is divided by the noise model, calculated from gain and read-out-noise, to determine the deviations from a poissonian distribution.

Cosmic rays are identified when this ratio is above a chosen threshold. They are marked as bad pixels and replaced by the median value of the contiguous pixels. This procedure is iterated several times in order to identify and remove all the cosmic rays.

6.2.2 Wavelength and flux calibration

The spectra processed so far do not yet contain any information about the spectral range: only the physical positions of each pixel on the matrix of the detector is known. The wavelength calibration is intended to assign to the abscissa of each pixel a precise value of wavelength λ, the spectra being oriented so as to have the dispersion axis in the positive direction of the x-axis. To determine which λ associate to the pixels we analyze a calibration spectrum, i.e. the spectrum of a comparison lamp for which the emission lines observed are known.

First, we have to identify the known emission lines on the comparison spectrum. In our case we could identify HeI and HgI lines. We extract a row along the dispersion direction from the comparison spectrum and we identify all the known lines (using the instrument manual as reference image of the line to be identified) to which the correspondent λ is assigned. In this way a raw transformation matrix from physical (x, y) to $\lambda-$calibrated (λ, y) coordinates is created. This transformation is then replicated line by line to the whole spectrum pos-

sibly acting on that rows where the emission lines were not correctly identified. We obtain a new transformation matrix able to correctly assign the wavelengths to each pixel of the spectra.

We also want to remove the geometric distorsion in order to make the dispersion axis really parallel to the chip's axis at all positions along the slits. To calibrate this effect we use a "multi-hole" image, obtained using different exposures of a star at different positions along the slits. Combining the different exposure in a single image, we obtain the equivalent of a calibration spectrum except for the coordinate system that in this case is replaced with the map of physical location of the stars, considering in this case the star as equivalent of the emission lines previously identified. We obtain a second two-dimensional transformation matrix containing the correct physical coordinates for each pixel of the spectra.

The transformation parameters so far obtained from the calibration spectrum and from the multi-hole image, are used to determine the two-dimensional transformation function that will associate each pixel of the spectra to the correct wavelength and capable to map the geometric and dispersion distorsions over the whole spectrum. This function is finally applied to all the spectra.

However this calibration process is not without errors and the emission lines do not coincide exactly with the laboratory wavelengths. This can be easily verified by checking the identified position of the sky-nigth emission lines (that do not suffer Doppler effect). If we compare these lines with the laboratory wavelengths (Osterbrock et al., 1996), we can determine the shift to be applied to the spectra to obtain the correct calibration. The position of the sky lines is measured by taking the center of gaussian profile fitted over each line. The difference between the observed centers and the laboratory measures gives the

shift in wavelength.

Creation of the final spectra

For each galaxy three different spectra have been acquired. This is useful both to reduce the problem of cosmic rays (which would deteriorate too much a long exposed spectrum), and to obtain an higher signal to noise ratio. To combine the several spectra we need the wavelength calibration be exactly the same, furthermore we need to merge each couple of spectra acquired by the two chip of the detector in a single image. FORS2 is indeed composed by two detectors physically separated one from each other by 480 μm, and they have slightly different characteristics, which translates in different levels measured. Of course we have to take into account this difference, when combining the spectra.

To make sure that the wavelength calibration of the different spectra is exactly the same, we resample all the spectra (both chip) with a unique value for the starting wavelength and with the same step in λ. Also the counts number of the CCD 2 are normalized to CCD 1 before merging the two spectra. Further step is to remove the contribution due to the sky background. We extract a row from each spectrum along the direction perpendicular to the dispersion axis and we select one interval on each side of the galaxy, distant from the center (where the contribution of the galaxy is essentially negligible) and not contaminated by other light sources. A function is then interpolated to reproduce the shape of the sky contribution starting from the regions selected and it is after subtracted to the whole spectrum.

At this point we can sum the three spectra. Each mosaic so far created shows a region were there is no signal, due to the physical separation between the two CCD. During the acquisition stage, the center of the galaxies has been

moved along the radial direction in three different positions, so that the separation would fall in different regions respect to the center of the galaxies. The center is evaluated interpolating a gaussian to the profile of the galaxies along the direction perpendicular to the dispersion axis. The radial shift to be applied to each spectrum is then determined and applied in order to have them perfectly overlapping. The spectra are then stacked together, applying meanwhile a $\sigma-$clipping algorithm that removes eventual spurious signals like cosmic rays previously undetected.

Flux calibration

Having observed spectrophotometric standards during the observation run, we are able to calibrate the spectra to real flux units. To make this possible we make uses of the calibrated data for the spectrophotometric standards reviewed. First of all, we correct the airmasses to mid-exposure. We then take the single observation of the spectrophotometric flux standard and compare this to the tabulated calibrated data (Hamuy et al., 1992) for the correspondent star: integrating the data over the appropriate bandpasses and normalizing to the exposure time we obtain a list of the observed counts within each bandpass along with the standard star fluxes. Then we fit the sensitivity function as a function of the wavelength and we apply the result to the spectra, obtaining the calibrated fluxes required (fig. 6.6).

6.2.3 Instrumental dispersion

The procedure used to determine the positions of the emission lines center on the comparison spectra allows us to calculate the instrumental dispersion at the different wavelengths. We average 20 lines in the central region of the comparison

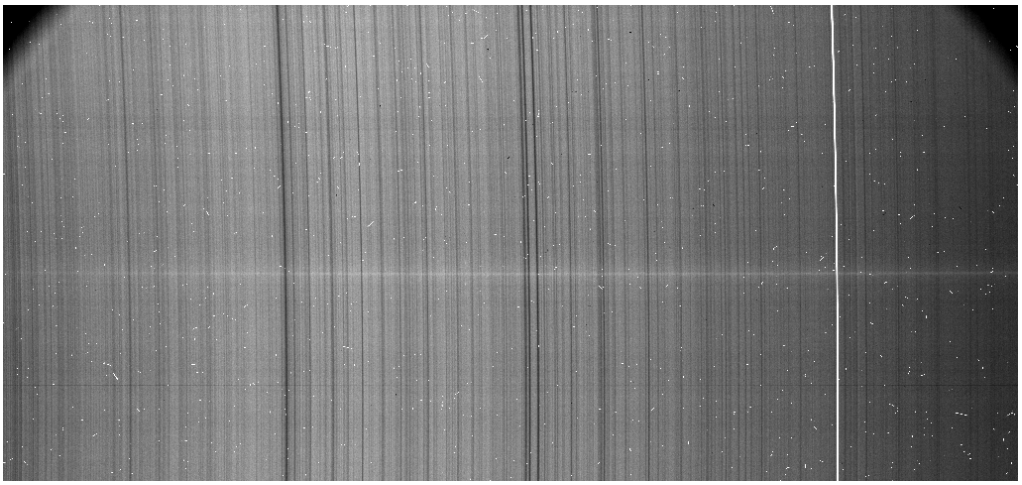

(a)

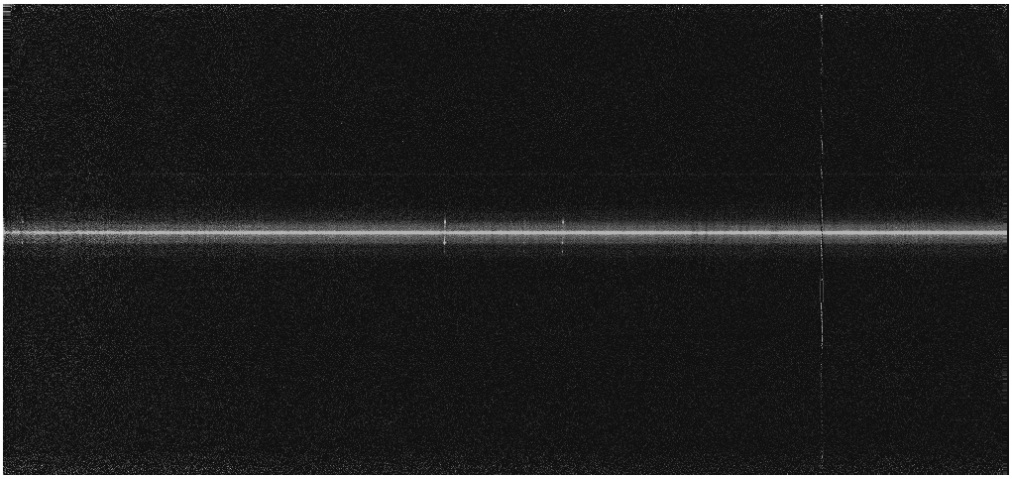

(b)

Figure 6.6: Comparison between the raw spectrum (a) and the final fully calibrated spectrum (b) for the minor axis of the galaxy PGC 37759.

spectrum and we interpolate the gaussian functions to the emission sky lines. We take the position of the center of each line as well as their full width at half maximum (FWHM). Averaging the values obtained for each line we can get the instrumental dispersion value, σ_{instr}.

In our case we obtain $\mathrm{FWHM}_{instr} = 1.33 \pm 0.07$Å, equivalent to $\sigma_{instr} = 0.56 \pm 0.03$Å (fig. 6.7).

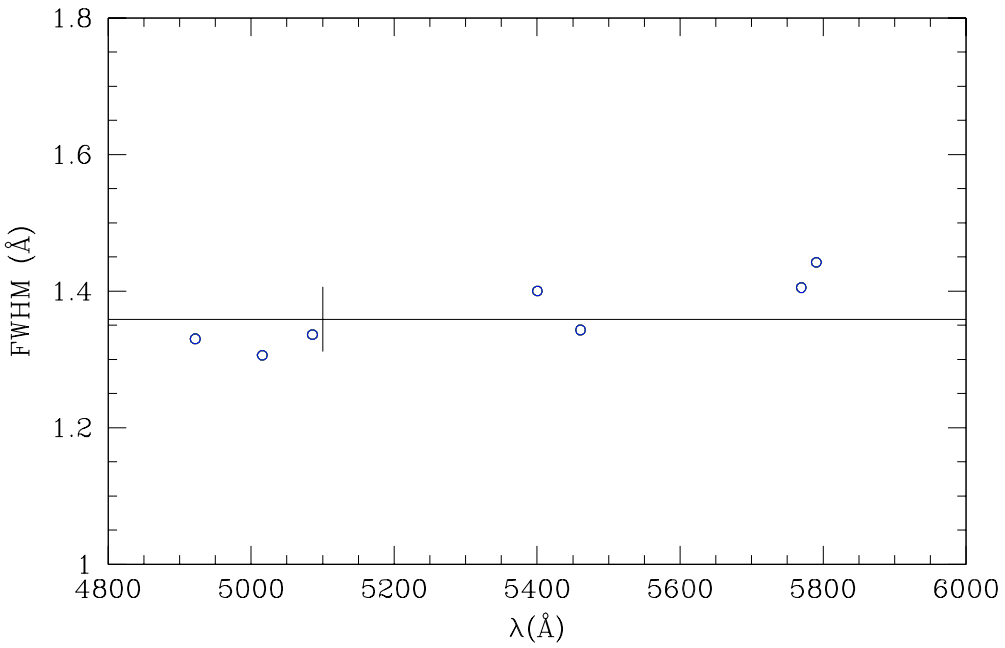

Figure 6.7: FWHM measured for the emission lines of a comparison spectrum, wavelength calibrated. The horizontal line corresponds to the mean value measured for the points, while the vertical bar represents the standard deviation from the mean.

Chapter 7

Data analysis

7.1 Stellar and gas component fit

The usual procedure to obtain measurements of the stellar and gas contribution to the flux incoming from a galaxy is to fit first the stellar continuum alone, masking the spectral regions contaminated by nebular emission, and afterward to measure the emission lines on the residual spectrum of the fit. However, masking the regions affected by gas emission can introduce some spurious features in the residual spectra that can alter the gas measurements, especially for weak emission lines (as described in Sarzi et al., 2006). For this reason we used for the analysis of the spectra the code GANDALF, developed and manteined by M. Sarzi. It is a direct fitting code designed to separate the contribution due to the stellar continuum and to the nebular emission and to measure the gas emission and kinematics. It extends the PPXF software of Cappellari & Emsellem (2004) to obtain a refined procedure to get measurements of the gas kinematics and fluxes without any kind of spectral masking. The code treats the emission lines as additional gaussian templates, iteratively searchs for their best velocities and

dispersions, and solves linearly at each step for their amplitudes and the optimal combination of the stellar templates convolved by the best stellar line-of-sight velocity distribution (LOSVD). The stellar continuum and the emission lines are thus fitted simultaneously.

We used a subset of 50 stars from the stellar library MILES (Sánchez-Blázquez et al., 2006) to build the best model able to reproduce the stellar continuum of our galaxies. In order to compare our galaxies to the stellar library we need first to make their resolution the same. Being our galaxies observed with an instrumental resolution greater than the MILES stars, we convolve the first to the appropriate value of $\sigma = 2.54$Å. This value has been recently recalculated by Beifiori et al. (2010) and it is slightly different from the $\sigma = 2.3$Å proposed in Sánchez-Blázquez et al. (2006).

For each spectrum we summed adjacent rows to obtain a better signal-to-noise ratio. The latter has been evaluated from the difference between the best fitting model and the spectrum. In most cases, the analysis was completed without problem and it returned the sought values of the emission lines fluxes, and also all the kinematics parameters at different distances from the center of the galaxies. In figure 7.1 it is showed an example of the fit performed.

However, in some cases we have encountered problems in the analysis, mainly due to a very bad signal-to-noise ratio, which made impossible to find the correct fit to the spectra, thus forcing us to discard the galaxies affected by these problems.

At the end of this process, we have 8 galaxies. Two of them observed both along the major and the minor axis, two observed along the minor axis, the other observed along the major axis. In table 7.1 there are showed some characteristics of the galaxies observed, being them divided into two groups: the accepted ones

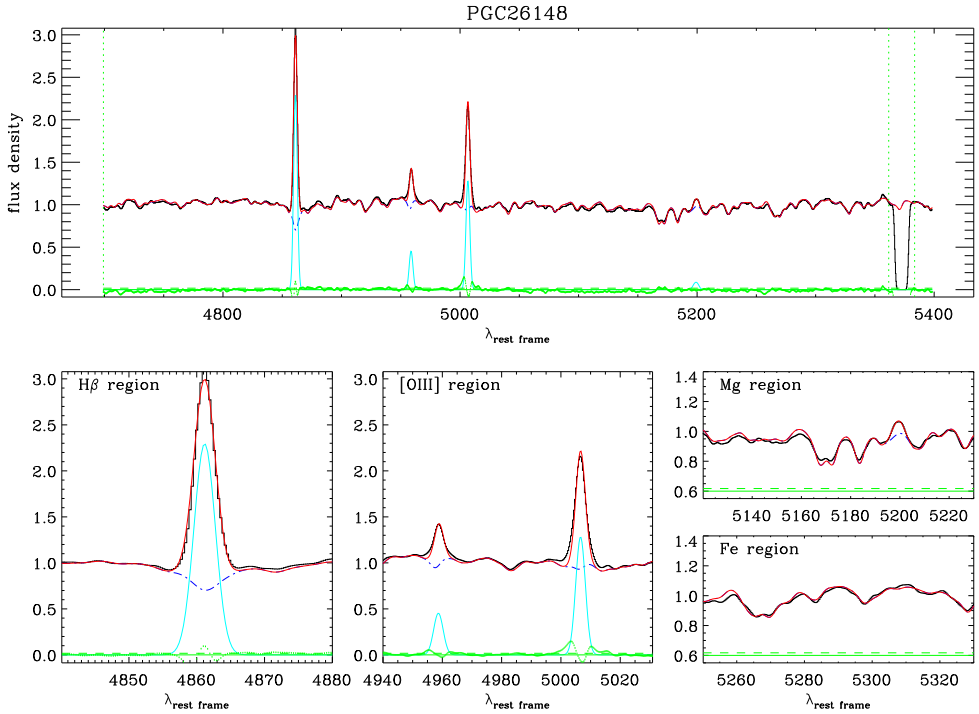

Figure 7.1: Example of the fit obtained. Here it is showed the central row for the galaxy PGC 26148. In the top box there is the entire spectrum (black) where the fit has been performed. Superposed, in red, the result of the fit of both the stellar and gas component. In cyan the emission lines fitted. The blue dash-dotted line represents the only stellar component. The green vertical dashed lines delimit the region where the fit has been performed. The green dotted line (here barely visible) represents the residuals between the fit and the original data. The three bottom boxes are a zoom of the regions interested by the following analysis, i.e. the Hβ, [OIII], magnesium and iron lines.

and the rejected.

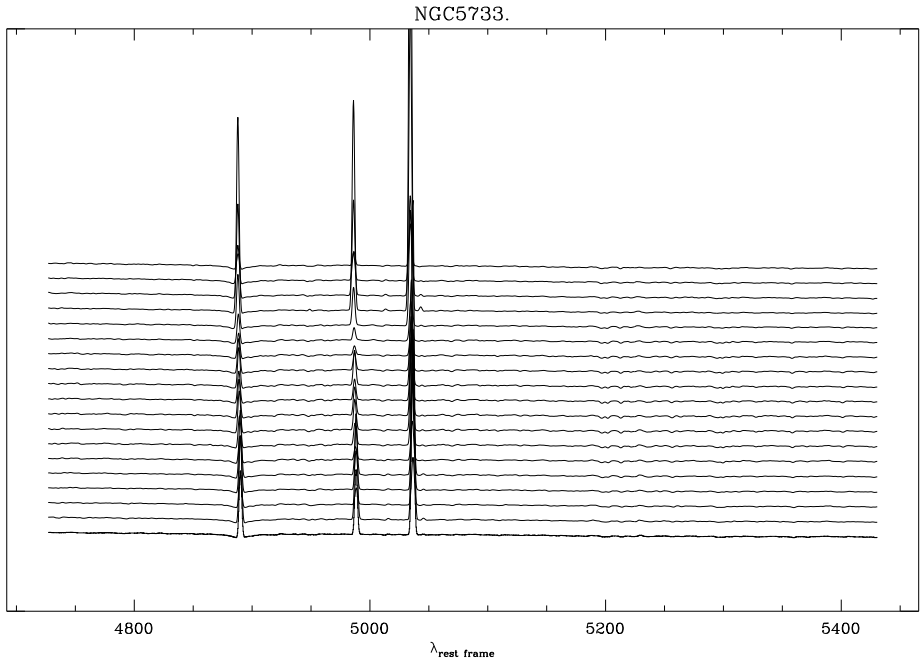

Figure 7.2: Spectra of the galaxies accepted. Each plotted spectrum is the spatially binned rows on which we performed the measure of the line strengths. The central spectrum correspond to the center of the galaxy. The spectra are at rest-frame.

7.2 Metallicity estimators

The analysis performed so far allows us to plot the radial profile of the metallicity estimator [OIII]/Hβ (R_3) for the galaxies selected. These are showed in figure 7.3.

The remarks made earlier about the degeneracy of the R_{23} parameter remain the same also in this case, making the R_3 index alone unsatisfactory to assess the correct value of the gas metallicity. However, for the galaxies here analyzed

Name	Ra	Dec	B_{tot}	μ_0	M_B	Hubble	z	Axis
	(h m s)	(° ' ")	(mag)	(mag/arcsec^2)	(mag)	type		
(1)	(2)	(3)	(4)	(5)	(6)	(7)	(8)	(9)
Accepted								
NGC 5733	14 42 45.90	-00 21 04.9	14.7	20.8	-16.5	dIn	0.006	M
PGC 26148	09 16 13.77	+00 42 02.8	15.5	20.4	-19.8	Sm	0.038	m
PGC 34605	11 18 49.52	+00 37 09.4	15.9	21.5	-18.7	Sa	0.026	M
PGC 37759	11 59 24.59	+01 26 02.2	16.0	21.7	-19.8	Sc	0.047	M+m
PGC 39275	12 16 04.46	+01 10 49.2	16.2	22.1	-19.8	Sa	0.050	M+m
PGC 46798	13 23 40.71	+01 21 42.9	15.9	21.5	-20.3	Sm	0.057	M
UGC 6469	11 28 17.67	+02 39 14.1	14.1	19.9	-20.1	Irr	0.023	M
ESO-LV 2060140	06 28 28.3	-48 45 34.0	14.9	21.7	-19.0	SABc(s)	0.015	m
Rejected								
1007+0121	10 10 29.01	+01 06 58.9	15.9	21.6	-21.6	Sc	0.103	M
LSBC L1-134	10 50 09	+01 15 37.3	17.4	23.1	-13.6	dI	0.005	M
PGC 33959	11 10 55.20	+01 05 37.9	15.9	22.1	-14.1	dIn	0.003	M
PGC 41395	12 31 03.79	+01 40 34.2	15.6	22.5	-14.6	dIn	0.004	M
UGC 7642	12 30 13.79	+02 37 28.2	15.2	22.4	-15.9	dI	0.005	M

Table 7.1: Galaxies sample observed. Data are taken from the catalog of Impey et al. (1996), except for ESO-LV2060140 (ESO-LV). Col. (1): galaxy name; col. (2) & (3): equatorial coordinates; col. (4): total apparent magnitude in B band; col. (5): central surface brightness; col. (6): absolute magnitude in B band obtained assuming $H_0 = 100$ km s^{-1} Mpc^{-1}. Distances are estimated from the heliocentric velocities measured by the 21 cm HI line; col. (7): morphologic type from de Vaucouleurs et al. (1991), and ESO-LV (ESO-LV2061040); col. (8): redshift; col. (9): axis available (M stays for Major, m for minor).

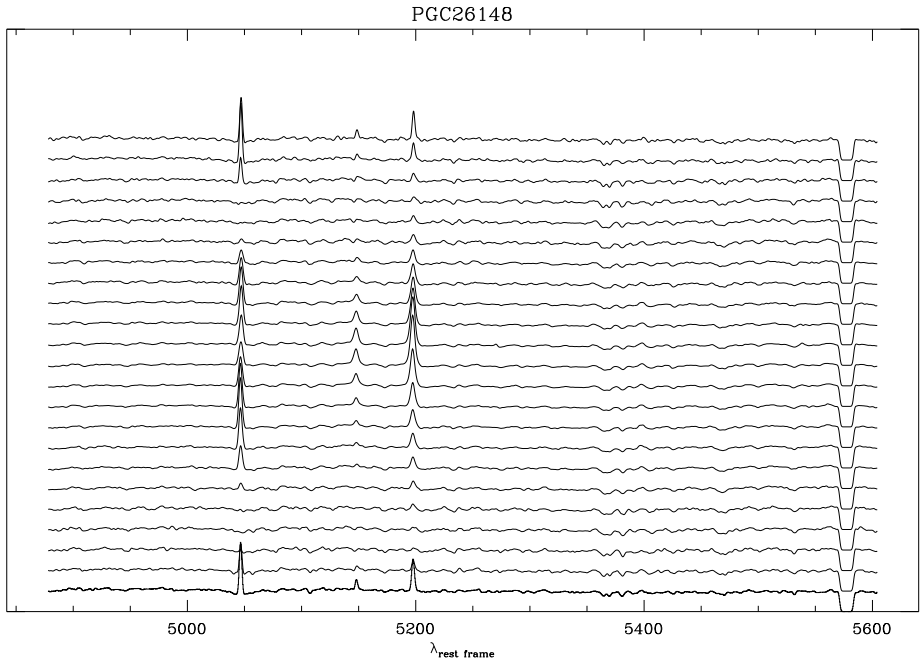

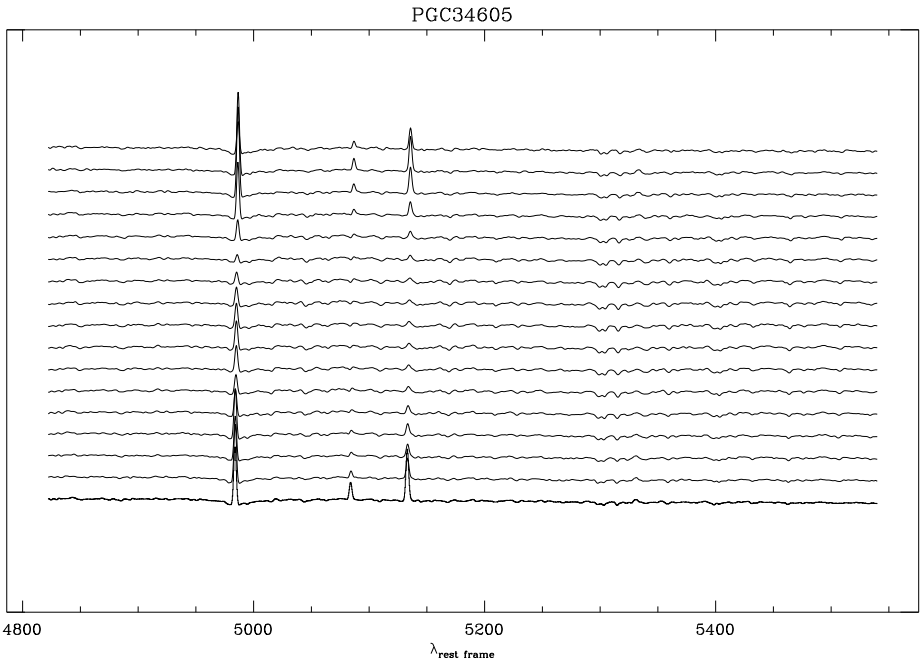

Figure 7.2: Continued

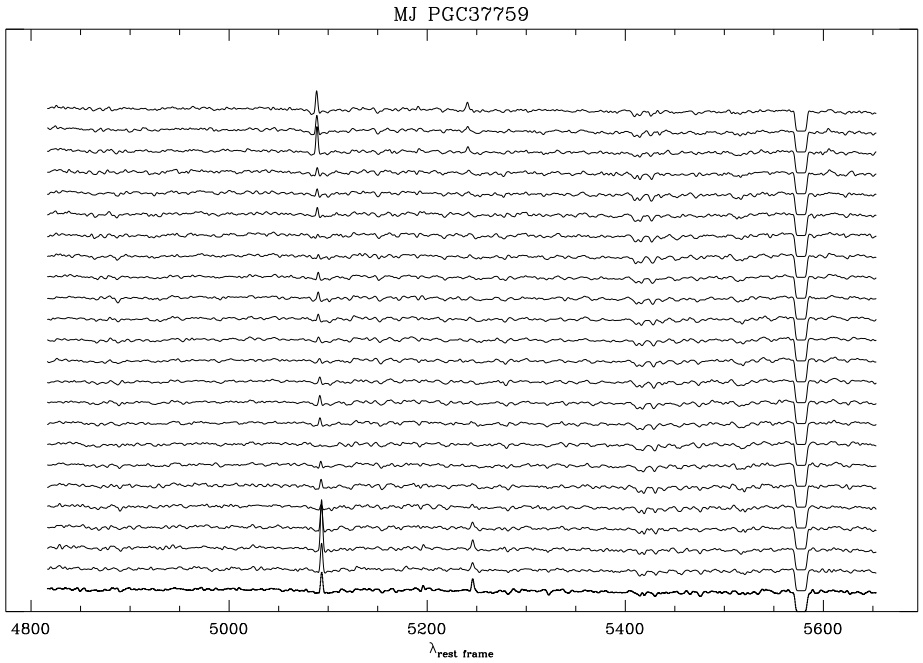

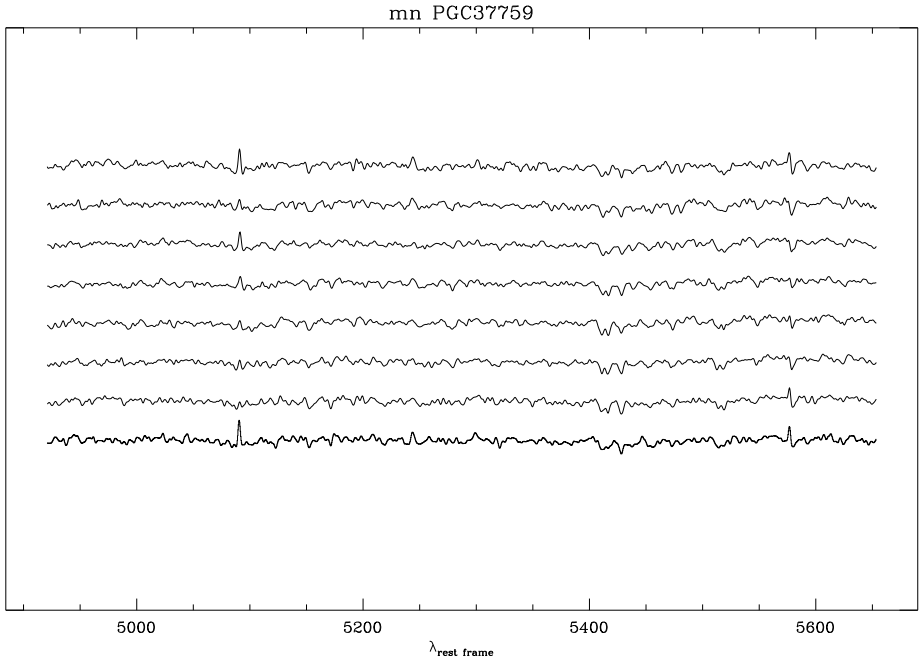

Figure 7.2: Continued

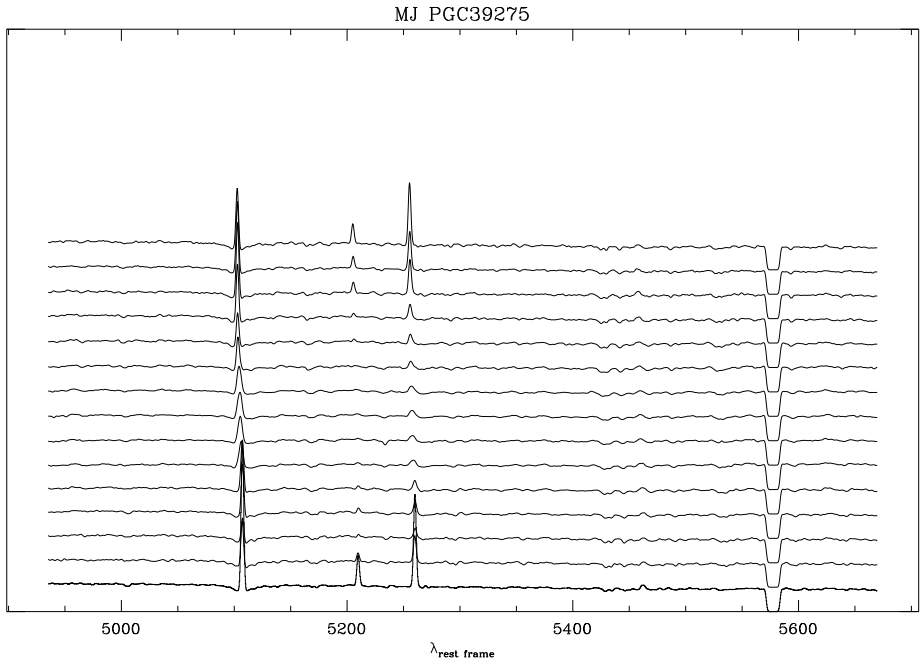

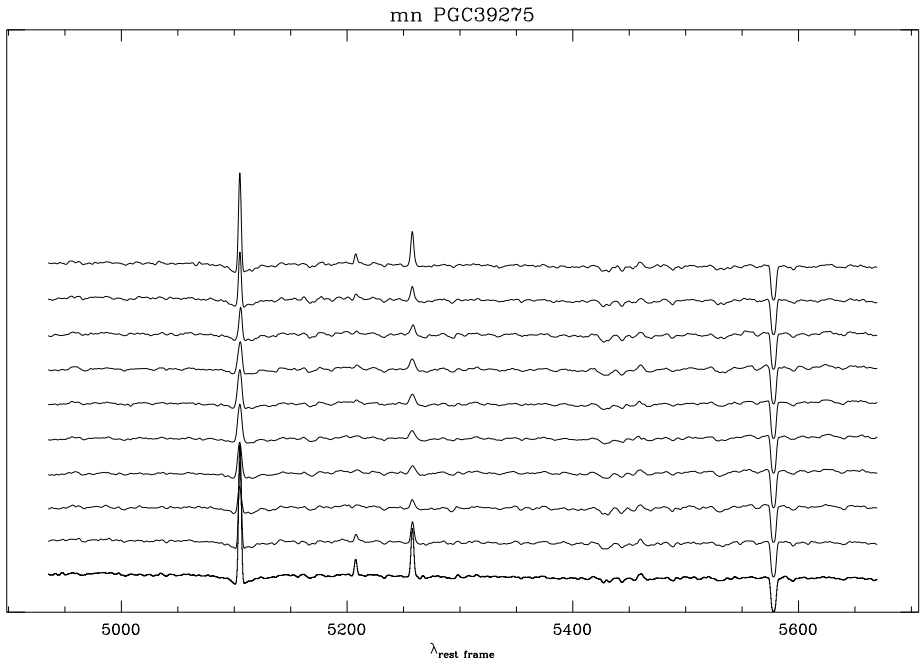

Figure 7.2: Continued

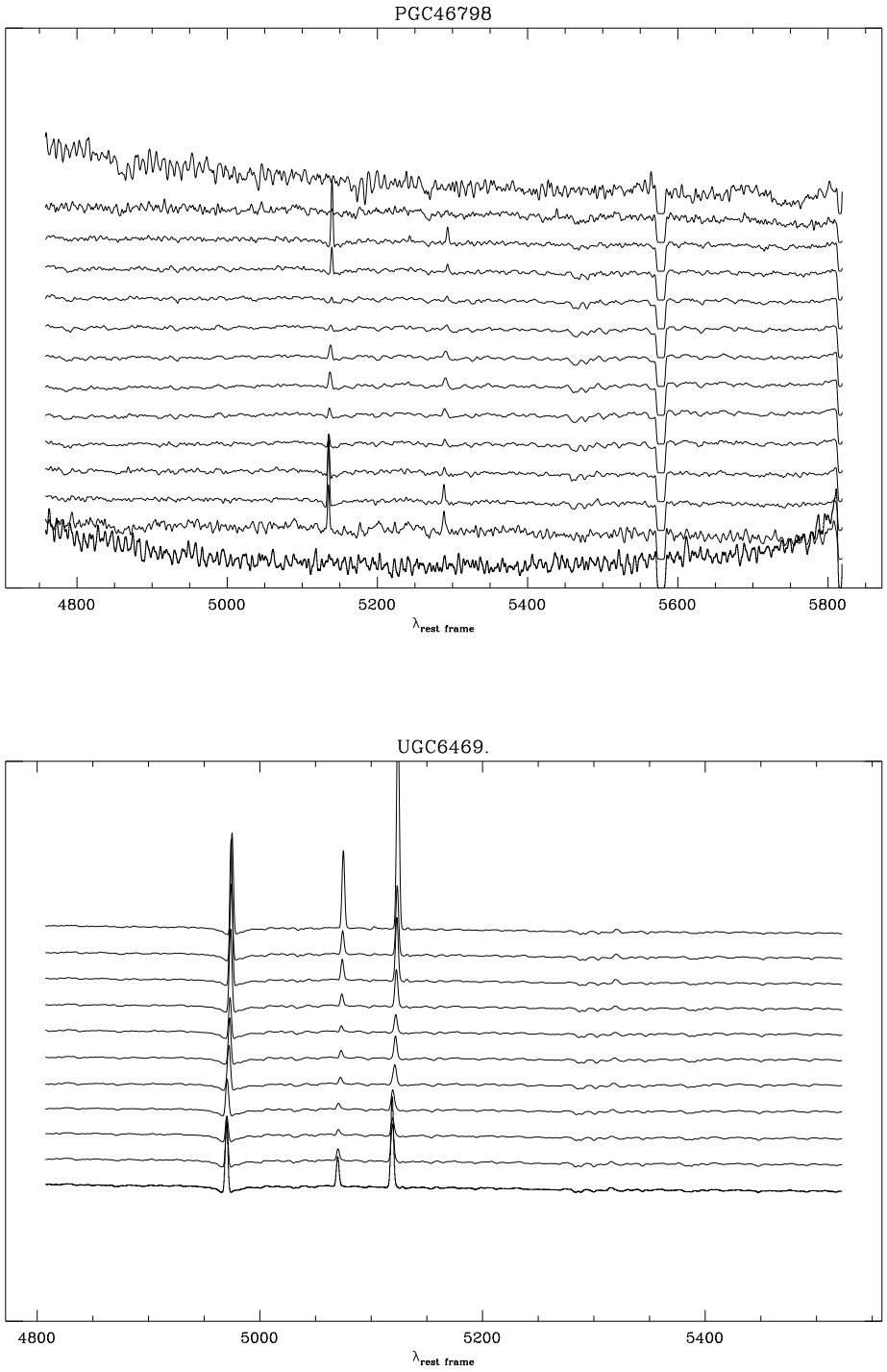

Figure 7.2: Continued

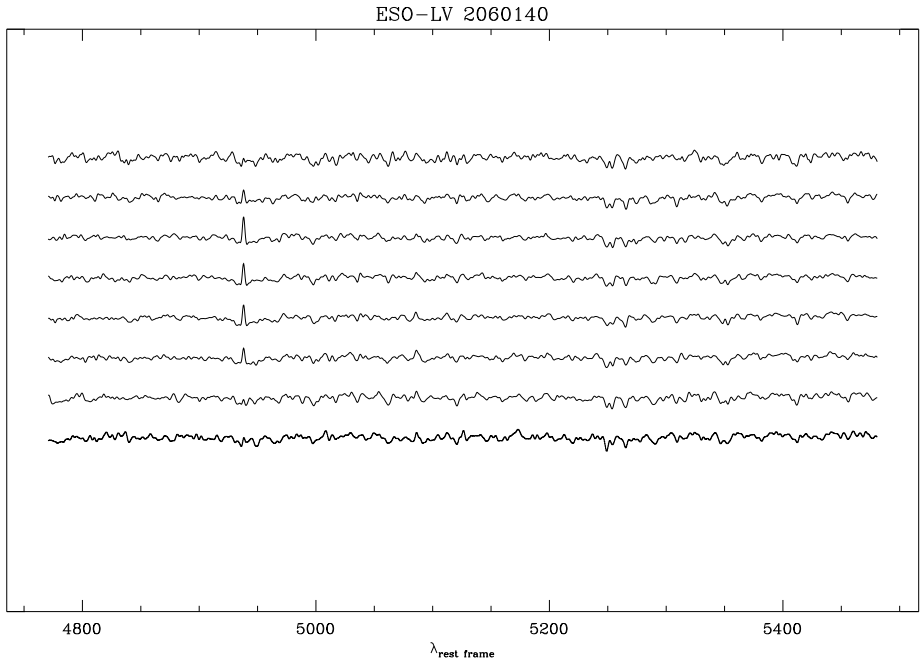

Figure 7.2: Continued

we are able to identify a well defined stellar continuum, and we can use it to obtain a measure of the stellar absorption indices Mgb and $\langle$Fe$\rangle$. In Bergmann et al. (2003) it is showed how these indices are correlated with the gas metallicity indicator [NII]/Hα (see figure 7.4):

$$[\text{NII}]/\text{H}\alpha = -0.11(\pm 0.13) + 0.26(\pm 0.08)\langle\text{Fe}\rangle \tag{7.1}$$

$$[\text{NII}]/\text{H}\alpha = -0.01(\pm 0.09) + 0.16(\pm 0.05)\text{Mg}b \tag{7.2}$$

The [NII]/Hα ratio gives indications about the current metallicity of the gas. The

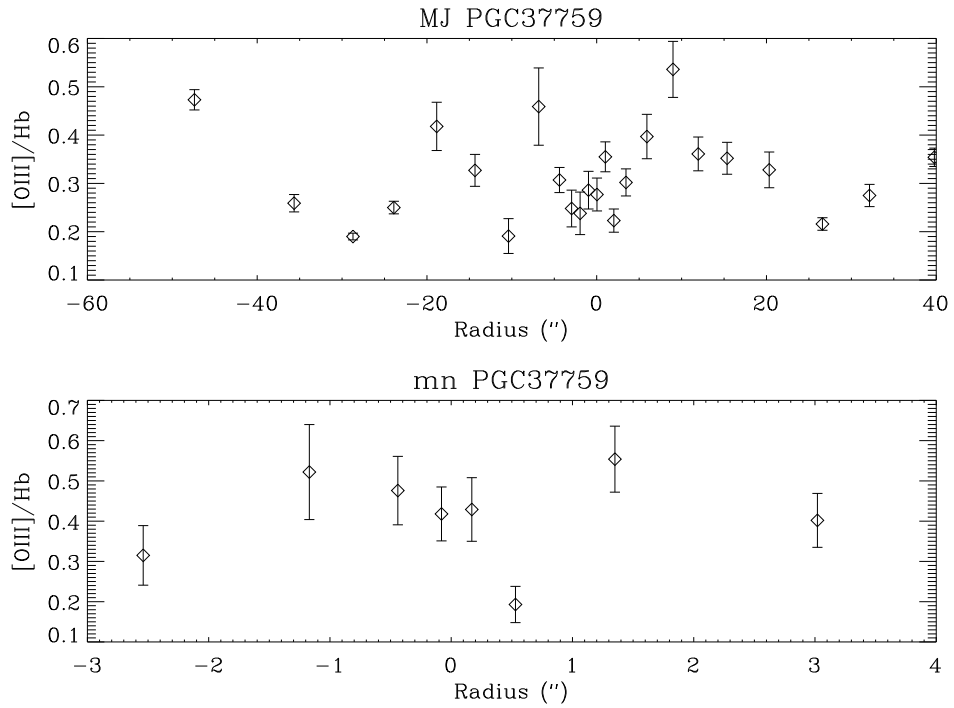

Figure 7.3: Radial profiles of the [OIII]/Hβ ratio obtained for the galaxies accepted. The error bars are the result of the propagation of the errors obtained from the fit.

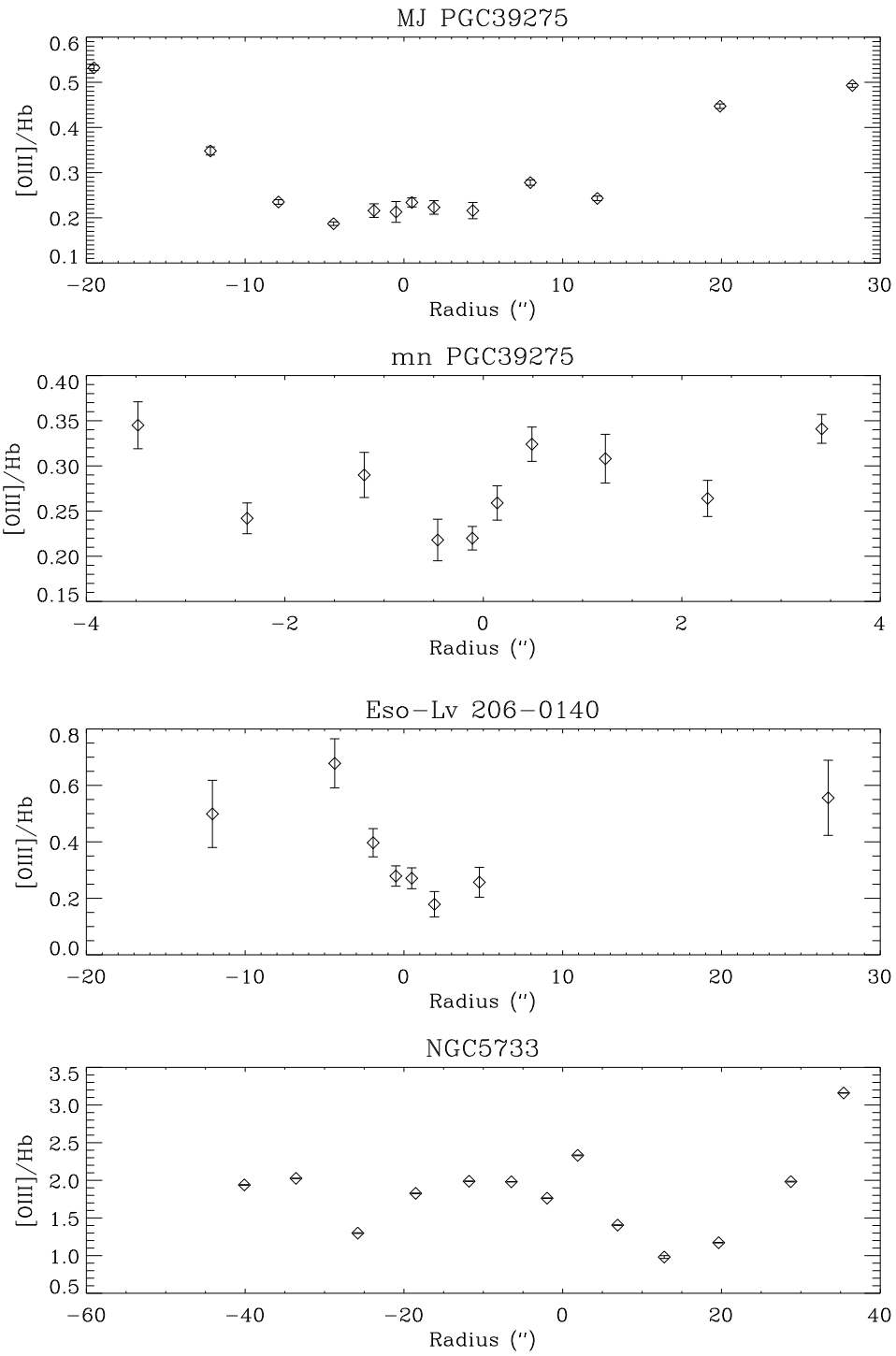

Figure 7.3: Continued

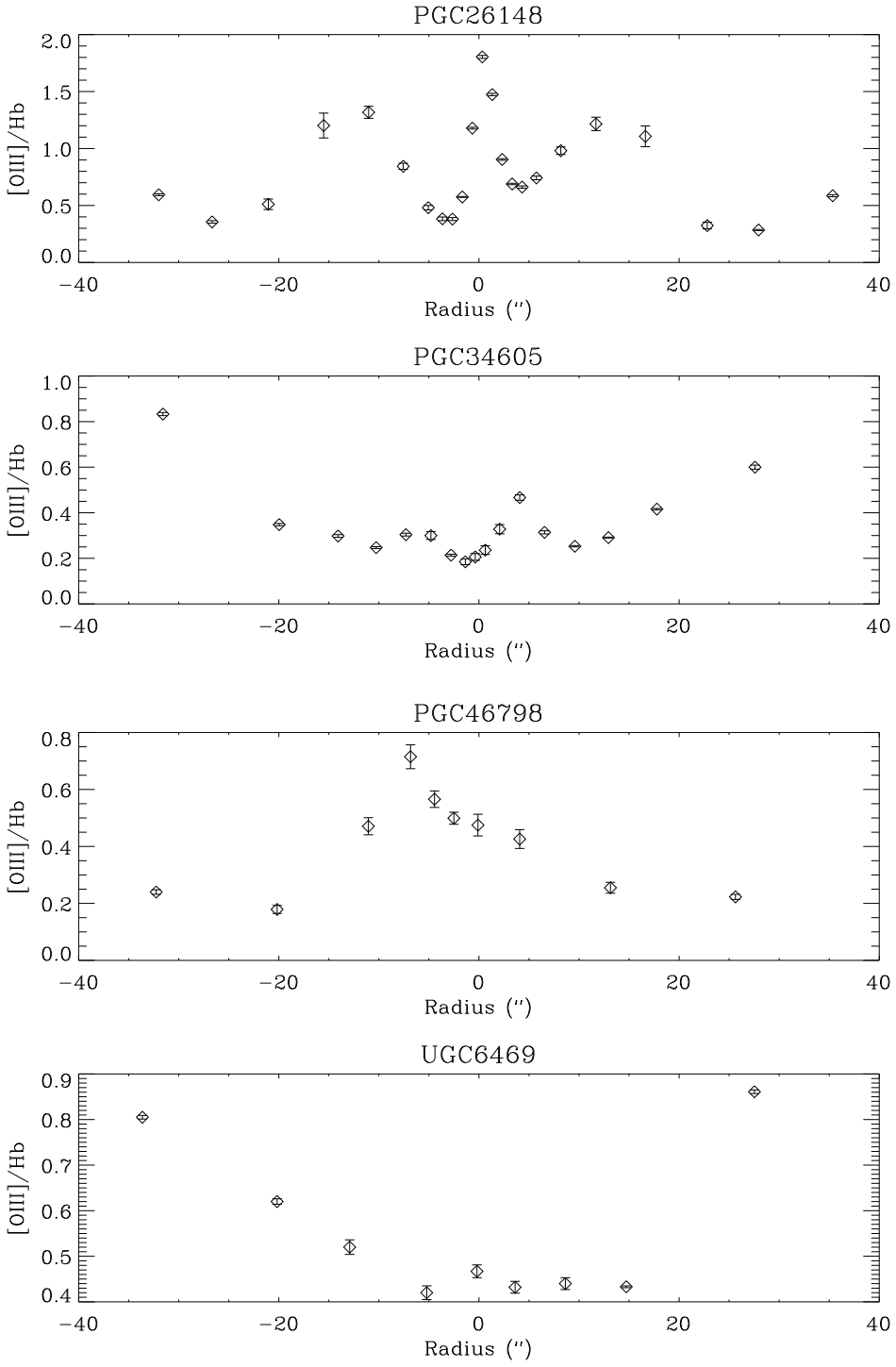

Figure 7.3: Continued

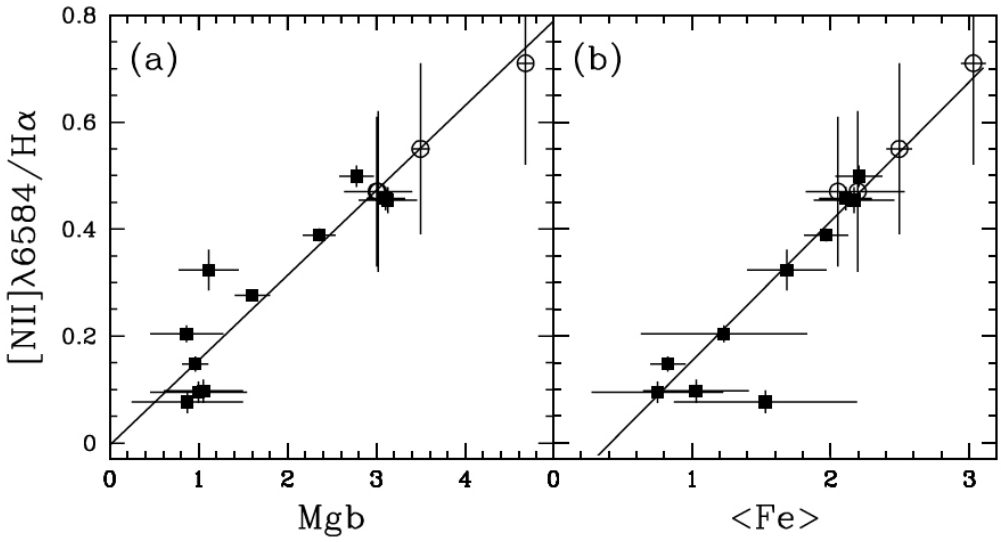

Figure 7.4: Relation between the [NII]/Hα ratio and the Lick indices Mgb and $\langle$Fe$\rangle$ found for LSB galaxies, as showed by Bergmann et al. (2003) (see fig. 9 in the paper).

Mgb and $\langle$Fe$\rangle$ intensities are responsive to both the metallicity and age of the stellar population, but these are linked by the gas consumption and enrichment story. For this reason a correlation does exist between the current metallicity and the age and enrichment history of the stellar population.

We can use this correlation to obtain an estimate of the metal content for our galaxies, and we can move back to the R_3 parameter to establish the correct branch of metallicity solutions.

The stellar absorption indices Mgb, Fe5270 and Fe5335 have been obtained following the definitions of the Lick/IDS system (Worthey et al., 1994), while the average iron index is defined as $\langle \mathrm{Fe} \rangle = (\mathrm{Fe5270} + \mathrm{Fe5335})/2$. Before measuring the indices we matched our spectra to the fixed spectral resolution of the IDS spectrograph ($\simeq 9$Å) convolving our spectra with a gaussian profile of the desired fwhm. The errors on indices were derived from photon statistics and

CCD readout noise, and calibrated with a Monte Carlo technique, reiterating the measure of the indices 100 times. The values obtained from the equations 7.1 and 7.2 are then averaged, and the errors on the measurements propagated (see table A.1 in appendix A).

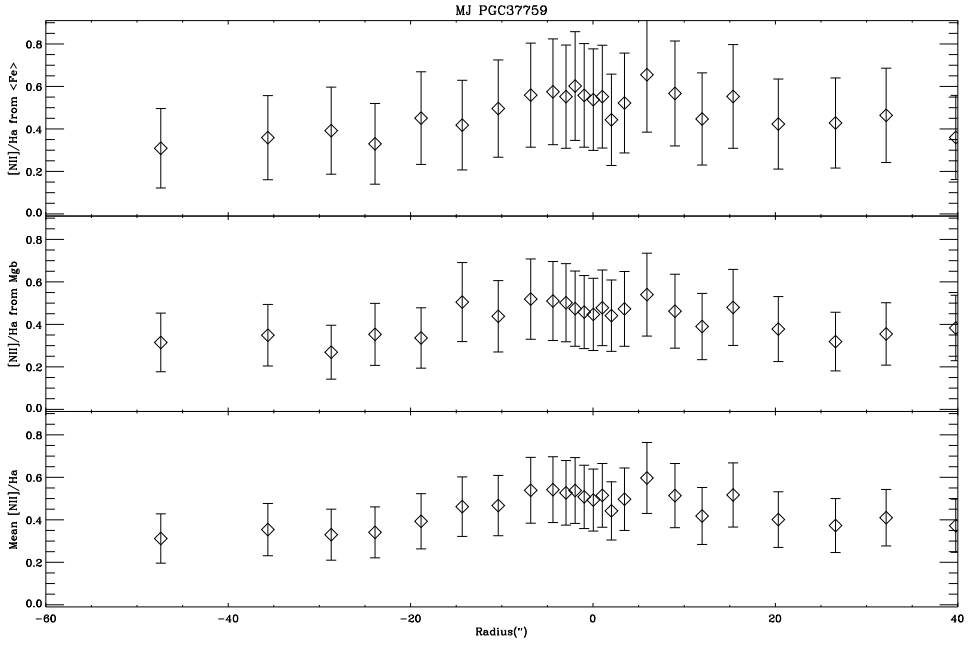

Figure 7.5: Radial distribution of the computed [NII]/Hα ratio. Top box shows the values obtained from the $\langle$Fe$\rangle$ index, as obtained by Bergmann et al. (2003). Middle box shows the values obtained from Mgb. Bottom box shows the mean values. The error bars are the result of the propagation of the uncertainties, and includes also the systematic errors associated to the parameters calculated by Bergmann et al. (2003).

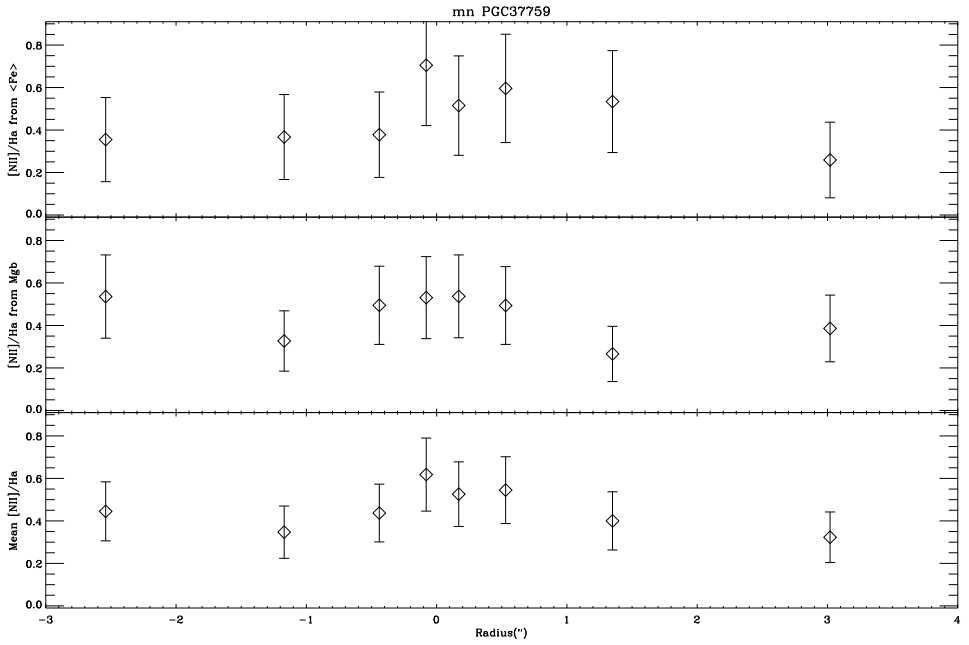

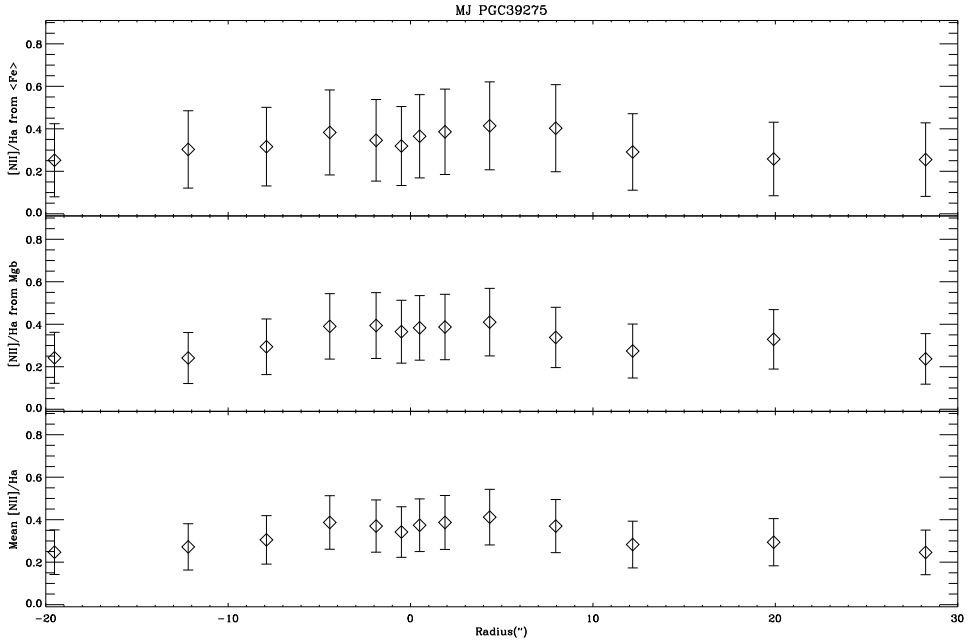

Figure 7.5: Continued

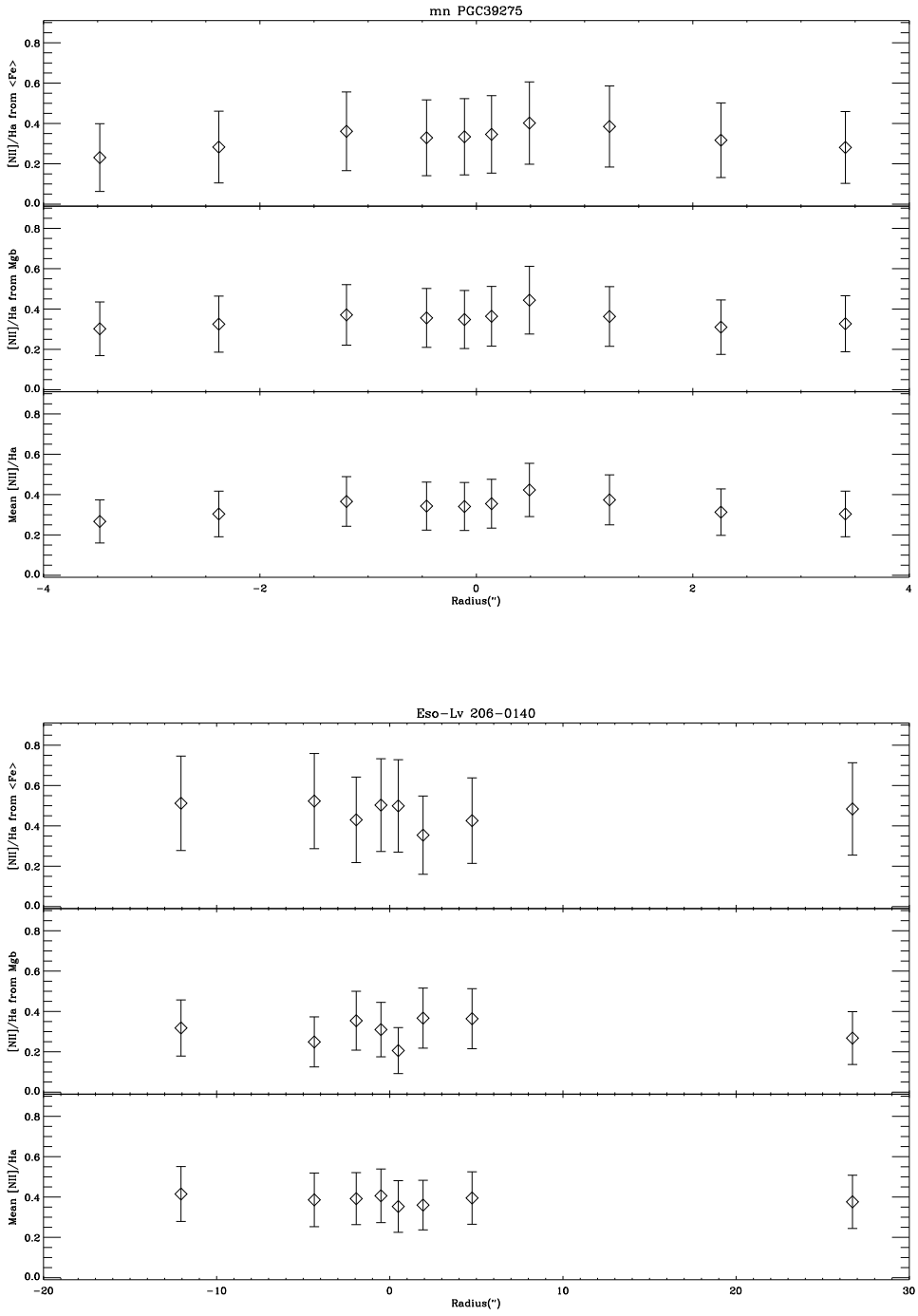

Figure 7.5: Continued

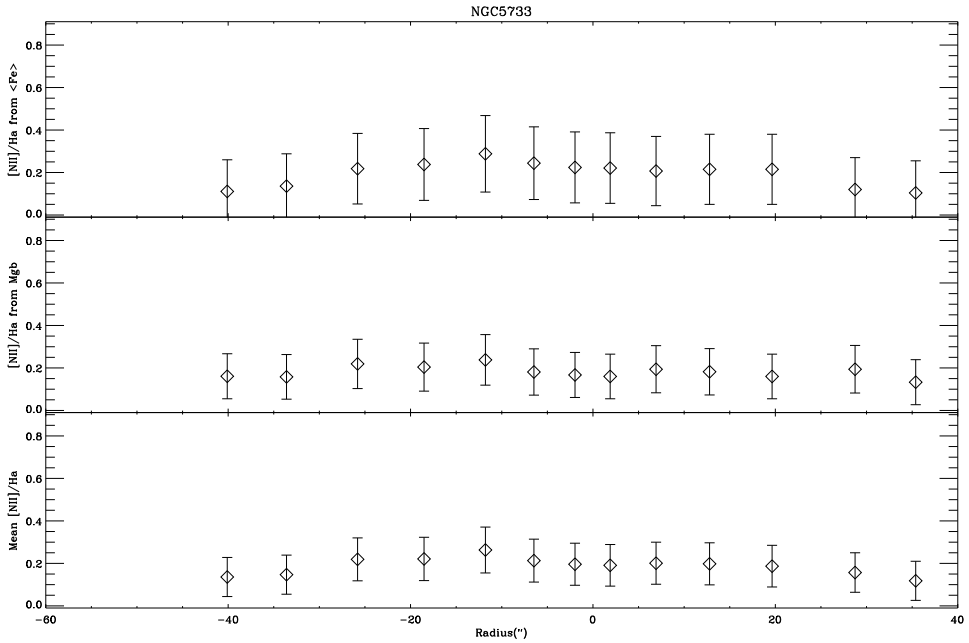

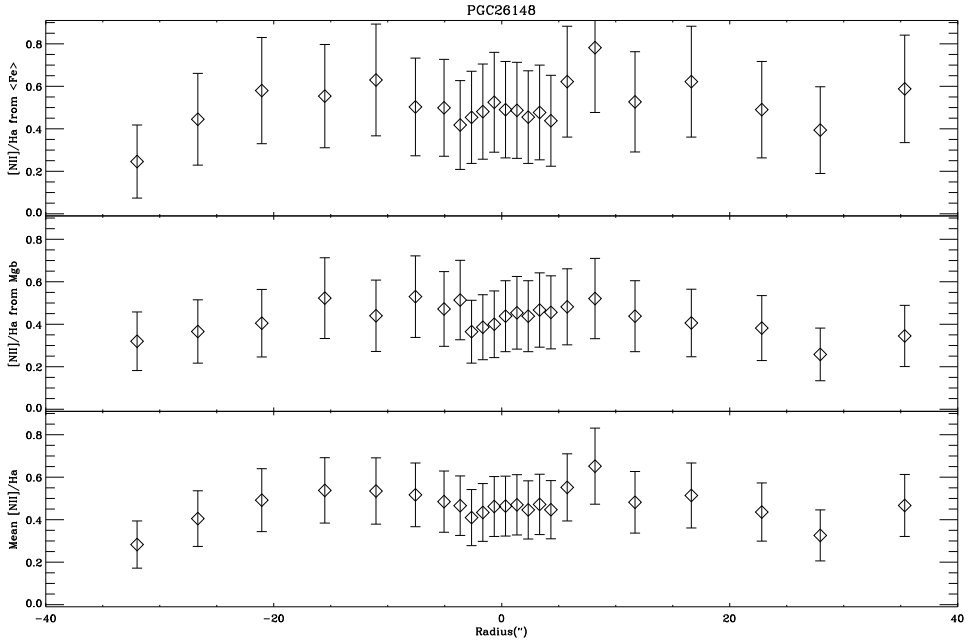

Figure 7.5: Continued

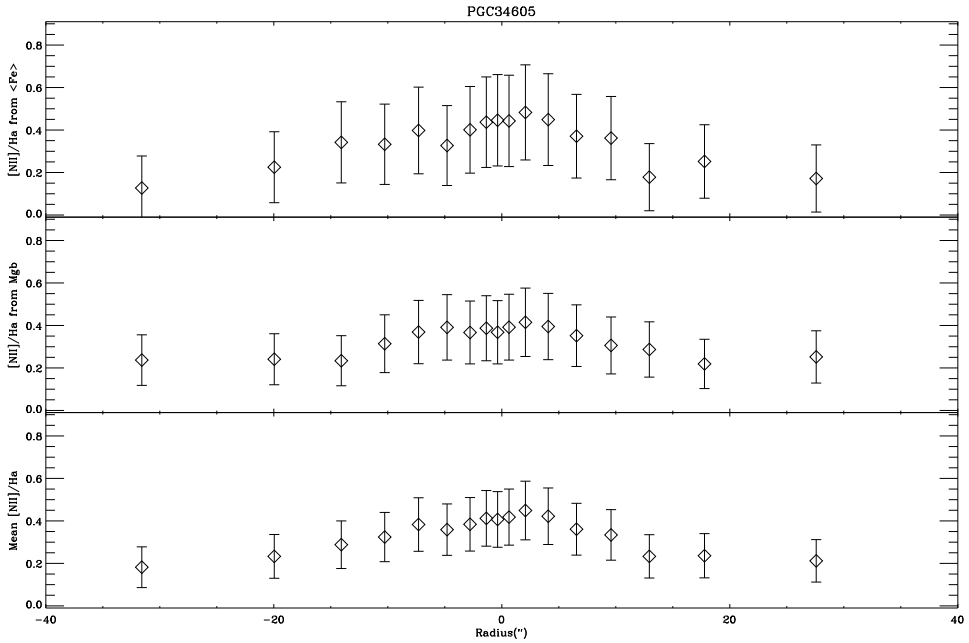

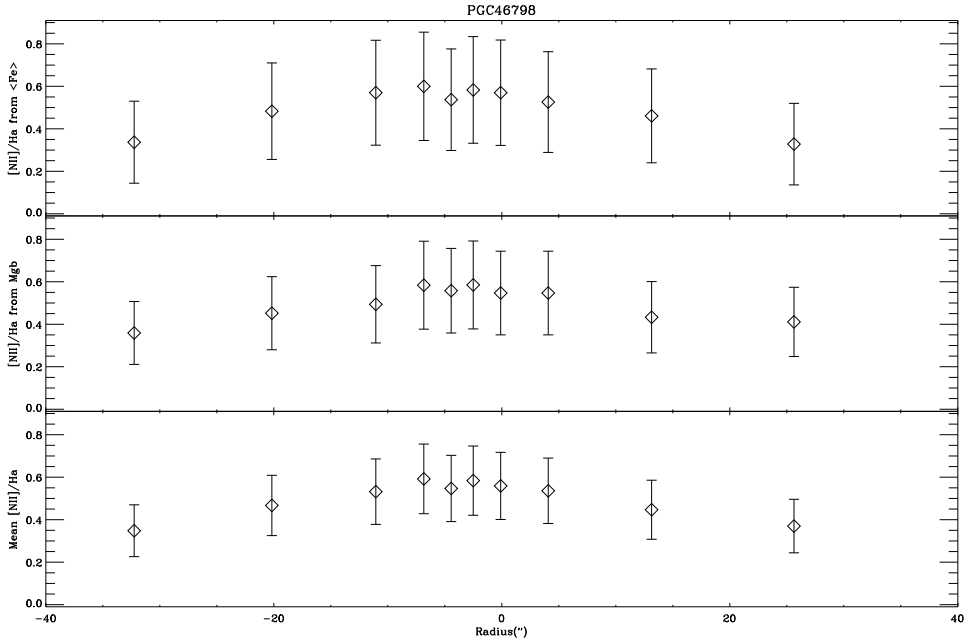

Figure 7.5: Continued

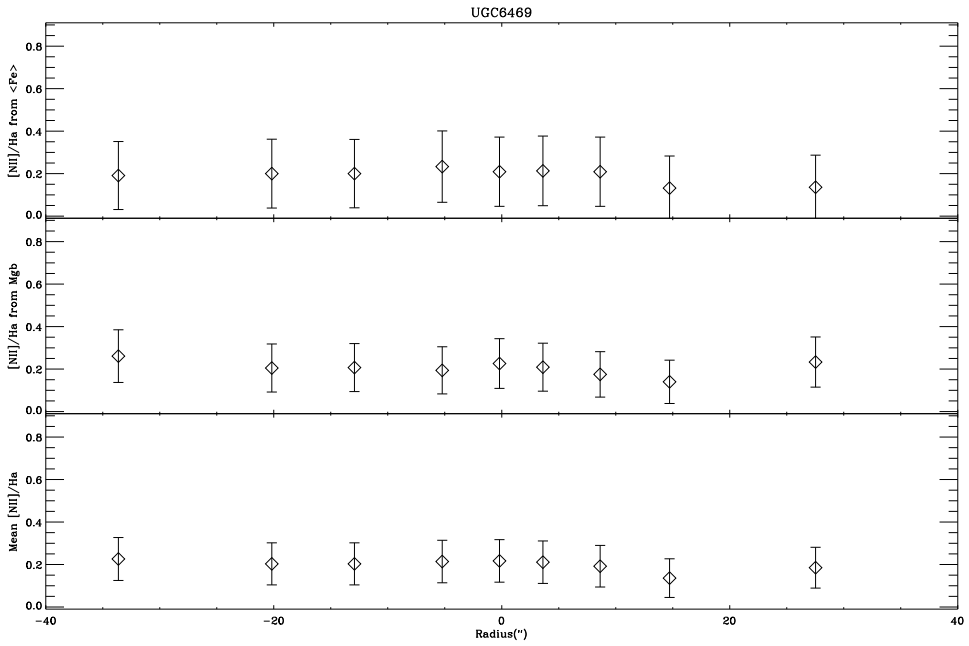

Figure 7.5: Continued

Chapter 8

Results and conclusion

In the previous sections we showed how we extracted from the orignal spectra of the LSB galaxies available, the information necessary to compute the metallicity indicator R_3 and [NII]/Hα. R_3 has been extracted directly from the emission lines available in the observed spectral range, while [NII]/Hα has been computed by means of the calibration found by Bergmann et al. (2003), starting from the stellar absorption indices Mgb and $\langle$Fe$\rangle$.

The values obtained for the [NII]/Hα ratio, which put our galaxies in the branch of high metallicity, in combination with the R_3 allow us to estimate the metallicity of the gas for our galaxies. The [OIII]/Hβ (Edmunds & Pagel, 1984) ratio has been calibrated by Vacca & Conti (1992) to give metallicities for the upper branch of the empirical oxygen abundance calibration, in the form $\log(O/H) = -0.69\ \log R_3 - 3.24$. More recently Liang et al. (2006), using a large sample of 38000 galaxies selected from the SDSS DR2, derived analytical calibrations for oxygen abundances from several metallicity-sensitive emission line ratios, among which R_3 and [NII]/[OIII]. We used here their third-order polynomial fit to obtain the metallicity values at each radius for our galaxies (see table

A.1 in appendix A):

$$12+\log(\mathrm{O/H}) = 8.841 - 0.575(\mathrm{R_3}) + 0.011(\mathrm{R_3})^2 + 0.297(\mathrm{R_3})^3 \quad (8.1)$$

$$12+\log(\mathrm{O/H}) = 9.013 - 0.395(\mathrm{O3N2}) - 0.072(\mathrm{O3N2})^2 + 0.106(\mathrm{O3N2})^3 \quad (8.2)$$

where $\mathrm{R_3}$=log([OIII]/Hβ) and O3N2=log(([OIII]/Hβ)/([NII]/Hα)).

The high quality data available for our galaxies, allows us to construct the radial profiles of metallicity. These are showed in figure 8.1.

Obtaining radial profile for low surface brightness galaxies is extremely difficult and thus rare, due to the fact that generally they lack enough bright HII regions to make abundance gradient determination. For this reason there are only few cases studied in literature that analyzed metallicity profiles for these galaxies.

de Blok & van der Hulst (1998) studying a sample of 12 LSB galaxies, obtained for three of them enough measurements over a large enough radial range to investigate possible oxygen abundance gradients. The result of their analysis however, showed no clear trend of abundance with radius.

We performed weighted linear least-squares to our data, represented in figure 8.1 as a straight line of the form $12+\log(\mathrm{O/H}) = a(\pm\sigma_a) + b(\pm\sigma_b)r$, being r the radius in kpc (values obtained for the parameters are summarized in table 8.1). We obtained slightly shallow (O/H) gradients, between -0.0192 ± 0.0066 and 0.0046 ± 0.0008 dex kpc^{-1}, which within 3σ are compatible with no gradient.

The lack of abundance gradients in LSB galaxies may indicate that the picture of galaxies evolving from inside out may not apply to LSB galaxies. It is commonly assumed that the gradients found in galaxies indicate that the exter-

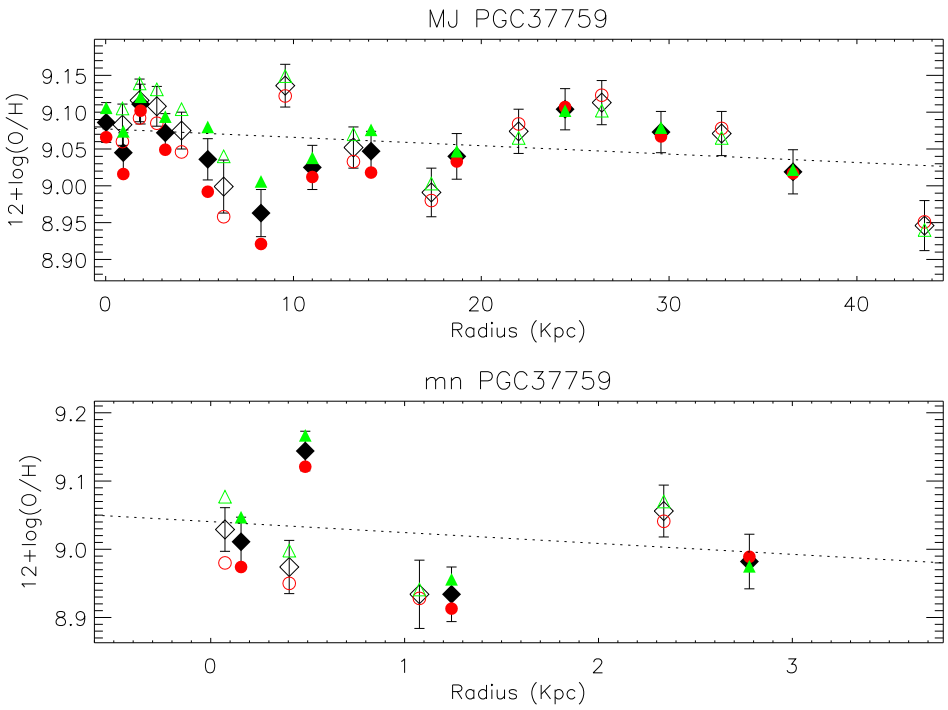

Figure 8.1: Radial distribution of the computed metallicity. The curves are folded around the nucleus and the filled and the open symbols refer to the two sides of the galaxy. Diamonds represent the average between the results obtained from equations 8.1 (in which metallicity is estimated only by means of the R_3 index, showed as circles) and 8.2 (in which the index O3N2 is used, showed as triangles). The error bars are the results of the propagation of the uncertainties. The straight dotted line represent the weighted linear least-squares fit to the data, which gives us the metallicity gradient.

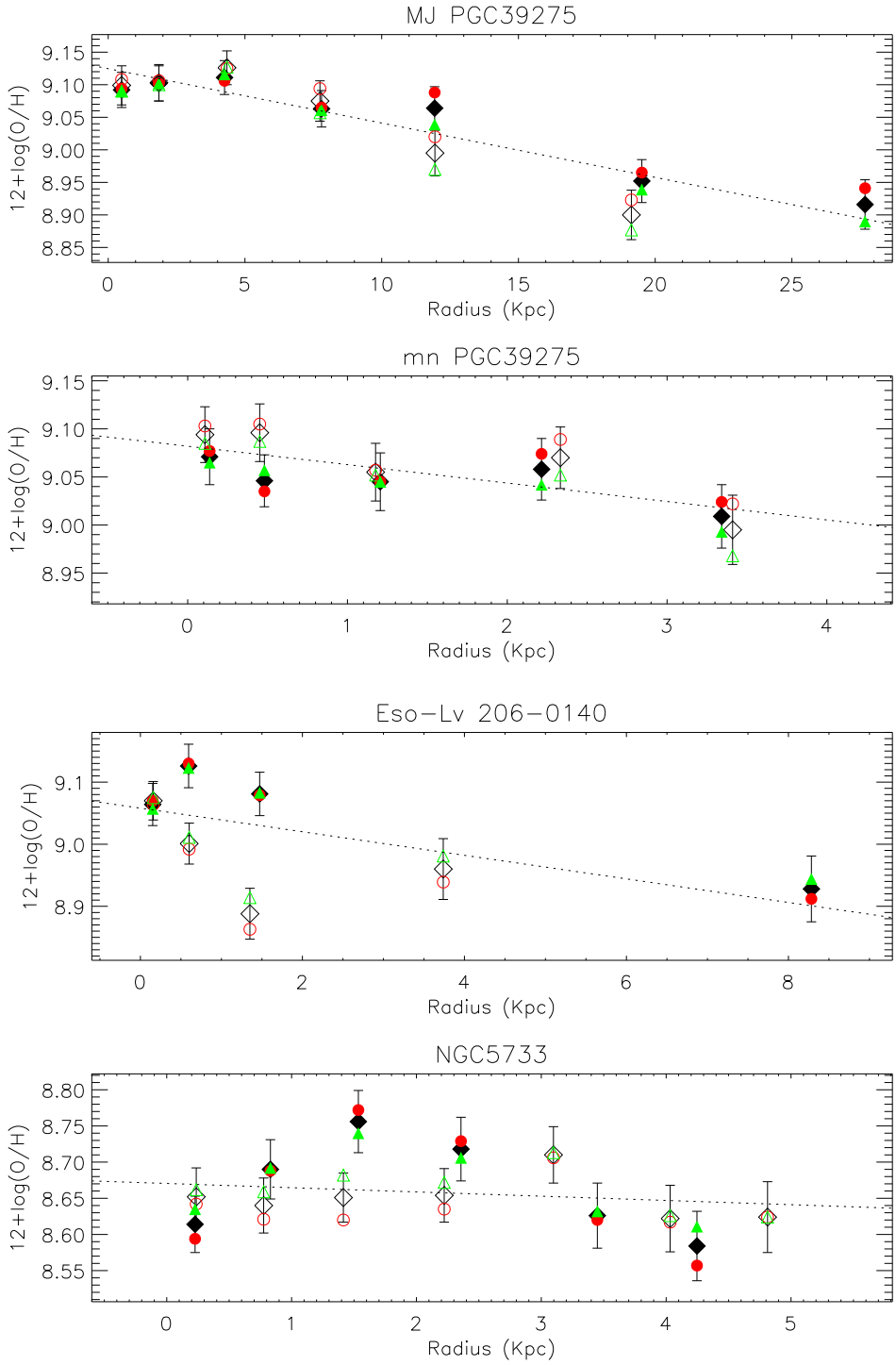

Figure 8.1: Continued

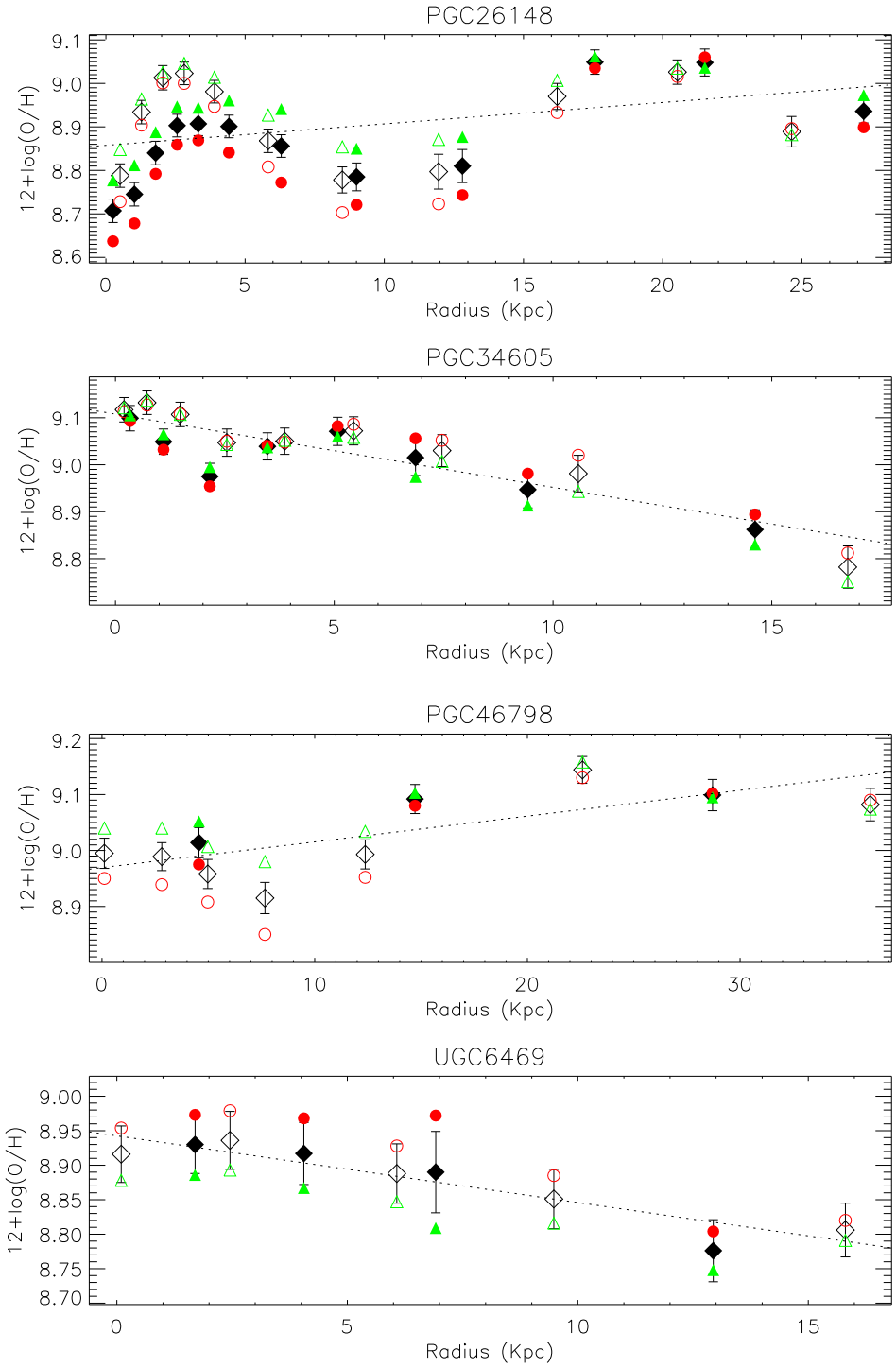

Figure 8.1: Continued

galaxy	a	σ_a	b	σ_b
MJ PGC37759	9.0773	0.0086	-0.0011	0.0005
mn PGC37759	9.0405	0.0185	-0.0160	0.0139
MJ PGC39275	9.1247	0.0119	-0.0083	0.0011
mn PGC39275	9.0820	0.0148	-0.0192	0.0084
Eso-Lv 206-0140	9.0581	0.0158	-0.0190	0.0066
NGC5733	8.6705	0.0199	-0.0059	0.0080
PGC26148	8.8576	0.0084	0.0049	0.0007
PGC34605	9.1077	0.0104	-0.0156	0.0018
PGC46798	8.9693	0.0130	0.0046	0.0008
UGC6469	8.9426	0.0234	-0.0097	0.0028

Table 8.1: Parameters obtained from the weighted linear least-squares fit to the data, represented by the straight dotted lines of the form 12+log(O/H) = $a(\pm\sigma_a) + b(\pm\sigma_b)r$, showed in figure 8.1.

nal regions are less evolved than the inner parts. The absence of such a radial trend would suggest that low surface brightness galaxies may have evolved at the same time rate over the whole disk.

Alternatively, the lack of a gradient may be explained if we consider an infall of metal-poor gas from high above the plane of these galaxies. However, because of the low star formation activity typical of LSBs, it is not likely that large amounts of gas can have been blown out in the past. If gas infall takes place, this must be primordial gas, dated back to when the LSB galaxies have been formed.

Another alternative is that the disks of LSB galaxies are still settling in their final configuration. In this case, gas from larger radii is slowly diffusing inward, causing enhancements where conditions for star formation may be favourable. This is qualitatively consistent with the finding that most of the star forming regions in LSB galaxies are generally found towards the outer radii of the stellar disk. If the star formation in LSB galaxies needs to be stimulated by external

conditions, like infall, and it is not self-propagating, this building up of the disk would not give rise to an abundance gradient. If every radius would go through one cycle of star formation before fading, after which star formation would move on to larger radii, this would not cause an abundance gradient.

The discussion presented in Edmunds & Roy (1993) about the presence of abundance gradients in gas-rich galaxies is of interest. They show that gradients seem to require the presence of unbarred spiral structure, and also that these gradients disappear at the same absolute magnitude that spiral structure ceases ($M_B \sim -17$). Late-type LSB galaxies show in general a faint spiral structure, and this can be related with the lack of abundance gradients.

There are two possible explanations. A declining star formation rate with radius can be related to a variation with radius of the frequency with which interstellar material crosses through a spiral pattern: if the spiral pattern would be absent, the star formation rate would consequently be more uniform across the disk. In alternative, if there are relatively important non-circular motions, this would lead a mixing that eventually would homogenize the chemical composition of the interstellar medium.

For the galaxies we analyzed, we obtained shallow abundance gradients which are compatible with no gradient, as found by de Blok & van der Hulst (1998). However we still observe a non negligible variation of the oxygen abundance between the center and the outer regions up till the limit of our observations, with mean value of 0.2 dex for almost all the galaxies here studied.
Also, in contrast with the general picture that claims the low-metallicity level for these kind of galaxies (McGaugh, 1994; Kuzio de Naray et al., 2004), we obtained high values for the oxygen abundances. The oxygen abundances we measured are comparable with the observed values for high surface brightness

galaxies (as showed for example by Garnett et al., 1997; van Zee et al., 1998).

Even if we cannot reproduce the steeper gradients found for some of these HSB galaxies, there is no need to suppose that the LSB galaxies here studied are fundamentally different from other types of galaxies.

Further investigation of these galaxies are still necessary to better understand their nature and how they differ (if they really do) from high surface brightness galaxies. For example, a comparison between the gas and the stellar metallicity at each radius would help to obtain a more precise information about the formation and evolution, while modelling would test the reliability of the evolution scenarios above described.

Appendix A

Measured values for LSB

Here there are reported the measurements obtained for the [NII]/Hα ratio for the low surface brightness galaxies analyzed, following Bergmann et al. (2003) (col. 2), at each radius (col. 1). In columns 3 and 4 there are reported the values obtained for the metallicity indices O3N2=log(([OIII]/Hβ)/([NII]/Hα)) and R_3=log([OIII]/Hβ), used to compute the metallcity values (col. 5) and the associated errors (col. 6) following equations 8.1 and 8.2, as derived by Liang et al. (2006).

Table A.1:

r	[NII]/Hα	O3N2	R3	12+log(O/H)	Δ(12+log(O/H))
(1)	(2)	(3)	(4)	(5)	(6)
Mj PGC37759					
-47.39	0.312	0.181	-0.195	8.946	0.034
-35.65	0.354	-0.135	-0.457	9.071	0.030
-28.71	0.330	-0.239	-0.590	9.113	0.030
-23.90	0.341	-0.136	-0.472	9.074	0.030
-18.85	0.393	0.026	-0.249	8.991	0.033
-14.34	0.462	-0.150	-0.355	9.052	0.028

-10.39	0.467	-0.388	-0.588	9.136	0.029
-6.83	0.539	-0.070	-0.208	8.999	0.036
-4.39	0.542	-0.247	-0.382	9.075	0.025
-2.96	0.527	-0.327	-0.475	9.108	0.027
-1.96	0.538	-0.355	-0.494	9.116	0.029
-0.97	0.508	-0.250	-0.413	9.083	0.028
0.03	0.493	-0.250	-0.427	9.086	0.027
1.02	0.515	-0.161	-0.319	9.045	0.027
2.02	0.442	-0.297	-0.521	9.111	0.027
3.45	0.497	-0.217	-0.390	9.072	0.026
5.91	0.597	-0.178	-0.271	9.036	0.028
8.99	0.514	0.019	-0.140	8.963	0.032
11.96	0.418	-0.063	-0.312	9.025	0.030
15.36	0.517	-0.167	-0.324	9.047	0.027
20.32	0.401	-0.087	-0.354	9.040	0.031
26.59	0.373	-0.238	-0.536	9.104	0.028
32.14	0.410	-0.174	-0.431	9.073	0.028
39.78	0.372	-0.022	-0.321	9.019	0.030
mn PGC37759					
-2.54	0.445	-0.150	-0.371	9.056	0.038
-1.17	0.347	0.177	-0.152	8.934	0.050
-0.44	0.437	0.037	-0.192	8.974	0.039
-0.08	0.618	-0.170	-0.248	9.029	0.032
0.17	0.526	-0.089	-0.237	9.011	0.036
0.53	0.545	-0.450	-0.583	9.144	0.029
1.35	0.400	0.142	-0.126	8.934	0.040
3.02	0.323	0.095	-0.266	8.982	0.040
Mj PGC39275					
-19.52	0.247	0.333	-0.144	8.900	0.038
-12.19	0.272	0.107	-0.328	8.995	0.035
-7.90	0.305	-0.113	-0.498	9.075	0.031
-4.43	0.387	-0.316	-0.598	9.126	0.026
-1.89	0.370	-0.233	-0.534	9.103	0.028
-0.50	0.342	-0.206	-0.541	9.099	0.030
0.50	0.374	-0.204	-0.500	9.092	0.027
1.89	0.387	-0.240	-0.522	9.102	0.027
4.34	0.412	-0.280	-0.535	9.111	0.026

7.96	0.370	-0.124	-0.426	9.063	0.028
12.18	0.283	-0.066	-0.484	9.064	0.033
19.91	0.294	0.182	-0.220	8.952	0.033
28.24	0.246	0.302	-0.177	8.916	0.038
mn PGC39275					
-3.48	0.267	0.111	-0.332	8.995	0.036
-2.38	0.304	-0.100	-0.487	9.070	0.032
-1.20	0.366	-0.102	-0.408	9.055	0.030
-0.46	0.343	-0.197	-0.532	9.096	0.030
-0.11	0.341	-0.190	-0.526	9.094	0.029
0.14	0.355	-0.137	-0.456	9.071	0.029
0.49	0.423	-0.115	-0.359	9.046	0.027
1.23	0.374	-0.083	-0.381	9.045	0.030
2.26	0.313	-0.074	-0.448	9.058	0.032
3.41	0.304	0.050	-0.336	9.009	0.033
mn ESO-LV 206-140					
-12.06	0.415	0.080	-0.172	8.960	0.049
-4.36	0.386	0.245	-0.038	8.888	0.041
-1.94	0.392	0.005	-0.271	9.001	0.033
-0.51	0.406	-0.163	-0.424	9.070	0.031
0.49	0.353	-0.115	-0.437	9.064	0.034
1.92	0.360	-0.303	-0.616	9.126	0.035
4.75	0.395	-0.186	-0.460	9.081	0.035
26.72	0.376	0.170	-0.125	8.928	0.053
Mj NGC5733.					
-40.10	0.136	1.153	0.418	8.624	0.049
-33.60	0.147	1.138	0.437	8.622	0.046
-25.81	0.219	0.773	0.244	8.710	0.039
-18.52	0.221	0.917	0.392	8.654	0.037
-11.79	0.263	0.878	0.429	8.651	0.034
-6.47	0.213	0.969	0.427	8.640	0.038
-1.97	0.196	0.955	0.377	8.652	0.040
1.89	0.191	1.087	0.498	8.614	0.039
6.92	0.201	0.845	0.278	8.690	0.041
12.79	0.198	0.694	0.122	8.756	0.043
19.64	0.187	0.797	0.199	8.718	0.044
28.74	0.157	1.102	0.428	8.626	0.045

35.39	0.118	1.426	0.630	8.584	0.048
Mj PGC26148					
-31.99	0.283	0.322	-0.096	8.889	0.035
-26.66	0.405	-0.057	-0.319	9.026	0.028
-21.05	0.492	0.016	-0.161	8.970	0.030
-15.52	0.538	0.349	0.210	8.797	0.040
-11.03	0.535	0.392	0.250	8.778	0.030
-7.57	0.517	0.213	0.057	8.868	0.027
-5.06	0.485	-0.004	-0.187	8.981	0.026
-3.65	0.466	-0.086	-0.287	9.023	0.026
-2.65	0.410	-0.031	-0.289	9.013	0.028
-1.66	0.434	0.122	-0.110	8.934	0.027
-0.66	0.462	0.407	0.202	8.788	0.027
0.33	0.464	0.590	0.387	8.707	0.027
1.33	0.470	0.496	0.299	8.745	0.027
2.32	0.446	0.306	0.086	8.840	0.027
3.32	0.472	0.164	-0.031	8.903	0.026
4.31	0.447	0.170	-0.049	8.907	0.027
5.74	0.552	0.128	0.001	8.901	0.026
8.18	0.652	0.178	0.122	8.856	0.026
11.69	0.482	0.402	0.215	8.785	0.032
16.63	0.514	0.333	0.174	8.810	0.038
22.81	0.436	-0.129	-0.359	9.049	0.028
27.94	0.326	-0.059	-0.415	9.048	0.031
35.35	0.467	0.099	-0.102	8.936	0.027
Mj PGC34605					
-31.58	0.182	0.660	0.051	8.782	0.045
-19.96	0.233	0.174	-0.328	8.981	0.039
-14.08	0.288	0.015	-0.396	9.030	0.034
-10.27	0.324	-0.117	-0.477	9.072	0.030
-7.30	0.383	-0.100	-0.386	9.050	0.028
-4.80	0.359	-0.077	-0.392	9.047	0.029
-2.79	0.384	-0.254	-0.540	9.107	0.026
-1.36	0.412	-0.348	-0.603	9.132	0.025
-0.37	0.407	-0.295	-0.555	9.117	0.026
0.63	0.418	-0.248	-0.497	9.099	0.027
2.07	0.449	-0.136	-0.353	9.049	0.027

4.07	0.422	0.044	-0.200	8.975	0.028
6.55	0.361	-0.061	-0.372	9.039	0.029
9.58	0.334	-0.121	-0.467	9.071	0.030
12.94	0.233	0.098	-0.405	9.015	0.038
17.78	0.236	0.247	-0.251	8.947	0.039
27.58	0.212	0.451	-0.092	8.862	0.042
Mj PGC46798					
-32.25	0.348	-0.161	-0.490	9.082	0.029
-20.17	0.467	-0.418	-0.618	9.144	0.024
-11.05	0.532	-0.053	-0.197	8.993	0.026
-6.84	0.592	0.082	-0.015	8.915	0.028
-4.44	0.547	0.014	-0.117	8.958	0.026
-2.51	0.584	-0.069	-0.172	8.989	0.025
-0.10	0.559	-0.070	-0.193	8.995	0.027
4.07	0.536	-0.100	-0.240	9.014	0.027
13.14	0.447	-0.243	-0.463	9.092	0.026
25.63	0.370	-0.220	-0.522	9.099	0.028
Mj UGC6469.					
-33.63	0.226	0.551	0.036	8.806	0.039
-20.17	0.203	0.486	-0.077	8.851	0.043
-12.92	0.203	0.408	-0.153	8.888	0.043
-5.22	0.214	0.294	-0.246	8.936	0.042
-0.20	0.217	0.332	-0.201	8.916	0.041
3.61	0.211	0.311	-0.235	8.930	0.042
8.63	0.192	0.360	-0.226	8.917	0.045
14.72	0.136	0.504	-0.233	8.890	0.059
27.53	0.185	0.668	0.065	8.776	0.045

Appendix B

The ultraviolet flare at the center of the elliptical galaxy NGC 4278

Published on A&A 2009, Vol. 508, p. 641

A. Cardullo[1], E. M. Corsini[1], A. Beifiori[1], L. M. Buson[2], E. Dalla Bontà[1], L. Morelli[1], A. Pizzella[1], and F. Bertola[1]

[1]Dipartimento di Astronomia, Università di Padova, vicolo dell'Osservatorio 2, I-35122 Padova, Italy

[2]INAF, Osservatorio Astronomico di Padova, vicolo dell'Osservatorio 5, I-35122 Padova, Italy

Abstract

Context. A large fraction of otherwise normal galaxies shows a weak nuclear activity. One of the signatures of the low-luminosity active galactic nuclei (LLAGNs) is ultraviolet variability which was serendipitously discovered in the

center of some low-ionization nuclear emission-line region (LINER) galaxies.

Aims. There is a pressing need to acquire better statistics about UV flaring and variability in galaxy nuclei, both in terms of the number and monitoring of targets. The Science Data Archive of the Hubble Space Telescope was queried to find all the elliptical galaxies with UV images obtained in different epochs with the Wide Field Planetary Camera 2 (WFPC2) and possibly with nuclear spectra obtained with the Space Telescope Imaging Spectrograph (STIS) in the region of the Hα emission line. These data were found only for the elliptical radiogalaxy NGC 4278.

Methods. The UV flux of the nuclear source of NGC 4278 was measured by means of aperture photometry on the WFPC2/F218W images obtained between June 1994 and January 1995. The mass of the central supermassive black hole (SBH) was estimated by measuring the broad components of the emission lines observed in the STIS/G750M spectrum and assuming that the gas is uniformly distributed in a sphere.

Results. The nucleus of NGC 4278 hosts a barely resolved but strongly variable UV source. Its UV luminosity increased by a factor of 1.6 in a period of 6 months. The amplitude and scale time of the UV flare in NGC 4278 are remarkably similar to those of the brightest UV nuclear transients which were found earlier in other LLAGNs. The mass of the SBH was found to be in the range between 7×10^7 and 2×10^9 $M_\odot$. This is in agreement with previous findings based on different assumptions about the gas distribution and with the predictions based on the galaxy velocity dispersion.

Conclusions. All the LINER nuclei with available multi-epoch UV observations and a detected radio core are characterized by a UV variable source. This supports the idea that the UV variability is a relatively common phenomenon in

galaxy centers, perhaps providing the missing link between LINERs and true AGN activity.

B.1 Introduction

A large fraction of otherwise normal galaxies shows weak nuclear activity. These low-luminosity active galactic nuclei (LLAGNs) occupy the faintest end of the luminosity function of the AGNs and have very low accretion rates or radiative efficiencies onto the central supermassive black hole (SBH, see Ho, 2008 for a review).

One of the signatures of LLAGNs is ultraviolet (UV) variability as observed with Hubble Space Telescope (HST) in the nuclei of some low-ionization nuclear emission-line region (LINER) galaxies. There have been a number of reports after the serendipitous discovery of a UV flare in the center of the elliptical galaxy NGC 4552 (Renzini et al., 1995; Cappellari et al., 1999). The images of its nucleus obtained in a five year period with the Faint Object Camera (FOC) showed an increase of the UV luminosity by a factor of 4.5 followed by a dimming of a factor of 2. O'Connell et al. (2005) unveiled a similar phenomenon in the giant elliptical NGC 1399 using the Space Telescope Imaging Spectrograph (STIS), while a rapidly fading UV source was detected in the Virgo cluster spiral NGC 4579 (Maoz et al., 1995; Barth et al., 1996). This kind of research took on a more systematic approach by Maoz et al. (2005), who monitored the UV variability of a sample of 17 LINER galaxies with compact nuclear UV sources by means of the HST Advanced Camera for Surveys (ACS). They detected a significant UV variability in almost all the sample galaxies, which were mostly spirals, with amplitudes ranging from a few to 50 percent.

This suggests that the UV variability is a relatively common phenomenon in

galaxy centers. Given this, there is a need to acquire better statistics, both in terms of the number of targets and monitoring the UV-variable nuclei. Maoz et al. (1995) already queried the HST Science Data Archive for ACS data and observed mostly spiral galaxies. We searched the Wide Field Planetary Camera 2 (WFPC2) archive for all the RC3 (de Vaucouleurs et al., 1991) elliptical galaxies having UV images obtained with the same filter in different epochs before 2008. We found 37 objects (12 LINERs, 2 Seyferts, 1 transition and 1 H II nucleus, 17 quiescent galaxies, and 4 objects with unknown nuclear activity; Ho et al., 1997, and NASA/IPAC Extragalactic Database) with at least one F218W or F300W image. NGC 4278 was the only galaxy with multi-epoch WFPC2/F218W images, which was not studied before. A nuclear spectrum obtained within a subarcsecond aperture by STIS in the Hα region was also available in the HST Science Data Archive. In this paper, we present and discuss the results about the UV variability of its nucleus including an estimate of the mass of its SBH based on STIS spectroscopy.

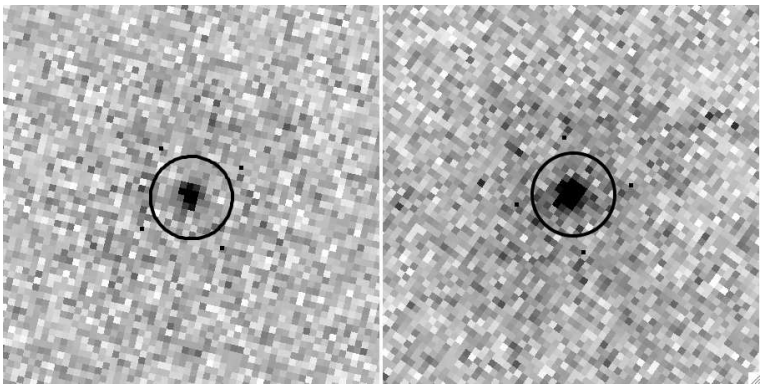

Figure B.1: WFPC2/F218W images of the NGC 4278 nucleus of 2 June 1994 (left) and 14 January 1995 (right), plotted with the same grayscale. Each panel is $2\farcs5$ on a side, north is up and east at the left. The UV flux was measured within the aperture marked by the circle ($r = 0\farcs28$).

B.2 NGC 4278

NGC 4278 is a large ($4\farcm1 \times 3\farcm8$, RC3) and bright ($B_T = 11.09$, RC3) elliptical galaxy. It is classified E1–2 and hosts a LINER nucleus (L1.9, Ho et al., 1997). Its total absolute magnitude is $M^0_{B_T} = -20.03$ (RC3), adopting a distance of 16.1 Mpc (Tonry et al., 2001). NGC 4278 is member of the Coma I cloud (Forbes, 1996). It was one of the first elliptical galaxies in which neutral hydrogen was detected (Gallagher et al., 1977) and used to infer the dark mater content at large radii (Bertola et al., 1993). It is distributed in an inclined outer ring (Raimond et al., 1981), which is possibly associated with the inner disk of ionized gas (Goudfrooij et al., 1994; Sarzi et al., 2006). The northwest side of the galaxy is heavily obscured by large-scale dust patches and filaments which seem to spiral down into the nucleus (Carollo et al., 1997).

The optical and radio properties of the nucleus have been investigated in detail (see Giroletti et al., 2005, and references therein). The radio data reveal two symmetric steep-spectrum jets on a sub parsec scale. They emerge from a flat-spectrum core and are responsible for the bulk of the emission at radio to optical frequencies in a similar way to that seen in more powerful radio loud AGNs. However, the total radio luminosity of NGC 4278 is at least 2 orders of magnitude less than those objects (Condon et al, 1998). This makes NGC 4278 an LLAGN (Giroletti et al., 2005).

B.3 Observations, data reduction, and analysis

B.3.1 Nuclear ultraviolet variability

The multi-epoch images obtained with the WFPC2 and the F218W filter were retrieved from the HST Science Data Archive. A 1800 s exposure was taken on

2 June 1994 (Prog. Id. 5380, P.I. A. Koratkar). Two exposures of 2200 s and 2300 s were obtained on 14 January 1995 (Prog. Id. 5381, P.I. A. Koratkar). The exposures were taken with the telescope guiding in fine lock mode, which typically gave an rms tracking error of $0\farcs003$. We focused our attention on the Planetary Camera (PC) chip where the nucleus of the galaxy was centered. This consists of 800×800 pixels of $0\farcs0455 \times 0\farcs0455$ each, yielding a field of view of about $36'' \times 36''$.

The images were calibrated using the standard WFPC2 reduction pipeline maintained by the Space Telescope Science Institute (STScI). Reduction steps including bias subtraction, dark current subtraction, and flat-fielding are described in detail in the WFPC2 instrument and data handbooks (Holtzman et al., 1995b; Baggett et al., 2002; Mc Master et al., 2008). Subsequent reduction was completed using standard tasks in the STSDAS package of IRAF[1]. The bad pixels were corrected by means of a linear one-dimensional interpolation using the data quality files and the WFIXUP task. The two 1995 images were aligned and combined using IMSHIFT and knowledge of the offset shifts. Cosmic ray events and residual hot pixels were removed using the LACOS_IMA procedure (van Dokkum, 2001). The cosmic ray removal and bad pixel correction were checked by inspection of the residual image between the cleaned and the original frame to ensure that the nuclear region was not affected by light loss. The residual cosmic rays and bad pixels in the PC were corrected by manually editing the resulting image with IMEDIT. The sky level (~ 1 count pixel^{-1}) was determined from apparently empty regions in the Wide Field chips and subtracted from the PC frame after appropriate scaling.

The flux calibration was performed by adopting the Vega magnitude system

[1]Imaging Reduction and Analysis Facilities is distributed by National Optical Astronomy Observatories (NOAO).

(Whitmore, 1995) and by taking into account the time dependence of the UV response (Mc Master & Whitmore, 2002). The presence of contaminants within WFPC2 causes a gradual build-up of material on the cold CCD faceplate of the camera, resulting in a decrease in the UV throughput. The contaminants are evaporated by periodically heating the camera to restore the instrumental throughput to its nominal value. The contamination rate is remarkably constant during each decontamination cycle, and can be accurately modeled by a simple linear decline following the decontaminations. The observed fluxes were corrected by assuming a decline in the F218W/PC normalized count rate of $(4.78 \pm 0.28) \times 10^{-3}$ per day since decontamination. This was derived during the decontamination cycles performed between April 1994 and June 1995 (Mc Master & Whitmore, 2002), which bracket the observations of NGC 4278.

Evidence of the presence of a nuclear source was found in the two final images of NGC 4278. It is barely resolved (FWHM = 0.″07) when compared to the WFPC2/F218W point spread function (PSF, FWHM = 0.″06) derived with the TINY TIM package (Krist & Hook, 1999). The total flux of the nuclear source was estimated as the flux in the circular aperture of radius of 0.″28 (Fig. B.1). The background level was determined as the median of the flux within the annulus of 0.″37–0.″51 centered on the source. The correction for the finite aperture radius has been performed by multiplying counts by 1.18±0.01, based on the encircled-energy value of a point source tabulated in Holtzman et al. (1995a). The errors were calculated taking in account the Poisson and CCD readout noises, charge transfer efficiency, correction for contamination, and correction for finite aperture. The UV flux of the central source of NGC 4278 in the WFPC2/F218W passband increased from $(6.94\pm0.46)\times10^{-16}$ to $(10.83\pm0.25)\times 10^{-16}$ erg cm^{-2} s^{-1} Å^{-1} from 2 June 1994 to 14 January 1995 (Fig. B.2).

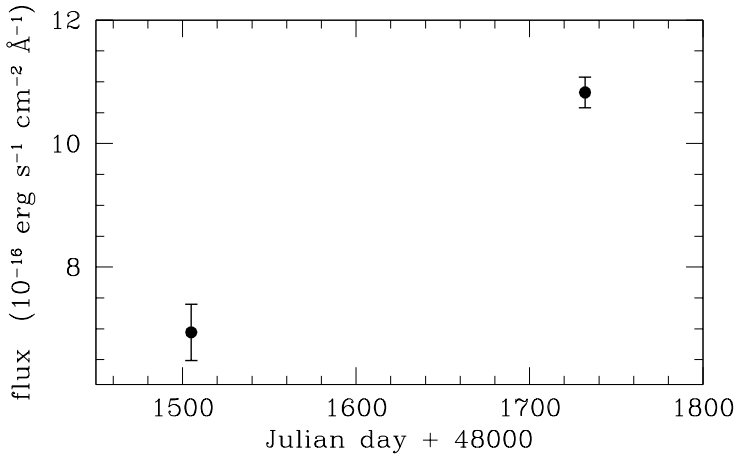

Figure B.2: UV light curve in WFPC2/F218W band for the nucleus of NGC 4278. Points correspond to fluxes measured on 2 June 1994 and 14 January 1995, respectively.

B.3.2 Estimate of the mass of the central black hole

The long-slit spectrum of the nucleus of NGC 4278 obtained with STIS in the region of the [N II] $\lambda\lambda 6548, 6583$, H$\alpha$, and [S II] $\lambda\lambda 6716, 6731$ emission lines (Prog. Id. 7403, P.I. A. Filippenko) was retrieved from the HST Science Data Archive. The G750M grating was used at the secondary tilt $\lambda_c = 6581$ Å covering the wavelength range 6295–6867 Å. The spectrum was taken with the $0\farcs2 \times 52''$ slit placed across the galaxy nucleus with a position angle of $87\fdg9$. The total exposure time was 3128 s. The dispersion is 0.55 Å pixel^{-1}. The instrumental resolution is 1.6 Å (FWHM) corresponding to $\sigma_{\rm inst} \approx 32$ km s^{-1} at Hα. The spatial scale of the 1024×1024 SITe CCD is $0\farcs05$ pixel^{-1}.

The spectrum was reduced using IRAF and the STIS reduction pipeline maintained by the STScI. The basic reduction steps including overscan subtraction, bias subtraction, dark subtraction, and flatfield correction are described in detail in the STIS instrument and data handbooks (Kim Quijano et al., 2007; Dressel

et al., 2007). The cosmic ray events and hot pixels were removed using the task LACOS_SPEC by van Dokkum (2001). The residual bad pixels were corrected by means of a linear one-dimensional interpolation using the data quality files. The wavelength and flux calibration as well as geometric correction for two-dimensional distortion were performed following the standard STIS reduction pipeline and applying the X2D task. This task corrected the wavelength scale to the heliocentric frame as well.

The central wavelengths, FWHMs, and intensities of the all the observed emission lines were measured following Beifiori et al. (2009). The broad and narrow components of the emission lines were fitted with multiple Gaussians, while describing the stellar continuum with a low-order polynomial. A flux ratio of 1:2.96 was assumed for the [N II] doublet, as dictated by atomic physics (e.g., Osterbrock, 1989) and both the [N II] and [S II] doublets were assumed to share a common line centroid and width. A broad component was needed to describe the Hα emission out to $0\farcs20$ from the center. The forbidden [N II] and [S II] lines required a broad component from $-0\farcs05$ to $+0\farcs1$. Fig. B.3 shows the continuum-subtracted nuclear spectrum of NGC 4278 with the fitted emission lines. It was extracted from the three central rows of the Hα STIS/G750M spectrum centered on the continuum peak. It thus consists of the central emission convolved with the STIS spatial PSF and sampled over a nearly square aperture of $0\farcs15 \times 0\farcs2$ (corresponding to 12×16 pc^2).

The mass $M_\bullet$ of the central SBH can be estimated from the virial theorem by assuming that the gas is uniformly distributed within a sphere of radius R and moves around the SBH with a mean velocity measured from the width of the broad component of the Hα line.

The lower limit on the size of the broad-line emitting region is given by the

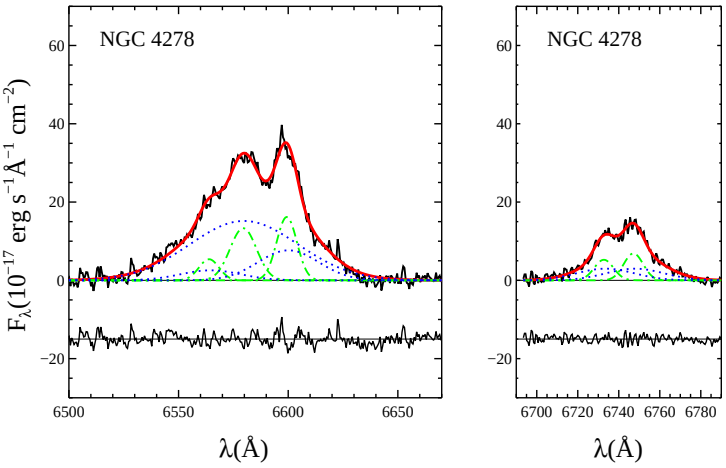

Figure B.3: Continuum-subtracted central spectrum of NGC 4278 in the Hα+[N II] (left panel) and [S II] (right panel) regions. In each panel, the red solid line shows the overall line blend, whereas the green dashed-dotted lines and blue dotted lines show the adopted narrow and broad Gaussian components, respectively. The fit residuals also are shown, offset for better visibility.

upper limit to the gas density as set by the forbidden lines and Hα luminosity. Following Osterbrock (1989)

$$R_{\rm min} = \left(\frac{3 L_{\rm H\alpha}}{4\pi f n_{\rm e}^2 \alpha_{\rm H\alpha}^{\rm eff} h \nu_{\rm H\alpha}} \right)^{\frac{1}{3}} \tag{B.1}$$

where $L_{\rm H\alpha}$ is the total luminosity of the Hα broad component, f is the volume filling factor, $n_{\rm e}$ is the electron density of the gas, $\alpha_{\rm H\alpha}^{\rm eff}$ is the recombination coefficient for Hα, h is the Planck constant, and $\nu_{\rm H\alpha}$ is the frequency of the Hα line. The ratio of the [S II] lines sets $n_{\rm e} \approx 10^5$ cm^{-3}, whereas the spherical and uniform distribution of the gas gives a filling factor equal to 1. It is $L_{\rm H\alpha} = 4.13 \times 10^{38}$ erg s^{-1} from the measured flux $(1.34 \pm 0.10) \times 10^{-14}$ erg s^{-1} cm^{-2} and assumed distance. We then find $R_{\rm min} = 0.1$ pc. In this region $\sigma_V = 1224 \pm 40$ km s^{-1}, which corresponds to a lower limit on the SBH mass of $M_\bullet \geq R_{\rm min}\sigma_V^2/G \simeq 7 \times 10^7$ M$_\odot$.

The upper limit on the size of the broad-line emitting region $R_{\rm max}$ can be estimated from the intrinsic emissivity distribution of the gaseous sphere. An intrinsically Gaussian flux profile centered on the stellar nucleus was assumed. It has a FWHM = 0.″19 (15 pc) when accounting for the STIS PSF (FWHM = 0.″09). The choice of a Gaussian parametrization is also conservative, since cuspier functions would have led us to estimate smaller $M_\bullet$. We find $R_{\rm max}$ = 5.9 pc and $\sigma_V = 1127 \pm 30$ km s^{-1} which translates into an upper limit on the SBH mass of $M_\bullet \leq R_{\rm max}\sigma_V^2/G \simeq 2 \times 10^9$ M$_\odot$.

B.4 Conclusions

UV variability with amplitudes ranging from a few to 50 percent over a timescale of a decade was detected in most of the LINER nuclei observed more than once (Maoz et al., 2005) suggesting a possible link between UV flares and SBH-related activity in LLAGNs. To acquire better statistics, both in terms of the number of targets and their monitoring, we queried the HST Science Archive for all the elliptical galaxies with available UV images obtained with the WFPC2 in different epochs.

Multi-epoch images were found only for NGC 4278, a nearby radiogalaxy known to host a LLAGN (Giroletti et al., 2005). It is characterized by a barely resolved nuclear source, which increased its UV luminosity by a factor of 1.6 in a period of 6 months. The amplitude and scale time of the variation are similar to those of the UV-brightest nuclear transients, which were earlier discovered in NGC 4552 (Renzini et al., 1995; Cappellari et al., 1999), NGC 4579 (Maoz et al., 1995; Barth et al., 1996), and NGC 1399 (O'Connell et al., 2005).

These serendipituous findings support the idea that the UV variability is a common event at the center of galaxies where SBHs reside. Some alternatives to

the AGN interpretation were explored to explain the UV variability. Maoz et al. (2005) pointed out that individual supergiants in galactic nuclei are not plausible candidates to produce the observed UV flux variations. On the other hand, the even brighter Wolf-Rayet and luminous blue variable stars could only explain the variations measured in the nuclei of lower UV luminosity. The fallback of debris onto the SBH, and collisions between precessing debris orbits (Rees, 1988; Kim et al., 1999) are expected to produce bright UV/X-rays flares (Ulmer, 1999). But given their rarity ($\approx 10^{-4}$ yr^{-1} per galaxy, Magorrian & Tremaine , 1999; Wang & Merritt, 2004), the stellar tidal disruptions can emerge only in all-sky deep X-ray (Donley et al., 2002; Esquej et al., 2007) and UV surveys (Gezari et al., 2006, 2008, 2009) and cannot account all the observed variable nuclei. This is particularly true for the galaxies with repeated episodes of UV variability, like NGC 4552 (Renzini et al., 1995; Cappellari et al., 1999; Maoz et al., 2005).

It was possible to estimate the mass of the SBH at the center of NGC 4278. The central width and radial extension of the broad components of the emission lines were measured over a subarcsecond aperture in the available STIS spectrum of the nucleus. If the gas is uniformly distributed within a sphere then it is $7 \times 10^7 \leq M_\bullet \leq 2 \times 10^9$ M$_\odot$. This is consistent with the predictions of the $M_\bullet - \sigma_c$ relations by Ferrarese & Ford (2005) and Lauer et al. (2007) when adopting a central velocity dispersion $\sigma_c = 333 \pm 8$ km s^{-1} (Beifiori et al., 2009). There is also a good agreement with the upper limits on $M_\bullet$ given by Beifiori et al. (2009). They measured the nuclear width of the narrow component of the [N II] λ6583 emission line and modelled it as due to the Keplerian motion of a thin disk of ionized gas around the putative SBH. They found $M_\bullet \leq 5 \times 10^7$ for a nearly edge-on disk and $M_\bullet \leq 2 \times 10^8$ M$_\odot$ for a nearly face-on disk.

According to Giroletti et al. (2005) this SBH is active and able to produce

the relativistic jet, responsible for most of the emission at optical and radio frequencies of this LLAGN. It is the same process as the ordinary radio loud AGNs despite a much lower power. The AGN interpretation is a promising way to explain the UV variability. In fact, all the LINER nuclei with multi-epoch observations and a detected radio core are characterized by UV variable sources (Maoz et al., 2005). This is the case of NGC 4278, too, suggesting that UV variability could provide the missing link between LINERS and true AGN activity. Unfortunately, it is the only elliptical galaxy observed by HST at different epochs in the UV and which was not studied before. This fact does not allow us to derive any firm statistical conclusion about the frequency of UV flares at the center of elliptical galaxies. Nevertheless, out of 37 galaxies, the only object with multi-epoch UV observations turned out to be variable. This is a further suggestion that this phenomenon may be quite common. Additional imaging with the Wide Field Camera 3 recently installed on HST to monitor the UV variablity in a statistically significant sample of quiescent and active nuclei and STIS spectra to measure their SBHs are highly desirable to gain insights into this subject in the near future.

Acknowledgements. AC acknowledges the Space Telescope Science Institute for hospility while this work was in progress. We thank Massimo Stiavelli and Michele Cappellari for useful discussions and their helpful comments. This work was made possible through grants CPDA068415 and CPDA089220 by Padua University. This research has made use of the Lyon-Meudon Extragalactic Database (LEDA) and NASA/IPAC Extragalactic Database (NED).

Bibliography

Abazajian, K., et al. 2005, AJ, 129, 1755

Adelman-McCarthy, J. K., et al. 2006, ApJS, 162, 38

Adelman-McCarthy, J. K., et al. 2008, ApJS, 175, 297

Aguerri, J. A. L., Balcells, M., & Peletier, R. F. 2001, A&A, 367, 428

Alloin, D., Collin-Souffrin, S., Joly, M., & Vigroux, L. 1979, A&A, 78, 200

Arimoto, N., & Yoshii, Y. 1987, A&A, 173, 23

Asari, N. V., Cid Fernandes, R., Stasińska, G., Torres-Papaqui, J. P., Mateus, A., Sodré, L., Schoenell, W., & Gomes, J. M. 2007, MNRAS, 381, 263

Baggett, S., et al. 2002, WFPC2 Data Handbook, Version 4.0 (STScI, Baltimore)

Barth, A. J., Reichert, G. A., Filippenko, A. V., Ho, L. C., Shields, J. C., Mushotzky, R. F., & Puchnarewicz, E. M. 1996, AJ, 112, 1829

Baugh, C. M., Cole, S., & Frenk, C. S. 1996, MNRAS, 283, 1361

Beifiori, A., Sarzi, M., Corsini, E. M., Dalla Bontà, E., Pizzella, A., Coccato, L., & Bertola, F. 2009, ApJ, 692, 856

Beifiori, A., Maraston, C., Thomas, D., & Johansson, J. 2010, arXiv:1012.3428

Bell, E. F., Barnaby, D., Bower, R. G., de Jong, R. S., Harper, D. A., Hereld, M., Loewenstein, R. F., & Rauscher, B. J. 2000, MNRAS, 312, 470

Bender, R., & Renzini, A. 2003, The Mass of Galaxies at Low and High Redshift, ESO Astrophysics Symposia, Springer-Verlag Berlin Heidelberg New York

Beijersbergen, M., de Blok, W. J. G., & van der Hulst, J. M. 1999, A&A, 351, 903

Bergmann, M. P., Jørgensen, I., & Hill, G. J. 2003, AJ, 125, 116

Bertola, F., Pizzella, A., Persic, M., & Salucci, P. 1993, ApJ, 416, L45

Bothun, G., Impey, C., & McGaugh, S. 1997, PASP, 109, 745

Burkholder, V., Impey, C., & Sprayberry, D. 2001, AJ, 122, 2318

Cappellari, M., Renzini, A., Greggio, L., di Serego Alighieri, S., Buson, L. M., Burstein, D., & Bertola, F. 1999, ApJ, 519, 117

Cappellari, M., & Emsellem, E. 2004, PASP, 116, 138

Cardullo, A., Corsini, E. M., Beifiori, A., Buson, L. M., Dalla Bontà, E., Morelli, L., Pizzella, A., & Bertola, F. 2009, A&A, 508, 641

Carollo, C. M., Franx, M., Illingworth, G. D., & Forbes, D. A. 1997, ApJ, 481, 710

Cole, S., Lacey, C. G., Baugh, C. M., & Frenk, C. S. 2000, MNRAS, 319, 168

Condon, J. J., Cotton, W. D., Greisen, E. W., Yin, Q. F., Perley, R. A., Taylor, G. B., & Broderick, J. J. 1998, AJ, 115, 1693

Contini, T., Treyer, M. A., Sullivan, M., & Ellis, R. S. 2002, MNRAS, 330, 75

Dalcanton, J. J., Spergel, D. N., Gunn, J. E., Schmidt, M., & Schneider, D. P. 1997, AJ, 114, 635

de Blok, W. J. G., van der Hulst, J. M., & Bothun, G. D. 1995, MNRAS, 274, 235

de Blok, W. J. G., McGaugh, S. S., & van der Hulst, J. M. 1996, MNRAS, 283, 18

de Blok, W. J. G. 1997, Ph.D. Thesis,

de Blok, W. J. G., & McGaugh, S. S. 1997, MNRAS, 290, 533

de Blok, W. J. G., & van der Hulst, J. M. 1998, A&A, 335, 421

de Jong, R. S., & Lacey, C. 2000, ApJ, 545, 781

De Lucia, G., Kauffmann, G., & White, S. D. M. 2004, MNRAS, 349, 1101

de Mello, D. F., Daddi, E., Renzini, A., Cimatti, A., di Serego Alighieri, S., Pozzetti, L., & Zamorani, G. 2004, ApJ, 608, L29

de Vaucouleurs, G., de Vaucouleurs, A., Corwin, H. G., Jr., Buta, R. J., Paturel, G., & Fouque, P. 1991, The Third Refecence Catalog of Bright Galaxies (RC3). Springer-Verlag Berlin Heidelberg New York

Donley, J. L., Brandt, W. N., Eracleous, M., & Boller, T. 2002, AJ, 124, 1308

Dopita, M. A., Kewley, L. J., Heisler, C. A., & Sutherland, R. S. 2000, ApJ, 542, 224

Dressel, L., et al. 2007, STIS Data Handbook, Version 5.0 (STScI, Baltimore)

Driver, S. P., Allen, P. D., Liske, J., & Graham, A. W. 2007, ApJ, 657, L85

Edmunds, M. G., & Pagel, B. E. J. 1984, MNRAS, 211, 507

Edmunds, M. G., & Roy, J.-R. 1993, MNRAS, 261, L17

Eggen, O. J., Lynden-Bell, D., & Sandage, A. R. 1962, ApJ, 136, 748

Ellison, S. L., Patton, D. R., Simard, L., & McConnachie, A. W. 2008, AJ, 135, 1877

Erb, D. K., Shapley, A. E., Pettini, M., Steidel, C. C., Reddy, N. A., & Adelberger, K. L. 2006, ApJ, 644, 813

Esquej, P., Saxton, R. D., Freyberg, M. J., Read, A. M., Altieri, B., Sanchez-Portal, M., & Hasinger, G. 2007, A&A, 462, L49

Ferrarese, L., & Ford, H. 2005, Space Science Reviews, 116, 523

Feulner, G., Gabasch, A., Salvato, M., Drory, N., Hopp, U., & Bender, R. 2005, ApJ, 633, L9

Finlator, K., & Davé, R. 2008, MNRAS, 385, 2181

Forbes, D. A. 1996, AJ, 112, 1409

Franceschini, A., et al. 2006, A&A, 453, 397

Freeman, K. C. 1970, ApJ, 160, 811

Gallagher, J. S., Knapp, G. R., Faber, S. M., & Balick, B. 1977, ApJ, 215, 463

Ganda, K., et al. 2007, MNRAS, 380, 506

Garnett, D. R., Shields, G. A., Skillman, E. D., Sagan, S. P., & Dufour, R. J. 1997, ApJ, 489, 63

Gezari, S., et al. 2006, ApJ, 653, L25

Gezari, S., et al. 2008, ApJ, 676, 944

Gezari, S., et al. 2009, ApJ, 698, 1367

Gilmore, G., & Wyse, R. F. G. 1998, AJ, 116, 748

Giroletti, M., Taylor, G. B., & Giovannini, G. 2005, ApJ, 622, 178

Goudfrooij, P., Hansen, L., Jorgensen, H. E., & Norgaard-Nielsen, H. U. 1994, A&AS, 105, 341

Guseva, N. G., Izotov, Y. I., & Thuan, T. X. 2000, ApJ, 531, 776

Guseva, N. G., Papaderos, P., Izotov, Y. I., Green, R. F., Fricke, K. J., Thuan, T. X., & Noeske, K. G. 2003, A&A, 407, 75

Guseva, N. G., Papaderos, P., Izotov, Y. I., Green, R. F., Fricke, K. J., Thuan, T. X., & Noeske, K. G. 2003, A&A, 407, 91

Guseva, N. G., Papaderos, P., Izotov, Y. I., Green, R. F., Fricke, K. J., Thuan, T. X., & Noeske, K. G. 2003, A&A, 407, 105

Hamuy, M., Walker, A. R., Suntzeff, N. B., Gigoux, P., Heathcote, S. R., & Phillips, M. M. 1992, PASP, 104, 533

Ho, L. C., Filippenko, A. V., & Sargent, W. L. W. 1997, ApJS, 112, 315

Ho, L. C., 2008, ARA&A, 46, 475

Holtzman, J. A., et al. 1995a, PASP, 107, 156

Holtzman, J. A., Burrows, C. J., Casertano, S., Hester, J. J., Trauger, J. T., Watson, A. M., & Worthey, G. 1995b, PASP, 107, 1065

Horne, K. 1986, PASP, 98, 609

Hoyos, C., Koo, D. C., Phillips, A. C., Willmer, C. N. A., & Guhathakurta, P. 2005, ApJ, 635, L21

Impey, C. D., Sprayberry, D., Irwin, M. J., & Bothun, G. D. 1996, ApJS, 105, 209

Impey, C., Burkholder, V., & Sprayberry, D. 2001, AJ, 122, 2341

Izotov, Y. I., Thuan, T. X., & Lipovetsky, V. A. 1994, ApJ, 435, 647

Izotov, Y. I., Thuan, T. X., & Lipovetsky, V. A. 1997, ApJS, 108, 1

Izotov, Y. I., Lipovetsky, V. A., Chaffee, F. H., Foltz, C. B., Guseva, N. G., & Kniazev, A. Y. 1997, ApJ, 476, 698

Izotov, Y. I., & Thuan, T. X. 1998, ApJ, 500, 188

Izotov, Y. I., & Thuan, T. X. 2004, ApJ, 602, 200

Izotov, Y. I., Papaderos, P., Guseva, N. G., Fricke, K. J., & Thuan, T. X. 2004, A&A, 421, 539

Izotov, Y. I., Stasińska, G., Meynet, G., Guseva, N. G., & Thuan, T. X. 2006, A&A, 448, 955

Jansen, R. A., Fabricant, D., Franx, M., & Caldwell, N. 2000, ApJS, 126, 331

Juneau, S., et al. 2005, ApJ, 619, L135

Kakazu, Y., Cowie, L. L., & Hu, E. M. 2007, ApJ, 668, 853

Kauffmann, G. 1996, MNRAS, 281, 487

Kewley, L. J., & Dopita, M. A. 2002, ApJS, 142, 35

Krist, J., & Hook, R. 1999, The Tiny Tim User's Guide (STScI, Baltimore)

Kim, S. S., Park, M.-G., & Lee, H. M. 1999, ApJ, 519, 647

Kim Quijano, J., et al. 2007, STIS Instrument Handbook, Version 8.0 (STScI, Baltimore)

Kobulnicky, H. A., & Skillman, E. D. 1996, ApJ, 471, 211

Kobulnicky, H. A., & Zaritsky, D. 1999, ApJ, 511, 118

Kobulnicky, H. A., & Phillips, A. C. 2003, ApJ, 599, 1031

Köppen, J., Weidner, C., & Kroupa, P. 2007, MNRAS, 375, 673

Kormendy, J., & Kennicutt, R. C., Jr. 2004, ARA&A, 42, 603

Kuzio de Naray, R., McGaugh, S. S., & de Blok, W. J. G. 2004, MNRAS, 355, 887

Lamareille, F., Mouhcine, M., Contini, T., Lewis, I., & Maddox, S. 2004, MNRAS, 350, 396

Lamareille, F., Contini, T., Brinchmann, J., Le Borgne, J.-F., Charlot, S., & Richard, J. 2006, A&A, 448, 907

Larson, R. B. 1975, MNRAS, 173, 671

Lauer, T. R., et al. 2007, ApJ, 662, 808

Lee, H., McCall, M. L., Kingsburgh, R. L., Ross, R., & Stevenson, C. C. 2003, AJ, 125, 146

Lee, H., Grebel, E. K., & Hodge, P. W. 2003, A&A, 401, 141

Lee, H., Skillman, E. D., Cannon, J. M., Jackson, D. C., Gehrz, R. D., Polomski, E. F., & Woodward, C. E. 2006, ApJ, 647, 970

Lee, J. C., Salzer, J. J., & Melbourne, J. 2004, ApJ, 616, 752

Lequeux, J., Peimbert, M., Rayo, J. F., Serrano, A., & Torres-Peimbert, S. 1979, A&A, 80, 155

Liang, Y. C., Yin, S. Y., Hammer, F., Deng, L. C., Flores, H., & Zhang, B. 2006, ApJ, 652, 257

Lilly, S. J., Carollo, C. M., & Stockton, A. N. 2003, ApJ, 597, 730

Magorrian, J., & Tremaine, S. 1999, MNRAS, 309, 447

Magrini, L., Sestito, P., Randich, S., & Galli, D. 2009, A&A, 494, 95

Maier, C., Meisenheimer, K., & Hippelein, H. 2004, A&A, 418, 475

Maier, C., Lilly, S. J., Carollo, C. M., Stockton, A., & Brodwin, M. 2005, ApJ, 634, 849

Maiolino, R., et al. 2008, A&A, 488, 463

Matteucci, F., & Tornambe, A. 1987, A&A, 185, 51

Maoz, D., Filippenko, A. V., Ho, L. C., Rix, H.-W., Bahcall, J. N., Schneider, D. P., & Macchetto, F. D. 1995, ApJ, 440, 91

Maoz, D., Nagar, N. M., Falcke, H., & Wilson, A. S. 2005, ApJ, 625, 699

McGaugh, S. S. 1991, ApJ, 380, 140

McGaugh, S. S., & Bothun, G. D. 1994, AJ, 107, 530

McGaugh, S. S. 1994, ApJ, 426, 135

Mc Master, M., & Whitmore, B. 2002, WFPC2 Instruments Science Report, 02-07 (STScI, Baltimore)

Mc Master, Biretta, et al. 2008, WFPC2 Instrument Handbook, Version 10.0 (STScI, Baltimore)

Mehlert, D., Thomas, D., Saglia, R. P., Bender, R., & Wegner, G. 2003, A&A, 407, 423

Mehlert, D., Tapken, C.,Appenzeller, I., Noll, S., de Mello, D.,& Heckman, T. M. 2006, A&A, 455, 835

Melbourne, J., & Salzer, J. J. 2002, AJ, 123, 2302

Melbourne, J., Phillips, A., Salzer, J. J., Gronwall, C., & Sarajedini, V. L. 2004, AJ, 127, 686

Morelli, L., et al. 2008, MNRAS, 389, 341

Nagao, T., Maiolino, R., & Marconi, A. 2006, A&A, 459, 85

Nilson, P. 1973, Nova Acta Regiae Soc. Sci. Upsaliensis Ser. V, 0

Noeske, K. G., Papaderos, P., Cairós, L. M., & Fricke, K. J. 2003, A&A, 410, 481

O'Connell, R. W., Martin, J. R., Crane, J. D., Burstein, D., Bohlin, R. C., Landsman, W. B., Freedman, I., & Rood, R. T. 2005, ApJ, 635, 305

O'Neil, K., Bothun, G. D., & Cornell, M. E. 1997, AJ, 113, 1212

O'Neil, K., Bothun, G. D., Schombert, J., Cornell, M. E., & Impey, C. D. 1997, AJ, 114, 2448

Osterbrock, D. E. 1989, Astrophysics of Gaseous Nebulae and Active Galactic Nuclei (Univ. Science Books, Mill Valley)

Osterbrock, D. E., Fulbright, J. P., Martel, A. R., Keane, M. J., Trager, S. C., & Basri, G. 1996, PASP, 108, 277

Pagel, B. E. J., Edmunds, M. G., Blackwell, D. E., Chun, M. S., & Smith, G. 1979, MNRAS, 189, 95

Pagel, B. E. J., Simonson, E. A., Terlevich, R. J., & Edmunds, M. G. 1992, MNRAS, 255, 325

Papaderos, P., Izotov, Y. I., Fricke, K. J., Thuan, T. X., & Guseva, N. G. 1998, A&A, 338, 43

Papaderos, P., Izotov, Y. I., Thuan, T. X., Noeske, K. G., Fricke, K. J., Guseva, N. G., & Green, R. F. 2002, A&A, 393, 461

Papaderos, P., Izotov, Y. I., Guseva, N. G., Thuan, T. X., & Fricke, K. J. 2006, A&A, 454, 119

Peletier, R. F., et al. 2007, MNRAS, 379, 445

Pettini, M., & Pagel, B. E. J. 2004, MNRAS, 348, L59

Pilyugin, L. S. 2001, A&A, 369, 594

Pilyugin, L. S. 2003, A&A, 399, 1003

Pilyugin, L. S., Vílchez, J. M., & Contini, T. 2004, A&A, 425, 849

Pilyugin, L. S., & Thuan, T. X. 2005, ApJ, 631, 231

Pipino, A., & Matteucci, F. 2004, MNRAS, 347, 968

Pipino, A., & Matteucci, F. 2006, MNRAS, 365, 1114

Pipino, A., D'Ercole, A., & Matteucci, F. 2008, A&A, 484, 679

Pipino, A., & Matteucci, F. 2008, A&A, 486, 763

Pizzella, A., Corsini, E. M., Dalla Bontà, E., Sarzi, M., Coccato, L., & Bertola, F. 2005, ApJ, 631, 785

Pizzella, A., Corsini, E. M., Sarzi, M., Magorrian, J., Méndez-Abreu, J., Coccato, L., Morelli, L., & Bertola, F. 2008, MNRAS, 387, 1099

Raimond, E., Faber, S. M., Gallagher, J. S., III, & Knapp, G. R. 1981, ApJ, 246, 708

Rees, M. J. 1988, Nature, 333, 523

Renzini, A., Greggio, L., di Serego-Alighieri, S., Cappellari, M., Burstein, D., & Bertola, F. 1995, Nature, 378, 39

Richer, M. G., & McCall, M. L. 1995, ApJ, 445, 642

Rix, S. A., Pettini, M., Leitherer, C., Bresolin, F., Kudritzki, R.-P., & Steidel, C. C. 2004, ApJ, 615, 98

Salzer, J. J., Lee, J. C., Melbourne, J., Hinz, J. L., Alonso-Herrero, A., & Jangren, A. 2005, ApJ, 624, 661

Sánchez-Blázquez, P., et al. 2006, MNRAS, 371, 703

Sarzi, M., et al. 2006, MNRAS, 366, 1151

Savaglio, S., et al. 2005, ApJ, 635, 260

Saviane, I., Ivanov, V. D., Held, E. V., Alloin, D., Rich, R. M., Bresolin, F., & Rizzi, L. 2008, A&A, 487, 901

Schombert, J. M., & Bothun, G. D. 1988, AJ, 95, 1389

Schombert, J. M., Bothun, G. D., Schneider, S. E., & McGaugh, S. S. 1992, AJ, 103, 1107

Shi, F., Kong, X., Li, C., & Cheng, F. Z. 2005, A&A, 437, 849

Skillman, E. D., Kennicutt, R. C., & Hodge, P. W. 1989, ApJ, 347, 875

Smartt, S. J., & Rolleston, W. R. J. 1997, ApJ, 481, L47

Smith, B. J., & Hancock, M. 2009, AJ, 138, 130

Smith, J. A., et al. 2002, AJ, 123, 2121

Sprayberry, D., Impey, C. D., Bothun, G. D., & Irwin, M. J. 1995, AJ, 109, 558

Stasińska, G. 2006, A&A, 454, L127

Storchi-Bergmann, T., Calzetti, D., & Kinney, A. L. 1994, ApJ, 429, 572

Thuan, T. X., Izotov, Y. I., & Lipovetsky, V. A. 1995, ApJ, 445, 108

Tonry, J. L., Dressler, A., Blakeslee, J. P., Ajhar, E. A., Fletcher, A. B., Luppino, G. A., Metzger, M. R., & Moore, C. B. 2001, ApJ, 546, 681

Tremonti, C. A., et al. 2004, ApJ, 613, 898

Ulmer, A. 1999, ApJ, 514, 180

Vacca, W. D., & Conti, P. S. 1992, ApJ, 401, 543

Vaduvescu, O., McCall, M. L., & Richer, M. G. 2007, AJ, 134, 604

van Dokkum, P. G. 2001, PASP, 113, 1420

van Zee, L., Salzer, J. J., Haynes, M. P., O'Donoghue, A. A., & Balonek, T. J. 1998, AJ, 116, 2805

Vanzi, L., Hunt, L. K., Thuan, T. X., & Izotov, Y. I. 2000, A&A, 363, 493

Vila-Costas, M. B., & Edmunds, M. G. 1992, MNRAS, 259, 121

Vilchez, J. M., & Esteban, C. 1996, MNRAS, 280, 720

Vílchez, J. M., & Iglesias-Páramo, J. 2003, ApJS, 145, 225

Vorobyov, E. I., Shchekinov, Y., Bizyaev, D., Bomans, D., & Dettmar, R.-J. 2009, A&A, 505, 483

Wang, J., & Merritt, D. 2004, ApJ, 600, 149

Whitmore, B. 1995, in Koratkar, A., Leitherer, C., eds, Calibrating Hubble Space Telescope: Post Servicing Mission (STScI, Baltimore), 269

Worthey, G., Faber, S. M., Gonzalez, J. J., & Burstein, D. 1994, ApJS, 94, 687

Yegorova, I. A., Pizzella, A., & Salucci, P. 2011, arXiv:1106.5105

Yin, S. Y., Liang, Y. C., Hammer, F., Brinchmann, J., Zhang, B., Deng, L. C., & Flores, H. 2007, A&A, 462, 535

Zaritsky, D., Kennicutt, R. C., Jr., & Huchra, J. P. 1994, ApJ, 420, 87